MASTER THESIS

Tracked ultrasound for patient registration in surgical navigation during abdominal cancer surgery

By

M.A.J. HIEP

A thesis submitted in fulfillment of the requirements for the degree of Master of Science

in

Technical Medicine
Track: Medical Imaging and Interventions
Faculty of Science and Technology

UNIVERSITY OF TWENTE.

NETHERLANDS CANCER INSTITUTE
ANTONI VAN LEEUWENHOEK

March 4, 2021

Graduation Committee

Chairman and technological supervisor:	Dr. ir. F. van der Heijden Department of Robotics and Mechatronics University of Twente Enschede, The Netherlands
Clinical supervisor:	Prof. dr. T.J.M. Ruers Professor Oncology and Biomedical Imaging University of Twente Enschede, The Netherlands Department of Surgery Netherlands Cancer Institute Amsterdam, The Netherlands
Process supervisor:	MSc. R.J. Haarman Faculty of Science and Technology University of Twente Enschede, The Netherlands
Additional supervisor:	Dr. W.J. Heerink Department of Surgery Netherlands Cancer Institute Amsterdam, The Netherlands
Additional supervisor:	Dr. ir. H.C. Groen Department of Surgery Netherlands Cancer Institute Amsterdam, The Netherlands
External member:	Dr. A.T.M. Bellos-Grob Faculty of Science and Technology University of Twente Enschede, The Netherlands

UNIVERSITY OF TWENTE

Abstract

Master of Science

Tracked ultrasound for patient registration in surgical navigation during abdominal cancer surgery

by M.A.J. HIEP

Surgical navigation is needed for the localization of tumors, malignant lymph nodes and other surrounding structures during abdominal cancer surgery. Currently, a cone-beam computed tomography (CBCT) scan is made on the operating room (OR) for the patient registration with pre-operative imaging and the electromagnetic (EM) tracking system. However, patient movement or tilting the surgical bed after scanning often results in surgical navigation inaccuracies. Additionally, the CBCT is limitedly available, clinical workflow is fully interrupted during scanning and staff and patient are exposed to radiation. Tracked ultrasound (US) might overcome these limitations, since US acquisition is possible on every OR regardless of the patient position, causes minimal workflow interruption and is non-invasive. Therefore, in this thesis, the feasibility and accuracy of EM tracked US was evaluated in a patient study.

Firstly, a hybrid magneto-optical tracking setup was developed to examine possible interference of two US devices: BK and Clarius. Static and dynamic measurements were performed, which provided insight to fixate an EM sensor to the US device at a location with minimal interference. Secondly, both US devices were separately calibrated with the EM tracking system using the tracked pointer method, resulting in a calibration accuracy of 1.5 and 3.1 mm for BK and Clarius, respectively. Lastly, an US registration method based on the pelvic bone was applied on patients undergoing navigated abdominal cancer surgery. The accuracy of this method was evaluated at surgical targets compared to the current reference: CBCT registration. The influence of alternate patient positions on the registration was evaluated by acquiring US scans in Trendelenburg and in horizontal patient position.

Ten patients were included in total. After exclusion of three unreliable patient measurements, an average target registration error of 2.6 mm was found for the BK US device, which suggest an acceptable navigation accuracy of $<$5 mm. Comparison of the horizontal with Trendelenburg US registration showed an average target registration discrepancy of 7.0 mm with an average offset in caudal-cranial direction of 6.5 mm. Further research is required to evaluate the true intra-operative navigation accuracy and the development of an automatic US bone segmentation algorithm is recommended.

It is concluded that the tracked US registration method is feasible and accurate at surgically relevant targets in the pelvic cavity regardless of the patient position or surgical bed tilting on the OR. This method has the potential to replace the current CBCT-scan in abdominal cancer navigation surgery.

Acknowledgements

First of all, I would like to thank my supervisors for the support during my graduation internship. I am very grateful for everything I have learned this year on clinical, scientific and personal level to develop myself as a healthcare professional. In addition, I want to thank all colleagues from the Antoni van Leeuwenhoek hospital for the helpful collaboration and enjoyable (online) coffee breaks. Lastly, a special thanks to my family and friends for all support and motivation, which aided me to perform to the best of my abilities.

Marijn Hiep
March 2021

Contents

List of Figures

List of Tables

List of Abbreviations

2D	Two-dimensional
3D	Three-dimensional
5DOF	Five degrees of freedom
6DOF	Six degrees of freedom
APR	Abdominoperineal resection
BMI	Body mass index
CBCT	Cone-beam computed tomography
CT	Computed tomography
EM	Electromagnetic
EMTS	Electromagnetic tracking system
FG	Field generator
HU	Hounsfield unit
ICP	Iterative closest point
IGS	Image guided surgery
IMU	Inertial measurement unit
LAR	Low anterior resection
LND	Lymph node dissection
LOOCV	Leave-one-out cross-validation
LOOCVE	Leave-one-out cross-validation error
MAE	Mean absolute error
MRI	Magnetic resonance imaging
NKI-AvL	Netherlands Cancer Institute-Antoni van Leeuwenhoek
OR	Operating room
OTS	Optical tracking system
PET	Positron emission tomography
RMSE	Root-mean-square error
SCU	System control unit
SD	Standard deviation
SIU	Sensor interface unit
SOS	Speed of sound
TME	Total mesorectal excision
TRD	Target registration discrepancy
TRE	Target registration error
TTFG	Tabletop field generator
US	Ultrasound

Chapter 1

Introduction

1.1 Clinical background

1.1.1 Anatomy of the lower abdominal and pelvic area

Several organs are located in the lower abdominal and pelvic area, such as the small bowel, colon, urinary bladder and reproductive organs. The anatomy of the colon has been visualized in Figure 1.1. The ascending colon starts from the caecum in the right lower quadrant of the abdomen. The colon continues as the transverse colon, descending colon and sigmoid, ending at the rectum and anal canal. The anatomic location of the colon is prone to movement, because it is not fixated inside the abdomen. However, the distal part of the sigmoid and the rectum are more fixated inside the pelvic cavity of the abdomen [1].

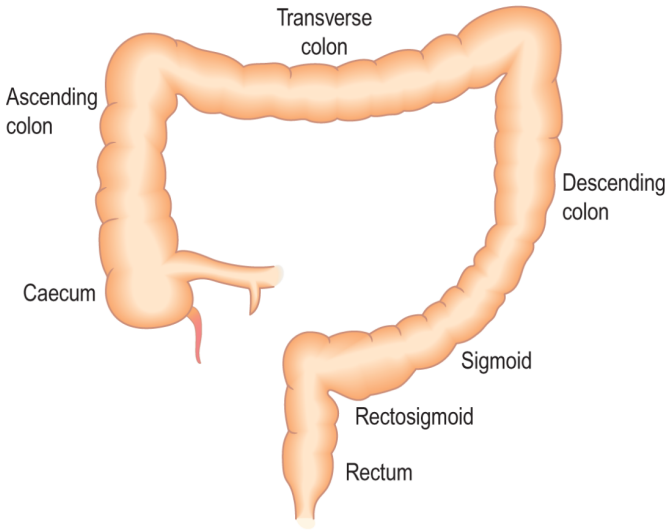

FIGURE 1.1: Anterior view of the anatomy of the colon [1].

The lower part of the abdomen is located inside the pelvic cavity, which is surrounded by the pelvic bone. The pelvis consists of two hip bones, visualized in Figure 1.2. Each hip bone is composed of three parts: the ilium, ischium and pubis. The pelvis is connected to other bones by the attachment of the ilium to the sacrum posteriorly and connection to the femurs at the acetabulum. Anteriorly, the hip bones are attached to each other by the pubic symphysis [2].

The main organs located inside the pelvic cavity are the urinary bladder, reproductive organs, sigmoid and rectum. These organs are relatively fixed, but could slightly move relative to the pelvic bone. Furthermore, the pelvic cavity contains

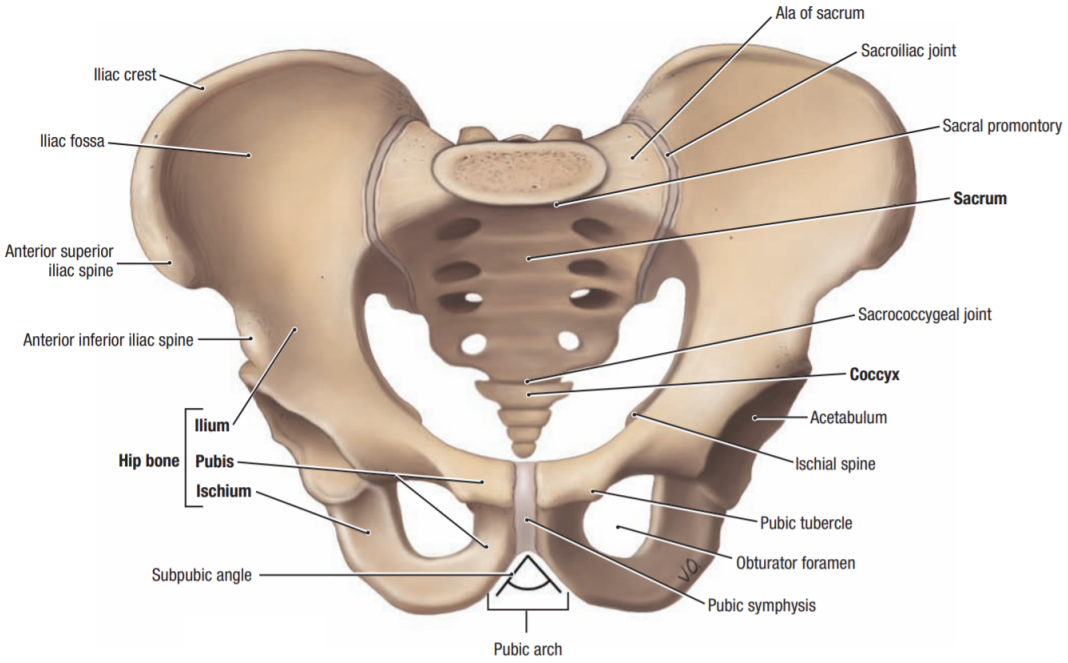

FIGURE 1.2: Anterior view of the pelvic bones [2].

a complex network of major arteries, veins, nerves, ureters and the lymphatic system. The abdominal aorta enters the pelvic cavity by bifurcating into the left and right common iliac artery, which branch further into the internal and external iliac artery. The internal iliac artery splits into an anterior and posterior branch to supply blood to several organs and tissues within the pelvic region. The external iliac artery supplies blood to the lower extremities by continuing caudally as the femoral artery. These pelvic arteries are visualized in Figure 1.3 [2], [3].

The major veins in the pelvic cavity lie posterior and inferior to the iliac arteries, roughly following their paths. Their names are similar to the major pelvic arteries, namely the external and internal iliac veins, which join into the common iliac vein into the inferior vena cava. The common iliac artery is crossed by the ureter at or directly distal to the bifurcation [3].

The lymphatic system in the lower abdominal cavity is visualized in Figure 1.4. In this figure, the lymph node stations are highlighted relative to the pelvic arteries. These groups are highly interconnected, meaning that many lymph nodes could be removed without disturbing the draining system. However, the number, size and location of these lymph nodes are anatomically variable, which means that Figure 1.4 only provides an indication of the main lymph node stations [3].

1.1.2 Abdominal cancer

Abdominal cancer covers a broad range of cancer types within the abdominal area, such as colorectal cancer, prostate cancer or bladder cancer. Overall, the most common type of abdominal cancer is colorectal cancer. Worldwide, 1.8 million patients were diagnosed with colorectal cancer in 2018 [4]. In the Netherlands, the incidence is approximately 14,000 patients in the same year [5]. Furthermore, colorectal cancer is the second most deadly cancer worldwide, with 881,000 estimated deaths for 2018 [6]. The colorectal cancer mortality in the Netherlands was approximately 5,000 deaths in 2017 [5].

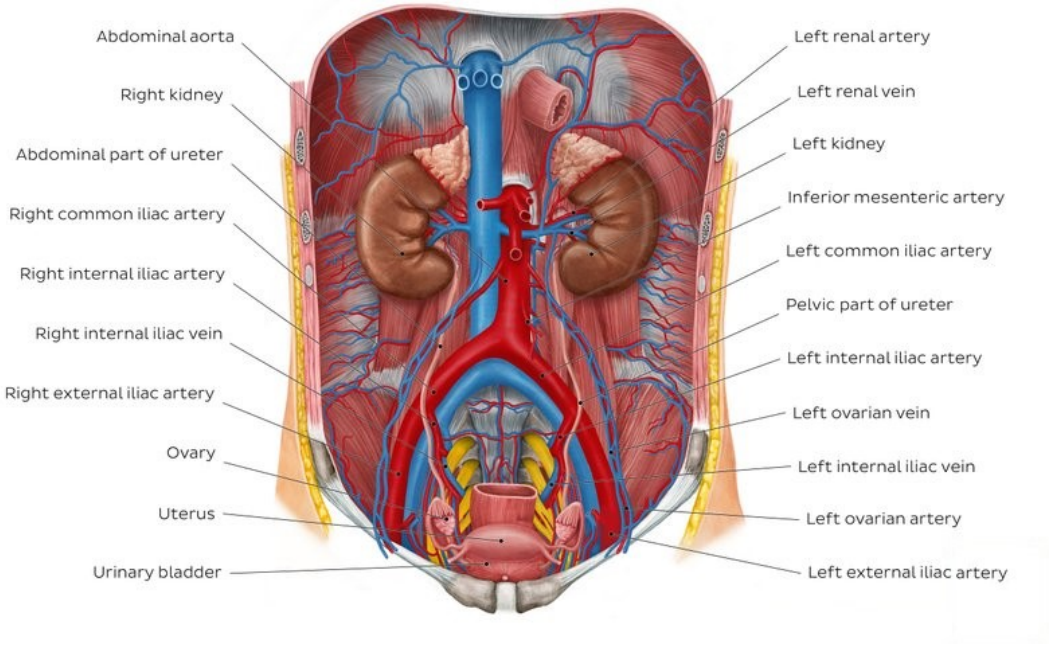

FIGURE 1.3: Anterior view of the anatomy inside the abdomen and pelvic cavity, showing the pelvic arteries, veins and ureters.

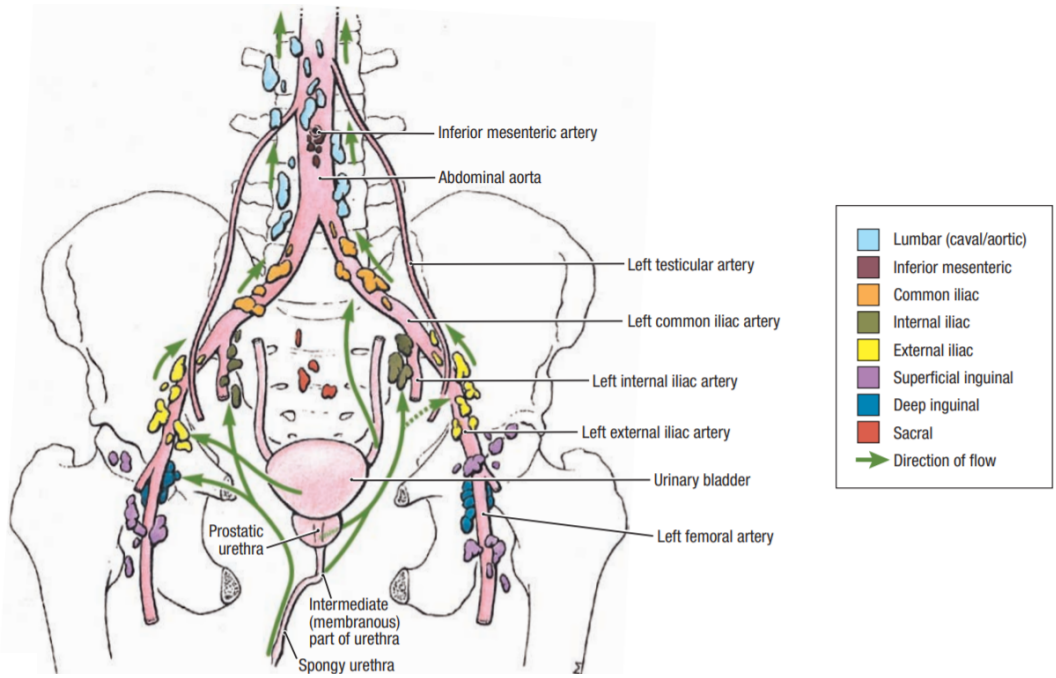

FIGURE 1.4: Anterior view of the lower abdominal lymphatic system including the pelvic arteries and several lymph node stations [2].

Besides the primary cancer type, abdominal cancer could also involve metastasis to other organs or lymph nodes. The lymphatic system is one of the major routes in which the primary tumor could spread, since the main function of the lymphatic system is to drain fluids from tissue and cells after which it returns to the bloodstream. Therefore, lymph nodes located close to the primary tumor are vulnerable to be involved and could be malignant as well [7].

For surgical navigation, colorectal cancer is the most applicable abdominal cancer type when the tumor is located in the rectum or distal sigmoid, since these structures lie relatively rigid in the pelvic cavity. Besides the primary cancer type, malignant lymph nodes in the pelvic cavity are relevant for surgical navigation as well, since most lymph node stations are located near rigid structures, such as the aorta or iliac arteries. In practice, surgical navigation is mostly applied for the removal of malignant lymph nodes, since they could be small and difficult to find.

1.1.3 Diagnosis of abdominal cancer

Many diagnostic tests are available that could diagnose various abdominal cancer types. Clinicians choose these tests depending on several factors, such as the suspected cancer type, the patient's symptoms and medical history. Some commonly applied diagnostic tests are a colonoscopy, blood test, biopsy and imaging techniques, such as computed tomography (CT), magnetic resonance imaging (MRI), ultrasound (US) and positron emission tomography (PET). For the diagnosis of colorectal cancer, a colonoscopy or sigmoidoscopy is the most common applied and efficient method [8]. The main advantage of this method is that the tumor can be localized and biopsied during the same examination. However, colonoscopy is an invasive method with a risk of complications, such as perforation or bleeding [8].

Another important diagnostic factor is tumor staging. This is mostly performed using the TNM classification system. This classification method describes the extent of the primary tumor (T), the presence and extent of tumor metastasis to regional lymph nodes (N) and the presence of distant metastasis (M) [9]. Imaging techniques, such as PET combined with CT (PET-CT), are useful in tumor staging and analyzing the presence of metastasis [8]. Staging of the diagnosed tumor is essential for patient survival prognosis and treatment planning [9].

For example, colorectal cancer is staged by combining the TNM classifications into the following five stages [10].

- Stage 0: Cancer in situ. The cancer cells are only located in the mucosa of the colon or rectum. (Tis, N0, M0)
- Stage 1: The cancer cells have invaded into the submucosa or muscular layer of the colon or rectum. (T1 or T2, N0, M0)
- Stage 2: The tumor invades through the muscular layer or further to the visceral peritoneum or other organs or structures. (T3 or T4a or T4b, N0, M0)
- Stage 3: Metastasis to one or more regional lymph nodes. (any T, any N, M0)
- Stage 4: The tumor has spread to one or more distant parts of the body. (any T, any N, M1)

1.1.4 Treatment of abdominal cancer

Abdominal cancer treatment depends on several factors, such as the cancer type, the stage of the tumor and the patient's condition [11]. In addition, the aim of the treatment could differ between cure or palliation. Surgery and a combination with radiotherapy and/or chemotherapy is commonly applied, especially when the tumor and possibly present metastasis are resectable [12].

About 80% of the patients diagnosed with colorectal cancer undergo surgery [1]. During colon cancer surgery, the malignant part of the colon is removed by a segmental resection and a restorative anastomosis. For rectal cancers, a total mesorectal excision is required, which removes the tumor and the surrounding mesorectal tissue. Abdominoperineal resection (APR) is performed for tumors within 5 cm of the anal margin, resulting in a permanent stoma for the patient. Otherwise, low anterior resection (LAR) could be performed, which connects the colon to the remaining section of the rectum after tumor resection. Other examples of abdominal tumor surgery are a prostatectomy, total mesorectal excision (TME) or lymph node dissection (LND) [1].

Surgery could be performed laparoscopically or conventionally with the open approach. The laparoscopic technique is widely applied because of its short-term advantages in smaller incisions, shorter hospitalization and faster recovery [13], [14]. However, this approach could be more difficult on patients who underwent radiotherapy or prior surgeries, due to the formation of adhesions or fibrosis. Oftentimes, this is the case for patients undergoing colorectal surgery in the Netherlands Cancer Institute-Antoni van Leeuwenhoek (NKI-AvL) in Amsterdam, which means that the conventional open approach is applied more frequently at this hospital. Long-term survival after colorectal cancer surgery depends on complete cancer tissue removal with adequate resection margins and malignant lymph node clearance [1]. Localizing the malignant tissue during surgery could be difficult, especially on patients with adhesions, fibrosis or shrunk tumor tissue due to (chemo)radiotherapy. Therefore, image guided surgery (IGS) and intra-operative navigation techniques, could aid the surgeon in localizing the tumor or malignant lymph node locations during surgery. In addition, this technique could improve the surgical resection margins while avoiding damage to critical structures, such as arteries or ureters, which might improve patient outcomes [15].

1.1.5 Image guided surgery

IGS is the technique of combining pre-operative imaging data, such as CT- and MRI-scans, with the intra-operative anatomy of the patient. In this manner, the pre-operatively determined tumor locations and critical structures could be visualized in real-time during surgery in relation to the patient's body. At the NKI-AvL, an IGS navigation technique has been developed and is currently applied as standard care for open tumor surgery in the lower abdominal and pelvic area [15]–[18]. They apply an electromagnetic tracking system (EMTS) with sensors on the patient to match and monitor the intra-operative orientation of the patient with pre-operative imaging data. The navigation user interface that is provided during surgery is shown in Figure 1.5. Here, a pre-operative CT-scan is visualized in three orthogonal views, following the surgeons pointer, including the segmentation of anatomical structures, such as bone, arteries, veins, ureters, nerves, lymph nodes and the tumor. A three-dimensional (3D) model of these structures is shown in the lower right corner of the screen. In addition, a model of the surgical pointer is shown relative to the segmented structures. The surgeon can move this surgical pointer inside the patient's body to validate its location in real-time during surgery [17].

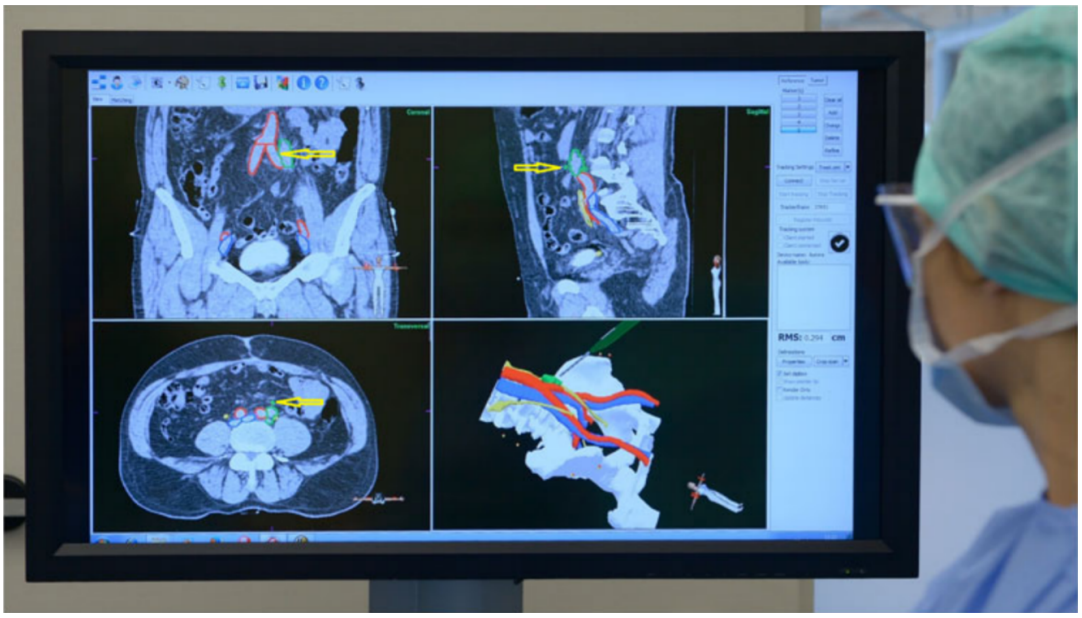

FIGURE 1.5: Intra-operative navigation user interface at the NKI-AvL. Three orthogonal views of a pre-operative CT-scan and a 3D model of five segmented structures are shown, namely bone (white), arteries (red), veins (blue), ureters (yellow) and a malignant lymph node (green). The surgical pointer is highlighted with yellow arrows in the CT-scan slices [17].

1.1.6 Clinical problem of image guided surgery

Before being able to use navigation during surgery, the intra-operative orientation of the patient needs to be matched to the pre-operative imaging data, which is performed through registration. Currently, three tracked patient sensors are attached to the patient's skin prior to the surgery at the height of the pelvic bone: two posterior and one anterior. Afterwards, registration is performed by scanning the patient on the operating room (OR) with a cone-beam CT (CBCT) and matching the acquired CBCT-scan with pre-operative imaging and electromagnetic (EM) tracking data from the patient sensors, which is clinically feasible [17]. However, this currently applied registration method has several limitations:

1. Oftentimes, the resulting navigation accuracy could be improved and a manual correction for the registration must be applied during surgery, which is not ideal.

2. CBCT-scanning must be performed with the surgical bed in a flat horizontal position, while frequently an alternative position is used during surgery.

3. Solely one hybrid OR with a CBCT is available at the NKI-AvL, which limits the application on surgeries that need to take place at other ORs, such as intra-operative radiotherapy.

4. The clinical workflow is fully interrupted during CBCT-scanning, since most staff members need to leave the OR during scanning.

5. Radiation exposure for the patient and some staff members.

Limitation 2 and 3 could be overcome by transferring the patient to another OR or tilting the surgical bed after CBCT-scanning. However, these actions could lead to a shift between the patient sensors and the surgical target area within the patient's body, resulting in navigation inaccuracies. For example, rotation of the surgical bed into Trendelenburg could cause the pelvic area of the patient to shift in cranial direction. Since the posterior patient sensors are located between the surgical bed and the patient's skin, they shift less than the pelvic area. In this situation, the true position of the surgical target area could be located more cranial than indicated by the navigation system.

Clinically, it is important to have a reliable registration and a high accuracy (within 5 mm) of the navigation system. If the accuracy during surgery decreases due to patient movement, the pointer location in the patient's body does not correspond with the location on pre-operative imaging. This could lead to useless navigation or maybe even incorrect tumor localization, resulting in worse patient outcomes. Therefore, an alternative registration method for CBCT is needed that could consistently reach accurate navigation regardless of the patient position during surgery.

The use of a tracked US device could provide a solution for the tracking inaccuracies caused by patient movement after CBCT registration, since an US scan can be acquired on every OR and after correctly positioning of the surgical bed before surgery. In addition, an intra-operative re-registration could be performed using a sterile covered tracked US device, which eliminates the need for a manual correction. Furthermore, potential structures used for registration, such as the pelvic bone, lie inside the patient's body, which is located closer to the surgical target area than the patient sensors in CBCT registration. Therefore, tracked US has the potential to consistently reach a high navigation accuracy regardless of external factors, such as the OR, surgical bed and patient position.

Practically, the workflow interruption would be minimal, since staff members do not need to leave the OR during US scanning. Moreover, US is a non-invasive method, removing the radiation exposure for the staff and patient. When expanding the abdominal navigation technique to other hospitals or robotic surgery, US is affordable and easier to implement. However, some potential disadvantages of tracked US are the required user experience and reduced image quality. It could be challenging to accurately visualize anatomical structures on US images due to noise or artifacts.

In conclusion, application of tracked US for patient registration might ease the clinical navigation workflow and improve the navigation accuracy during surgery regardless of the patient position, which could eventually lead to better surgical outcomes for abdominal cancer patients.

1.2 Technological background

1.2.1 Electromagnetic and optical tracking

The key component of surgical navigation is object tracking. In general, object tracking is a technology that can continuously measure the location and orientation of sensors in a specific field of view. Clinically, medical instruments or sensors could be measured relative to the orientation of the patient. This is needed to combine preoperative imaging data with the patient's anatomy during surgery. The two main tracking modalities are an EMTS and optical tracking system (OTS). An EMTS uses a field generator (FG) to create an EM field. The magnetic flux of the EM field is measured by EM sensors, which is used by the system to determine the distance to the source of the FG to define the position and orientation of the sensor in the reference frame of the EMTS. This means that hardware components, such as the FG, need to be located close to the patient where the sensors are measured. However, tracking accuracy of the EMTS could be influenced by external ferromagnetic objects, such as a CT scanner, surgical tools or a mobile phone [19]. An OTS uses cameras to visually localize markers within the operable area. These markers are wireless, while the EM sensors are mostly wired. Furthermore, the technical accuracy of the OTS is a little higher ($\pm$ 0.1 mm) than the EMTS [20], [21]. However, the optical markers must be located within the camera's line-of-sight to be detected by the OTS. This is not always feasible during surgery, especially when tracking surgical instruments inside the body of the patient [19].

1.2.2 Aurora electromagnetic tracking system

Therefore, an EMTS is currently applied for surgical navigation during abdominal cancer surgery in the NKI-AvL, namely the NDI Aurora V2 (Northern Digital Inc, Waterloo, Ontario, Canada) [22]. The Aurora tracking system consists of four main components: a FG, EM sensors, sensor interface units (SIUs) and a system control unit (SCU). The FG generates a low-intensity varying EM field in which the EM sensors can be detected. Two versions of the Aurora FG are shown in Figure 1.6: the tabletop field generator (TTFG) and the planar FG. The TTFG is mainly used for abdominal cancer navigation at the NKI-AvL, since it could be easily attached underneath the surgical bed before the start of the surgery. This FG creates an oval shaped EM field of 60x42x60 cm in which sensors could be tracked with an accuracy of 0.48 mm and 0.30 degrees [22]. However, no EM data can be measured in the first 12 cm directly on top of the TTFG.

The planar FG is a smaller portable variant, which can be moved around the patient before tracking. This FG creates a smaller EM field of 50x50x50 cm. Both FGs have a measurement rate of 40 Hz [22].

The EM field created by the FG induces small currents in EM sensors located inside this field. This information is send by the sensors as electric signals to the SIUs, which amplifies and digitizes them. Subsequently, this information is sent to the SCU, which controls the FG. The SCU can then calculate the position and orientation of every sensor and send it to the host computer. Both units are shown in Figure 1.7 [22].

Two types of EM sensors are available, namely five degrees of freedom (5DOF) and six degrees of freedom (6DOF) sensors. 5DOF sensors report the x-y-z position of the sensor and two of its orientations, pitch and yaw. 6DOF sensors provide an additional third orientation of the senor, which is called roll. Figure 1.8 shows a

FIGURE 1.6: The Aurora tabletop field generator (left) and planar field generator (right) [22].

FIGURE 1.7: The sensor interface unit (left) and the system control unit (right) [22].

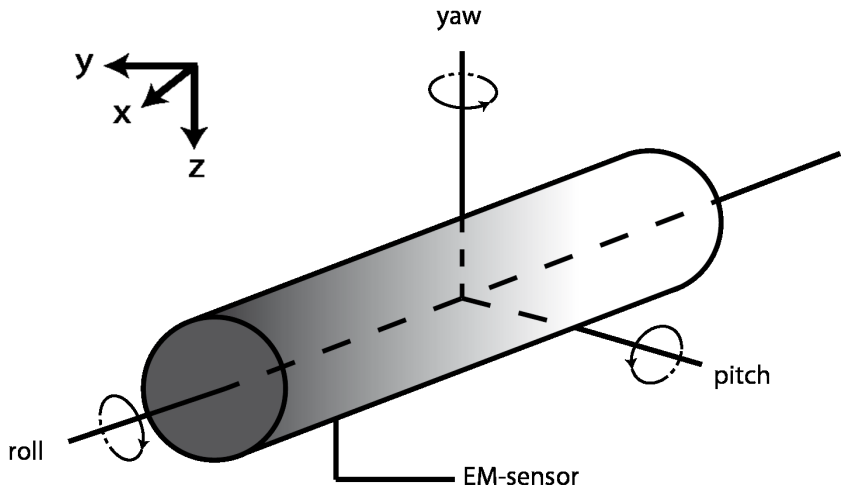

FIGURE 1.8: Schematic overview of a 6DOF sensor. Three locations (x, y, z) and three orientations (pitch, yaw, roll) are shown. A 5DOF sensor uses the same locations and orientations as the 6DOF sensor, but without the roll.

schematic overview of a 6DOF EM sensor and its orientations. Both sensor types are applied for surgical tumor navigation, for example the 5DOF Philips patient sensor and the 6DOF Aurora pointer. One Philips patient sensor consists of two 5DOF EM sensors, which are used to determine the position of the patient during surgery. The Aurora pointer has 6DOF and is used by the surgeon to navigate inside the patient's abdomen. Both sensors are shown in Figure 1.9. In addition, two other 6DOF EM sensors are visualized, namely a reference disk sensor (Figure 1.9c) and a cable tool sensor (Figure 1.9d). These two sensors could be applied for research purposes or to track several tools and devices, such as an US probe [23].

(A) Philips patient sensor (2x5DOF)

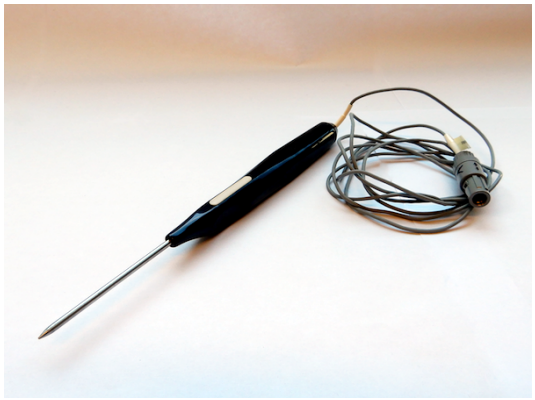

(B) Aurora pointer (6DOF)

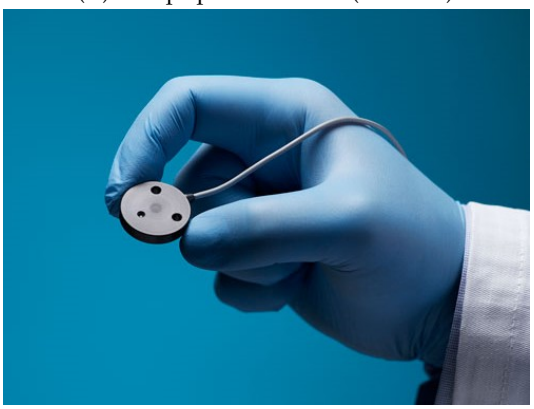

(C) Reference disk sensor (6DOF)

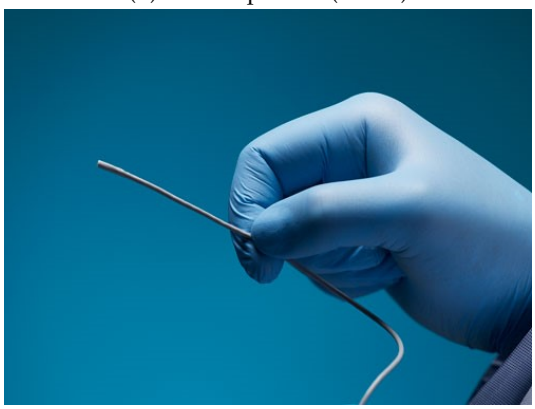

(D) Cable tool sensor (6DOF)

FIGURE 1.9: Four EM sensors of the NDI Aurora EMTS.

1.2.3 Surgical navigation workflow

The current workflow for surgical navigation at the NKI-AvL can be divided into several pre-operative and intra-operative steps. An overview of this workflow is visualized in Figure 1.10 [24].

Pre-operatively, contrast-enhanced CT-scans are made. These CT-scans and other imaging data of the patient, such as an MRI-scan, are used to create a 3D model. WrldMatch, an in-house developed software, is used to match the scans through rigid registration based on bone intensity. After this, all registered scans could be used to create the 3D model. This is done semi-automatically by segmenting several structures in the open source software 3D Slicer with segmentation tools such as thresholding. Afterwards, these segmented structures (bone, arteries, veins, ureters, nerves, lymph nodes and tumors) are combined into a 3D model. This model and the

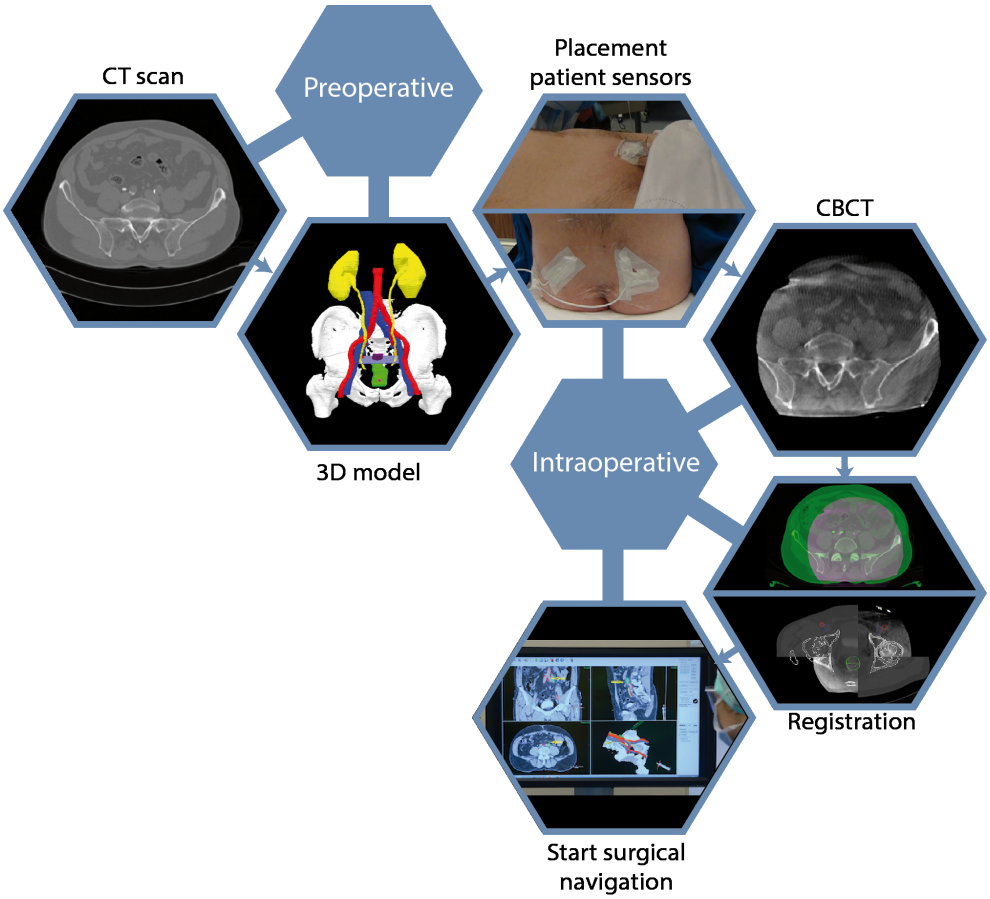

FIGURE 1.10: Schematic overview of the surgical navigation workflow [24].

patient imaging data are loaded into another in-house developed software, SurgNav, which is applied during surgery for surgical navigation (Figure 1.5). Finally, the TTFG is attached underneath the surgical bed and the EMTS is prepared [17].

Intra-operatively, three Philips patient sensors are attached to the skin of the patient at the level of the iliac crest, two at the back and one at the front. After patient anesthesia and positioning on the table, CBCT-scanning is performed on the OR. Because of the small field of view of the CBCT, two scans are made for all patient sensors to be imaged. Within WrldMatch, the CBCT-scans are registered with the pre-operative CT-scan based on bone anatomy of the pelvis. This registration connects the pre-operative imaging data and 3D model with the CBCT-scan. Afterwards, the electromagnetically measured locations of the Philips patient sensors are matched to the physical location on the CBCT-scan with a point registration method within SurgNav. Then, all imaging data is matched with the EMTS and surgical navigation can start [17].

1.2.4 CBCT registration method

Registration is the process of transforming data coordinates, such as images or point locations, from one coordinate system to another coordinate system. This process is necessary to combine spatial data from different measurements with each other [25]. For example, a CBCT image (A) could be rigidly registered to a CT image (B). This means that the best translation and rotation of the CBCT image data to the CT image data is found, depending on the registration settings. This process results in

a translation vector (${}^{B}t_{A}$) and rotation matrix (${}^{B}R_{A}$), which can be combined as a transformation matrix (${}^{B}T_{A} = \begin{bmatrix} {}^{B}R_{A} & {}^{B}t_{A} \\ 0 & 1 \end{bmatrix}$). ${}^{B}T_{A}$ describes the transformation from coordinate system A to B, which can be applied to transform points from CBCT coordinates (${}^{A}p$) to points in CT coordinates (${}^{B}p$) with the following equation: [26]

$$ {}^{B}p = {}^{B}T_{A}\,{}^{A}p \tag{1.1} $$

For surgical navigation, the same technique is applied to relate the EMTS coordinate system with the pre-operative CT coordinate system. Two registrations need to be performed, namely from EMTS to CBCT and from CBCT to CT. First, the CBCT is registered to the pre-operative CT using bone to bone registration within WrldMatch. This results in a transformation matrix (${}^{CT}T_{CBCT}$), which could transform data from CBCT coordinates (${}^{CBCT}p$) to CT coordinates (${}^{CT}p$) with Equation 1.2. Second, the EMTS is registered to the CBCT using EM patient sensor locations on both the CBCT-scan and the EMTS. The patient sensors on the CBCT are manually selected and the locations in EM coordinates are measured by the EMTS in real-time. With these locations, a fiducial registration using an iterative closest point (ICP) algorithm is applied, which results in a transformation matrix (${}^{CBCT}T_{EMTS}$). This transformation matrix transforms data from EMTS coordinates (${}^{EMTS}p$) to CBCT coordinates (${}^{CBCT}p$) in real-time with Equation 1.3. Eventually, Equation 1.2 and 1.3 could be combined to transform data from EMTS coordinates to CT coordinates directly (Equation 1.4). An overview of the OR set-up, coordinate systems and transformations are visualized in Figure 1.11.

$$ {}^{CT}p = {}^{CT}T_{CBCT}\,{}^{CBCT}p \tag{1.2} $$

$$ {}^{CBCT}p = {}^{CBCT}T_{EMTS}\,{}^{EMTS}p \tag{1.3} $$

$$ {}^{CT}p = {}^{CT}T_{CBCT}\,{}^{CBCT}T_{EMTS}\,{}^{EMTS}p \tag{1.4} $$

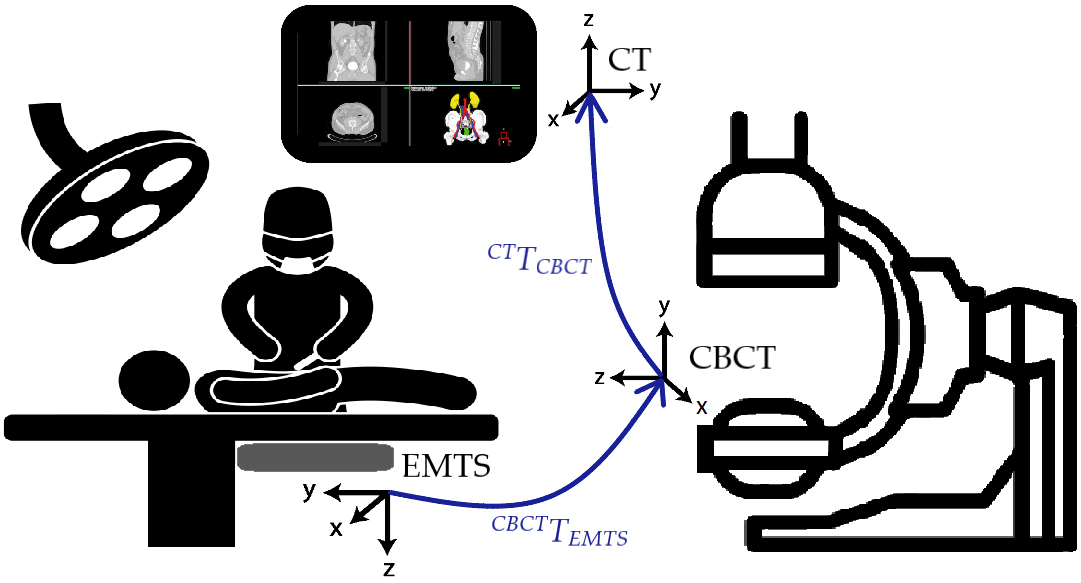

FIGURE 1.11: Overview of the coordinate systems and their transformations (blue) needed for CBCT registration.

1.2.5 Ultrasound imaging technique

US imaging applies the technique of sending pulses of sound waves from a transducer at high frequencies, above 20 kHz, into tissue and receiving reflections of these sound waves, which are turned into a two-dimensional (2D) image. The longitudinal sound waves sent by the transducer propagate through tissue at different wavelengths depending on its velocity and frequency. These waves lose energy while propagating through tissue, which is called attenuation. Attenuation is caused by two mechanisms, scattering and absorption. Scattering occurs at the transition location between two tissue types due to a difference in acoustic impedance. For example, a transition to bone causes a high acoustic impedance change, leading to scattering and reflection of the sound waves towards the transducer, resulting in a higher image intensity. Absorption depends on the tissue type and the ultrasonic wave frequency. A higher frequency results in more absorption, thus a higher ultrasonic wave energy loss. When most energy of the propagating wave is lost due to attenuation, no reflective signal can return to the transducer for deeper tissues. This means that a lower US frequency is needed for the imaging of deeply located structures, because less energy will be lost due to absorption. However, lower frequencies result in a decreased spatial resolution of the US image [27].

Each US device uses a specific speed of sound (SOS) for the reconstruction of B-mode images. This assumed SOS (c) with the measured propagation time of sound waves (t) is used to compute the distance (d) between the US probe surface and the reflected targets with the following equation [28]:

$$d = t \cdot c/2 \tag{1.5}$$

Most US devices assume a SOS of 1540 m/s, which is the average SOS in human tissue. However, each tissue type has a different SOS varying from approximately 1450 m/s in fat to 1600 m/s in muscles and 4080 m/s in bone, which might cause speed displacement artifacts on the US image. For example, when imaging through fat tissue, sound waves travel slower than the SOS assumed by the US device, which causes the echoes to be displayed deeper than their actual depth [29].

1.2.6 Tracked ultrasound registration

To perform surgical navigation through US registration, it is essential to know the location of the US images relative to the patient. The location of the US probe could be measured by an EM sensor that is attached to the probe. At the NKI-AvL, extensive research has already been performed on tracking a BK T-shaped intra-operative US transducer (I14C5T, BK Medical, Peabody, USA) for the application in tracked liver surgery. They use a 3D printed clip to rigidly attach the EM sensor to the US probe, which is visualized in Figure 1.12. In this manner, the position of the US image relative to the EM sensor attached to the US probe is always constant. This static transformation from US image to EM sensor (${}^{EMsens}T_{USim}$) could be calculated by spatial probe calibration [30]. Further elaboration on the calibration process will be given in Chapter 3. Real-time tracking data of the EMTS provides the transformation from the EM sensor to the EMTS (${}^{EMTS}T_{EMsens}$). When ${}^{EMsens}T_{USim}$ is known, the location of the US image could be tracked in EMTS coordinates relative to other EM sensors. Finally, the EM data needs to be matched to the pre-operative CT with the transformation ${}^{CT}T_{EMTS}$. This transformation is computed by matching points in the US image (${}^{USim}p$) with points in the pre-operative CT-scan (${}^{CT}p$). An overview of

the transformations needed for tracked US registration is shown in Figure 1.13 and Equation 1.6.

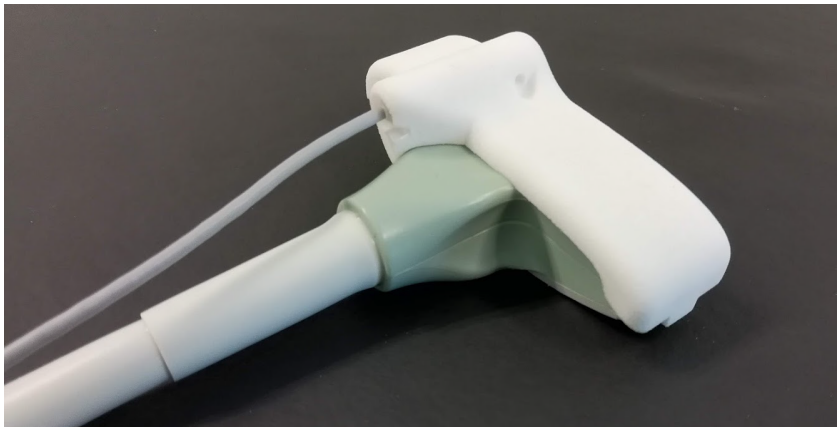

FIGURE 1.12: BK T-shaped intra-operative US probe with an attached clip with EM sensor [24].

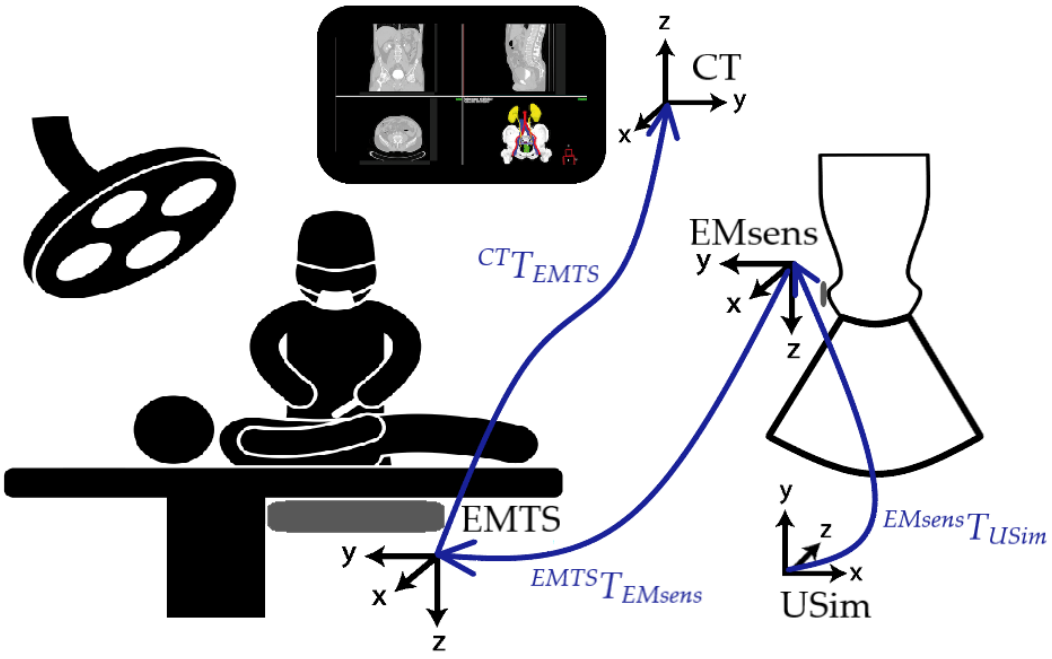

FIGURE 1.13: Overview of the coordinate systems and their transformations (blue) needed for registration with tracked US.

$$^{CT}p = {}^{CT}T_{EMTS}\,{}^{EMTS}T_{EMsens}\,{}^{EMsens}T_{USim}\,{}^{USim}p \tag{1.6}$$

Intra-operatively, one transformation ($^{CT}T_{EMTS}$) is unknown and needs to be calculated through registration of specific targets. These registration targets should be anatomical structures that lie rigidly within the operable area. A commonly used registration target is bone, because of its rigidity relative to the patient's anatomy. On US imaging, bone surface could be clearly visualized because of its high attenuation. Therefore, the pelvic bone could be a proper target for US registration in abdominal tumor surgery. An alternative registration target could be the aortic artery

and its bifurcation into the common iliac arteries. US flow measurements could be applied to visualize these arteries and they lie relatively rigid within the pelvic area.

US imaging of the bone surface is more difficult than performing a CBCT-scan. Some general drawbacks of the US technique are the high levels of noise, a limited field of view and several possible artifacts. Furthermore, the manner of US scanning and orientation of the probe relative to the patient highly influences the image quality, which makes the scanning process user dependent. This problem is visualized in Figure 1.14, where three US images of the same bone surface are shown. The right image shows an ideal image of a typically high intensity bone surface with a shadow region underneath. The other two images show that an alternate probe orientation could cause a reduced intensity of the bone (left) or less shadow (middle), which makes it harder to accurately define the bone surface for the registration procedure. The best image quality is acquired when scanning orthogonal to the surface of the bone. Therefore, some US scanning experience by the user is required for optimal data collection, which is needed for accurate registration [31].

Other factors that could influence the bone intensity on US images is a reduced bone density due to age or previous treatment, such as radiotherapy. Oftentimes, patients with abdominal cancer undergoing navigated surgery at the NKI-AvL are relatively old and received earlier treatment. In addition, orthogonal positioning of the US probe could be more difficult on patients with an increased amount of fat tissue. Therefore, it might be challenging to accurately visualize the bone surface on US for these patients.

FIGURE 1.14: Three US images of the same bone surface at different probe orientations relative to the patient. A low bone intensity (left), less shadow (middle) and ideal image (right) is shown [31].

1.2.7 Previous research

In previous research at the NKI-AvL, the feasibility of 3D tracked US registration has been tested on a phantom with pelvic bone [24]. Bone registration was performed with an ICP algorithm. The accuracy results were compared with the current gold standard, namely CBCT registration. A similar target registration error (TRE) for tracked US registration compared with CBCT registration was found when the left and right iliac crest and the pubic bone were used for US registration. While this study showed promising results, the registration accuracy might differ when scanning patients instead of a phantom due to different overlaying structures, such as fat and muscles. Therefore, the feasibility of using tracked US on patients for registration will be evaluated in this study.

1.2.8 Clarius wireless ultrasound transducer

The previously used transducer, the BK T-shaped intra-operative probe, is primarily designed for hepatic surgery, focusing on lesion detection and classification. Other transducers might result in easier or more accurate US bone scanning, which could improve the registration. Therefore, a new wireless US transducer was purchased at the NKI-AvL specifically for this study, which is the Clarius C3 HD probe (Clarius Mobile Health Corporation, Burnaby, Canada), shown in Figure 1.15. This transducer has a frequency range of 2-6 MHz and a maximum depth of 40 cm. The main advantage of this transducer is that it is wireless, easy to use and has data connectivity through Wi-Fi [32]. Additionally, the C3 HD probe has an embedded 9DOF inertial measurement unit (IMU) that measures gyroscope, accelerometer and magnetometer information in x, y and z axes. This data might provide additional information about the location and orientation of the probe, which could be useful for more accurate tracking of the device [33]. Furthermore, real-time elastography is available on the Clarius probe. This technique measures the elasticity and stiffness of tissue on US images, which might be useful in the visualization and segmentation of stiff bone [34].

FIGURE 1.15: The Clarius C3 HD probe. The ultrasound image is visualized on a mobile phone [32].

1.3 Research objectives

Primary objective

The main goal of this study is to evaluate the feasibility and accuracy of EM tracked US registration in patients and investigate how this technique could be implemented into clinical practice with the aim to potentially replace the CBCT registration method for abdominal tumor navigation surgery in the future.

Secondary objectives

To reach the described goal, technical implementation of the Clarius wireless US probe is necessary to be able to electromagnetically track the US device. Furthermore, a patient study will be performed to assess the US registration accuracy and clinical feasibility. This results in the following secondary objectives:

1. Examine the EM tracking accuracy when using the Clarius wireless US probe in combination with the EMTS and find a suitable fixation position for the EM sensor on the US probe.
2. Calibrate the wireless US probe with the EMTS with a maximum calibration error of 5 mm.
3. Assess the accuracy of the tracked US registration technique at clinical targets by comparing it with the CBCT registration method on patients undergoing abdominal cancer surgery.
4. Determine the influence of a patient position rotation into 10 degrees Trendelenburg on the US registration outcome.

Chapter 2

Accuracy evaluation of electromagnetically tracked ultrasound

2.1 Introduction

Immediate clinical implementation of an electromagnetically tracked US system is not possible due to the unknown tracking accuracy of the system and patient safety. The EM tracking accuracy is dependent on internal specifications of the EMTS and on external materials that could interfere with the EMTS, such as ferromagnetic objects or electrical devices. These external materials and devices might cause distortions when introduced into the EM field, which influences the measured position and orientation data from EM sensors [35], [36]. Consecutively, a high EM tracking error will propagate through the registration procedure, which would strongly decrease the surgical navigation accuracy. Therefore, the accuracy of the EMTS after introducing new devices, such as an US probe, into the EM field should be evaluated prior to further clinical implementation.

In literature, extensive research has been performed on EM tracking accuracy and multiple different evaluation methods have been applied. To ensure comparability between various studies, Hummel *et al.* proposed a standardized assessment protocol for the evaluation of new EMTSs [37], [38]. In their research, a base plate with different positions and distances to the FG was used to determine the error between the tracked EM sensor position and the actual position within the base plate. For example, Maier-Hein *et al.* applied this standardized method to evaluate the NDI Aurora EMTS in a clinical setting [39]. When tracking in a clinical environment with a nearby CT-scanner, they measured a position error increase for the TTFG by a factor of 2.9 compared to the reference tracking accuracy. Still, the mean position error in a clinical environment was sub-millimetric (0.9 mm) and no significant increase in orientation error was found [39]. Nijkamp *et al.* evaluated the accuracy of different EM sensors for the Aurora TTFG by using a polycarbonate frame with stackable boxes to alter the distance to the TTFG [40]. They showed a sub-millimetric and sub-degree tracking accuracy for 6DOF and multiple combined 5DOF sensors within 30 cm of the FG. A 6DOF disk shaped sensor reached the highest tracking accuracy of all tested sensors [40]. Other research found that an increased sensor distance to the TTFG results in a higher error as well [41]. Therefore, it is important to focus on clinical relevant areas within the EM field when evaluating the EM tracking accuracy.

While the method proposed by Hummel *et al.* [37], [38] is convenient for static error measurements, it is not suitable when the EM sensor is moved while measuring.

Various error detection methods have been proposed for dynamic measurements, such as using a robotic system [42]. While a robotic system can accurately repeat several dynamic trajectories, the system itself might interfere with the EMTS due to metallic parts of the robot. Another proposed method for dynamic accuracy measurements is by combining the EMTS with an OTS to form a hybrid magneto-optical tracking system [40], [42], [43]. After calibration of both systems, the tracking error is the difference between the optical measurement and the EM measurement. This is a useful method when the tracked sensor needs to move freely within the EM field during error measurements. However, inaccurate calibration between both tracking systems could propagate to the measured tracking error and lead to unreliable results.

Up till now, no EM tracking accuracy evaluation has been performed for wireless US probes, such as the Clarius C3 HD probe. However, six conventional US probes have been evaluated with an NDI Aurora EMTS by Franz *et al.* [44] and three 3D US probes were evaluated by Hastenteufel *et al.* [45]. Both studies showed that the amount of interference highly depends on the used probe and tracking system. Overall, 3D US probes cause higher tracking errors than conventional 2D probes. Furthermore, the sensor position and orientation relative to the US probe has a major impact on the tracking accuracy [45]. Therefore, a suitable fixation position for the EM sensor needs to be found on novel tracked US probes to minimize tracking inaccuracies due to interference.

In this study, a wireless US probe (C3 HD, Clarius Mobile Health Corporation, Burnaby, Canada) will be tracked using a rigidly attached EM sensor for the patient registration prior to surgical navigation. This US probe contains several electrical parts and has data connectivity through Wi-Fi and bluetooth, which might interfere with the EMTS. Therefore, it is important to measure the extent of interference to find a fixation position for the EM sensor on the US probe where the tracking accuracy is acceptable.

In this chapter, EM tracking accuracy will be evaluated for the Clarius C3 HD probe. The result will be compared with two BK probes. First, static measurements will be performed to provide an overall indication of the maximum interference for every US probe. Second, static measurements will be done while varying the distance and location between the EM sensor and US probe. This provides an indication for suitable EM sensor fixation positions. Position error and jitter and orientation error and jitter is calculated by using a static measurement without US probe as ground truth. Third, a hybrid magneto-optical tracking system is created by calibrating an OTS with an EMTS, which is applied for dynamic measurements. These dynamic measurements are performed with the EM sensor fixed to the US probe at promising locations according to the static measurements.

2.2 Materials and methods

2.2.1 Hardware

The used EMTS was an NDI Aurora V2 TTFG with SIU and SCU. One EM sensor was used, namely a 6DOF reference disk sensor (Figure 1.9c). The used OTS was an NDI Hybrid Polaris Spectra system, which has an accuracy of <0.25 mm root-mean-square error (RMSE) [46]. Two optical tool frames were 3D printed from an open-source dynamic reference frame library to ensure that they do not interference with the EMTS [47]. Four passive reflective markers were rigidly attached to each optical tool. The accuracy measurements were performed for three US probes, namely a

wireless probe (C3 HD, Clarius Mobile Health Corporation, Burnaby, Canada), a curved array probe (6C2, BK Medical, Peabody, USA) and a T-shaped probe (I14C5T, BK Medical, Peabody, USA) (Figure 2.1).

FIGURE 2.1: A wireless US probe (left), a curved array US probe (middle) and a T-shaped probe (right).

The hybrid magneto-optical tracking measurement setup is visualized in Figure 2.2. For this setup, the polycarbonate frame with stackable boxes was used, which has been created by Nijkamp *et al.* [40]. This frame rigidly encases the TTFG, so no movement between the frame and the TTFG is possible. One optical tool (OPT_{FG}) was fixed onto the polycarbonate frame to enable optical tracking of the TTFG (Figure 2.2). The other optical tool (OPT_{sens}) was rigidly attached to the EM sensor (EM_{sens}), which resulted in a combined sensor (Figure 2.3). In this manner, the combined sensor could be tracked by the OTS and the EMTS simultaneously.

2.2.2 Software

The NDI toolbox software was used for initial evaluation of the measurement setup and tracking volumes. Both 3D printed optical tools were calibrated with NDI 6D architect software. After calibration, a maximum optical tracking error of 0.2 mm was achieved for each optical tool. The OTS and EMTS were connected to a notebook (Intel Core i5-7200U CPU @ 2.50 GHz; 8.00 GB RAM; 64-bit operating system) through USB 3.0 connections. Tracking data from the OTS and EMTS was received using PlusServer from the PLUS toolkit with a frame rate of 30 Hz [48]. The received data was send by PlusServer through OpenIGTLink and read into MATLAB (Release 2020a, The MathWorks, Inc., Natick, Massachusetts, USA). Within MATLAB, the calibration of the OTS with the EMTS and all further data evaluation was done. In addition, real-time visualization of tracking data was done in 3D Slicer version 4.10.2 with the SlicerIGT extension [49], [50].

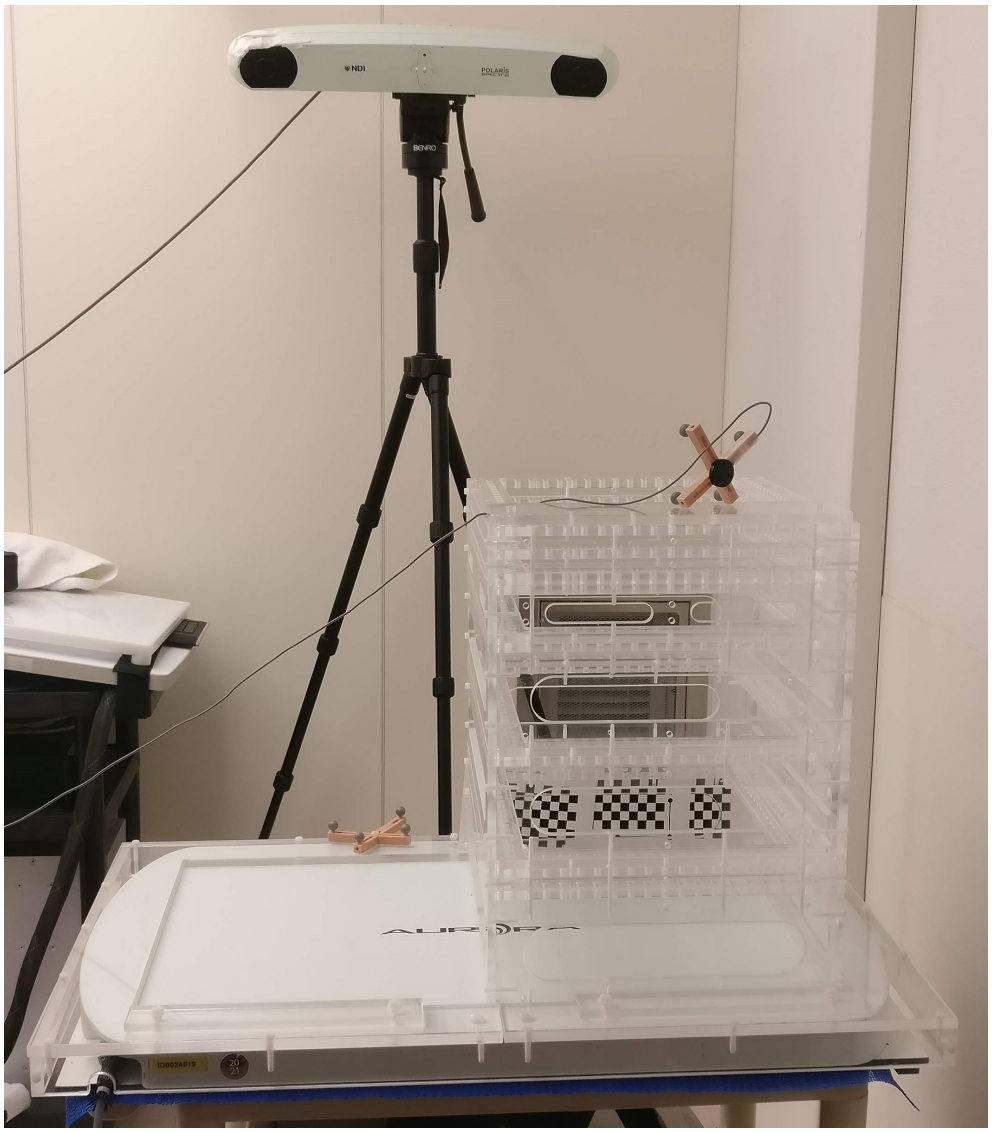

FIGURE 2.2: Hybrid magneto-optical tracking measurement setup with one optical tool attached to the TTFG case and the combined sensor located on top of the stacked boxes at 45 cm to the TTFG.

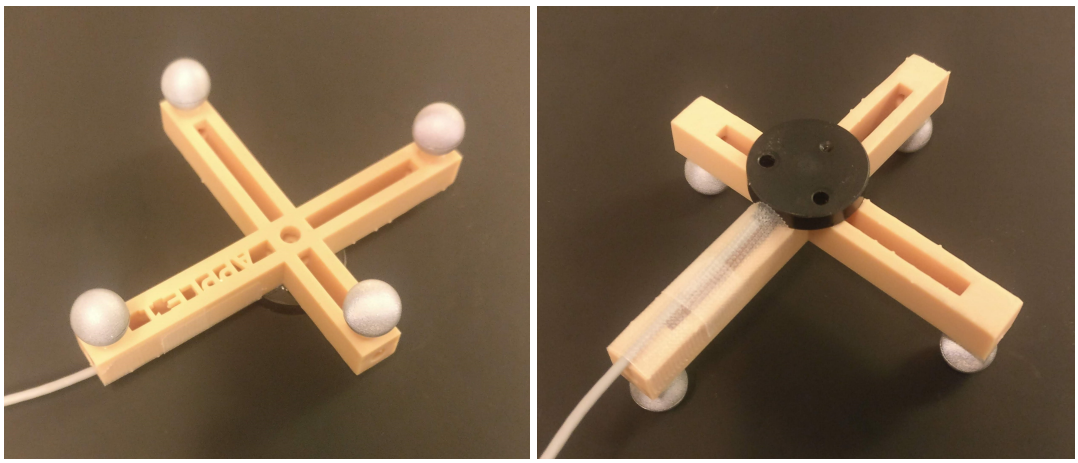

FIGURE 2.3: Front view (left) and rear view (right) of the combined sensor, which consists of a disk shaped EM sensor and an optical tool.

2.2.3 Error classification

Positional and orientational tracking inaccuracies were classified in two categories: jitter and error. The jitter describes the deviation of a static measurement over time, which is also known as the precision of the measurement. The error describes the accuracy of the measurement, which is a systematic difference between the measured and true value [42].

2.2.4 Calibration OTS with EMTS

In order to use optical tracking data as a validation for EM tracking data, the difference between the coordinate systems of the OTS and EMTS needed to be found. A schematic overview of the measurement setup, coordinate systems and corresponding transformations is visualized in Figure 2.4. During measurements, the OTS continuously measures the transformation from OPT_{sens} to OTS (${}^{OTS}T_{OPTsens}$) and from OPT_{FG} to OTS (${}^{OTS}T_{OPT_{FG}}$). The EMTS measures the transformation from EM_{sens} to $EMTS$ (${}^{EMTS}T_{EMsens}$). These three transformations change dynamically in real-time and are visualized in green in Figure 2.4. The other two transformations visualized in red, ${}^{OPTsens}T_{EMsens}$ and ${}^{EMTS}T_{OPT_{FG}}$, are the transformations from EM_{sens} to OPT_{sens} and from OPT_{FG} to $EMTS$, respectively. These transformations are static, initially unknown and need to be calculated through calibration.

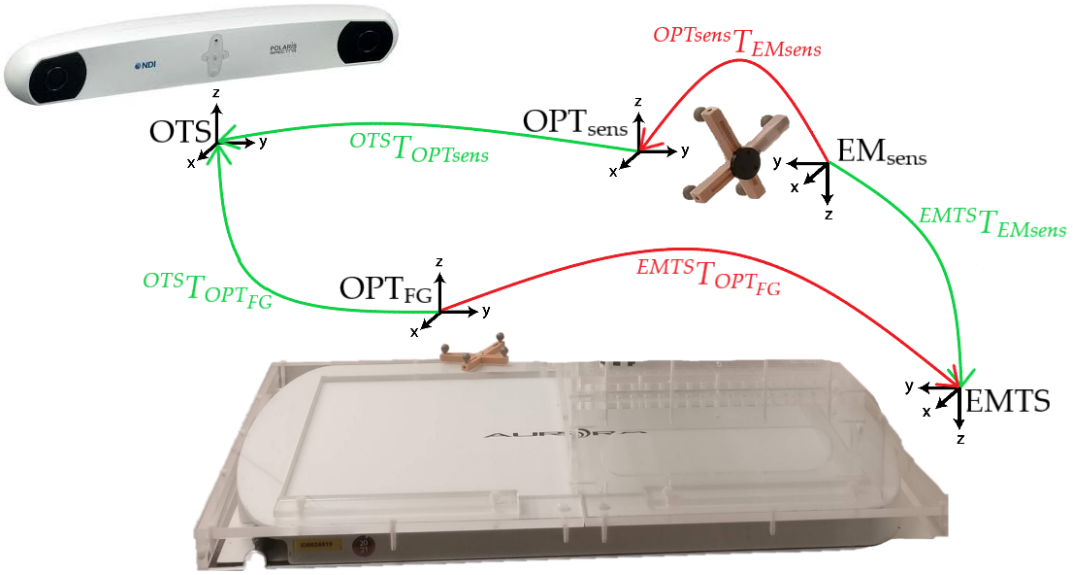

FIGURE 2.4: Schematic overview of the hybrid magneto-optical tracking measurement setup and its coordinate systems (black), measured dynamic transformations (green) and calibrated static transformations (red).

The calibration procedure consisted of three steps. First, hand-eye calibration was performed to compute an initial estimate of the unknown transformations ${}^{OPTsens}T_{EMsens}$ and ${}^{EMTS}T_{OPT_{FG}}$. Second, an optimization algorithm (Levenberg-Marquardt) was applied on the initial estimated transformations, which resulted in optimized transformations ${}^{OPTsens}T_{EMsens}$ and ${}^{EMTS}T_{OPT_{FG}}$. Third, temporal calibration was done, which corrects for the time difference between the OTS and the EMTS.

Hand-eye calibration

The hand-eye calibration method was originally developed for robotic systems to compute the transformation between the robotic gripper (hand) and the attached camera (eye) by collecting several camera and gripper motions [51], [52]. One of the most common mathematical representations of this method is:

$$AX = XB \tag{2.1}$$

In this equation, A represents the robotic gripper movement, B represents the camera movement and X represents the static transformation from the camera to the robotic gripper [52].

This method could be applied on hybrid tracking systems as well [42]. In this case, several poses i = 1,...,N of the combined sensor (OPT_{sens} and EM_{sens}) needed to be collected for the computation of transformations ${}^{OPTsens}T_{EMsens}$ and ${}^{EMTS}T_{OPT_{FG}}$. The combined sensor was positioned at N=27 different poses within the EM and optical field, without moving the optical camera and TTFG. At every pose, the transformations ${}^{OTS}T_{OPTsens}$, ${}^{EMTS}T_{EMsens}$ and ${}^{OTS}T_{OPT_{FG}}$ were measured by the tracking systems for 150 consecutive times and averaged to correct for jitter. Averaging of transformations was done by computing the mean of the translation and averaging quaternions for the rotation, as has been proposed by Markley *et al.* [53]. Between poses, the position and orientation of the combined sensor was altered maximally, which increases the robustness and precision of the hand-eye calibration. Afterwards, the averaged measurements ${}^{OTS}T_{OPTsens}(i)$ and ${}^{EMTS}T_{EMsens}(i)$ were used to compute the motion of the combined sensor ($T_{OPTsens}(i \rightarrow i+1)$ and $T_{EMsens}(i \rightarrow i+1)$) with Equation 2.2 and 2.3.

$$T_{OPTsens}(i \rightarrow i+1) = ({}^{OTS}T_{OPTsens}(i+1))^{-1} \; {}^{OTS}T_{OPTsens}(i) \tag{2.2}$$

$$T_{EMsens}(i \rightarrow i+1) = ({}^{EMTS}T_{EMsens}(i+1))^{-1} \; {}^{EMTS}T_{EMsens}(i) \tag{2.3}$$

At this point, the hand-eye calibration method from Equation 2.1 could be adapted for the hybrid tracking setup, since A represents the movement of OPT_{sens}, B represents the movement of EM_{sens} and X represents the unknown transformation ${}^{OPTsens}T_{EMsens}$. This results in the following equation for the computation of ${}^{OPTsens}T_{EMsens}$:

$$T_{OPTsens}(i \rightarrow i+1) \; {}^{OPTsens}T_{EMsens} = {}^{OPTsens}T_{EMsens} \; T_{EMsens}(i \rightarrow i+1) \tag{2.4}$$

The same measured data was used to compute the other unknown transformation ${}^{EMTS}T_{OPT_{FG}}$. This time, A represents the motion of the EMTS and B represents the motion of OPT_{FG}. These motions were computed as follows:

$$T_{EMTS}(i \rightarrow i+1) = {}^{EMTS}T_{EMsens}(i+1) \; ({}^{EMTS}T_{EMsens}(i))^{-1} \tag{2.5}$$

$$\begin{aligned} T_{OPT_{FG}}(i \rightarrow i+1) = &(({}^{OTS}T_{OPTsens}(i+1))^{-1} \; {}^{OTS}T_{OPT_{FG}}(i+1))^{-1} \\ &(({}^{OTS}T_{OPTsens}(i))^{-1} \; {}^{OTS}T_{OPT_{FG}}(i)) \end{aligned} \tag{2.6}$$

Subsequently, Equation 2.1 was adapted for the computation of the second static transformation (${}^{EMTS}T_{OPT_{FG}}$):

$$T_{EMTS}(i \rightarrow i+1) \ {}^{EMTS}T_{OPT_{FG}} = {}^{EMTS}T_{OPT_{FG}} \ T_{OPT_{FG}}(i \rightarrow i+1) \quad (2.7)$$

Several methods to find a solution for X in the hand-eye calibration problem (Equation 2.1) have been summarized by Shah *et al.* [52]. An open-source MATLAB package, which includes functions of these methods, was used to find the static transformations of Equation 2.4 and 2.7 [54]. All nine included methods were applied on the measured data and the calibration accuracy was evaluated for each method. Eventually, the method of Park and Martin showed the highest accuracy [55]. Therefore, this method was used for the hand-eye calibration of ${}^{OPTsens}T_{EMsens}$ and ${}^{EMTS}T_{OPT_{FG}}$.

Optimization algorithm

A Levenberg-Marquardt optimization algorithm was applied on the hand-eye calibrated transformations ${}^{OPTsens}T_{EMsens}$ and ${}^{EMTS}T_{OPT_{FG}}$ to further improve the calibration accuracy of the hybrid measurement setup. In an error-free measurement setup, the transformation ($T_\delta = \begin{bmatrix} R_\delta & t_\delta \\ 0 & 1 \end{bmatrix}$) from EM_{sens} to OPT_{sens} to OTS to OPT_{FG} to $EMTS$ to EM_{sens} should be an identity matrix (Figure 2.4 and Equation 2.8) [56].

$$T_\delta = ({}^{EMTS}T_{EMsens})^{-1} \ {}^{EMTS}T_{OPT_{FG}} \ ({}^{OTS}T_{OPT_{FG}})^{-1} \ {}^{OTS}T_{OPTsens} \ {}^{OPTsens}T_{EMsens} \quad (2.8)$$

However, errors in the translational (t_δ) and rotational (R_δ) component of T_δ could be caused by inaccurate calibration. Therefore, the calibration accuracy is described by the following cost function that weighs translational errors in millimeters to rotational errors in degrees (δ) [56]:

$$\delta = ||t_\delta|| + \frac{180}{\pi} \cdot arccos(\frac{trace(R_\delta) - 1}{2}) \quad (2.9)$$

The Levenberg-Marquardt algorithm was applied on the previously measured data using the hand-eye calibrated transformations as initial parameters. The cost function δ was minimized iteratively to compute the optimized transforms ${}^{OPTsens}T_{EMsens}$ and ${}^{EMTS}T_{OPT_{FG}}$.

Temporal calibration

Temporal calibration was done using fCal software, which comes with the PLUS toolkit. The combined sensor was manually moved vertically up and down through the EM field at an approximately constant speed while measuring the position of OPT_{sens} and EM_{sens}. This process was repeated three times and the resulting time offsets, which were computed by fCal, were averaged. However, only a small time offset between both tracking systems was found (5 ms), which could be neglected. Therefore, no temporal correction between the OTS and EMTS was made.

2.2.5 Calibration accuracy of magneto-optical tracking setup

To evaluate the accuracy of the calibrated hybrid measurement setup, static measurements were performed on 68 positions throughout the EM field of the TTFG. The polycarbonate frame was used to create 5x3x4 (length, width, height) measurement locations using the same measurement setup as during the calibration procedure

(Figure 2.2). Since the EM field of the TTFG is shaped like an ellipse, eight additional locations were selected, namely four at both edges in the length of the TTFG and one at every height. For every position, the combined sensor was similarly oriented and 150 consecutive transformations of the EM sensor and optical tools were measured by the EMTS and OTS. Afterwards, the transformation from EM_{sens} to $EMTS$ measured by the EMTS ($T_{EM} = \begin{bmatrix} R_{EM} & t_{EM} \\ 0 & 1 \end{bmatrix}$) and the same transformation measured by the OTS ($T_{OPT} = \begin{bmatrix} R_{OPT} & t_{OPT} \\ 0 & 1 \end{bmatrix}$) were computed (Equation 2.10 and 2.11).

$$T_{EM} = {}^{EMTS}T_{EMsens} \tag{2.10}$$

$$T_{OPT} = {}^{EMTS}T_{OPT_{FG}} \ ({}^{OTS}T_{OPT_{FG}})^{-1} \ {}^{OTS}T_{OPTsens} \ {}^{OPTsens}T_{EMsens} \tag{2.11}$$

The calibration accuracy was evaluated by comparing T_{OPT} with T_{EM}. For all 68 measured locations (j), the average of the 150 measured transformations was computed (T_{OPTm} and T_{EMm}). Afterwards, the position error and orientation error were computed for every location j with Equation 2.12 and 2.13. The position error (E_{pos}) is defined as the euclidean distance between the mean position measured by the OTS ($t_{OPTm} = (x_{OPTm}, y_{OPTm}, z_{OPTm})^T$) and the mean position measured by the EMTS ($t_{EMm} = (x_{EMm}, y_{EMm}, z_{EMm})^T$) [57]. For the computation of the orientation error (E_{or}), the rotation matrices (R_{OPTm} and R_{EMm}) were defined as quaternions (q_{OPTm} and q_{EMm}). Then, the orientation error, which is the angle between both quaternions in degrees, is computed using Equation 2.13, where $vec(q_{OPTm} * {q_{EMm}}^{-1})$ denotes the vector part of the quaternion product [58]. Afterwards, the RMSE of the whole tracking volume was calculated for the position and orientation error using Equation 2.14 [57].

$$E_{pos}(j) = ||t_{OPTm}(j) - t_{EMm}(j)|| \tag{2.12}$$

$$E_{or}(j) = \frac{180}{\pi} \cdot 2 \cdot arcsin(||vec(q_{OPTm}(j) * q_{EMm}(j)^{-1})||) \tag{2.13}$$

$$RMSE = \sqrt{\frac{1}{n}\sum_{j=1}^{n} E(j)^2} \tag{2.14}$$

In addition, the position and orientation jitter of T_{EM} and T_{OPT} for $k = 1, ..., 150$ were computed using Equation 2.15 and 2.16. The position jitter ($E_{posjitter}$) is defined as the root mean square of the euclidean distance between the mean position (t_{mean}) and every measured position ($t(k)$). The orientation jitter ($E_{orjitter}$) is computed by the root mean square of the angular difference between the mean orientation (q_{mean}) and every measured orientation ($q(k)$) [42].

$$E_{posjitter} = \sqrt{\frac{1}{n}\sum_{k=1}^{n} ||t_{mean} - t(k)||^2} \tag{2.15}$$

$$E_{orjitter} = \sqrt{\frac{1}{n}\sum_{k=1}^{n} (\frac{180}{\pi} \cdot 2 \cdot arcsin(||vec(q_{mean} * q(k)^{-1})||))^2} \tag{2.16}$$

2.2.6 EM tracking accuracy measurements with US probe

The performed measurements with the US probes have been divided into three trials. First, an initial indication of the maximum amount of interference caused by the three selected US probes was given. Second, the influence of various distances and locations between the EM sensor and the wireless US probe on the caused interference was measured. These measurements provided an indication for suitable EM sensor fixation positions for the following trial. Third, the combined sensor was attached to the wireless US probe using a 3D printed clip and measurements were performed while moving the US probe with attached sensor through the EM field.

All measurements were performed on the OR on a plastic table without external distortion. For trial 1 and 2, the EM sensor was fixed to the polycarbonate frame in the middle of the EM field at a height of 25 cm to the TTFG. Before both trials, an undistorted measurement of the EM sensor was performed (T_{EM0}), which served as a reference measurement. The transformation ${}^{EMTS}T_{EMsens}$ was measured 150 consecutive times and averaged to correct for jitter, resulting in T_{EM0}. Only static measurements were performed in trial 1 and 2, while trial 3 consisted of dynamic measurements. Therefore, the optical tracking data was only used for trial 3.

Trial 1: Maximum EM tracking interference of different US probes

In the first trial, the overall influence of the three US probes (wireless, T-shaped and curved array) on the EM tracking accuracy was measured. Each US probe was individually moved around the fixed EM sensor, while randomly varying the orientation, location and distance to the EM sensor. For each US probe, this process was repeated in three modes, namely the US probe and system turned off (off), the US probe and system turned on with a frozen US image (on) and the US probe and system turned on while acquiring US images (active).

During each measurement, ${}^{EMTS}T_{EMsens}$ was continuously measured for $l = 1, ..., 1000$ times, resulting in T_{EM} (Equation 2.10). The position and orientation error were computed by the euclidean distance and angular difference between the reference T_{EM0} and each measured transformation $T_{EM}(l)$ with:

$$E_{pos}(l) = ||t_{EM0} - t_{EM}(l)|| \tag{2.17}$$

$$E_{or}(l) = \frac{180}{\pi} \cdot 2 \cdot arcsin(||vec(q_{EM0} * q_{EM}(l)^{-1})||) \tag{2.18}$$

From these results, the maximum position and orientation error was acquired for each measurement. In addition, the position and orientation jitter were computed using Equation 2.15 and 2.16.

Trial 2: Evaluate sensor fixation positions on wireless US probe

Nine possible fixation positions of the EM sensor relative to the wireless US probe are visualized in Figure 2.5. Location 1-3, 4-6 and 7-9 are located at the side, front and diagonal of the US probe, respectively. Since the EM sensor was fixed on the polycarbonate frame, the orientation of the US probe was altered between measurements. The scanning surface of the US probe was always directed towards the TTFG, which resembles a clinical scanning situation. For each possible fixation position, ten measurements with increasing distance of the US probe to the EM sensor (1-10 cm) were performed. For every measurement, the US probe was held statically

and ${}^{EMTS}T_{EMsens}$ was continuously measured 150 times. During all measurements, the US probe was turned on and acquiring US images. The measurement setup for this trial is visualized in Figure 2.6, in which the sensor is located at location 1 at a distance of 5 cm.

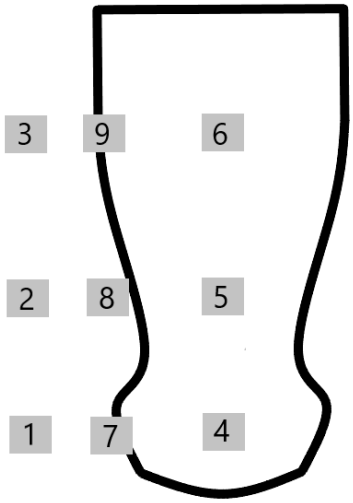

FIGURE 2.5: Nine EM sensor locations at the side (1-3), front (4-6) and diagonal (7-9) of the US probe.

FIGURE 2.6: Measurement setup for trial 2. The EM sensor is located on location 1 at 5 cm distance of the US probe.

Evaluation of trial 2 was done by computing the mean position and orientation error for every measurement position similar as for trial 1 with Equation 2.17 and 2.18. Additionally, the position and orientation jitter were computed using Equation 2.15 and 2.16.

Trial 3: Dynamic measurements with wireless US probe

Dynamic measurements were performed with the hybrid magneto-optical tracking setup and stackable boxes (Figure 2.2). Firstly, solely the combined sensor was moved through the EM field, which functioned as a reference measurement. Secondly, the combined sensor was attached to the wireless US probe with a 3D printed clip (Figure 2.7) and the same movements as for the reference measurement were repeated while the US probe was turned on and set into scanning mode. The combined sensor was attached at a distance of 6.5 cm to the probe on location 4 (Figure 2.5), since the results of trial 2 indicated low tracking interference at that location while maintaining an acceptable distance of the EM sensor to the US image. As additional comparison, the combined sensor was attached on 4.5 cm distance to the US probe as well with a different clip. All measurements were repeated to check the variability between measurements.

Three separate trajectories were executed, namely a square shaped trajectory at a height of 20 cm to the TTFG, the same square shaped trajectory at a height of 40 cm to the TTFG and random movements at clinically relevant positions within the EM field. Each square shaped trajectory was reproduced by following the edges of the stacked boxes at the specified height. The clinical relevant positions were selected where US measurements will be performed for registration prior to surgical navigation, which is at the os ilium and os pubis of patients.

FIGURE 2.7: The combined sensor attached to the wireless US probe on location 4 at a distance of 6.5 cm using a 3D printed clip.

Evaluation of trial 3 was done by comparing the potentially distorted measurement T_{EM} with the undistorted measurement T_{OPT}. The position and orientation error were computed with Equation 2.12 and 2.13 and the RMSE of both errors was computed for each trajectory using Equation 2.14. Since the transformations were dynamically collected, no average could be computed to correct for jitter. Further evaluation was done by visually comparing the measured trajectories of T_{EM} with T_{OPT}.

2.3 Results

2.3.1 Calibration accuracy of magneto-optical tracking setup

Initially, the hand-eye calibration method of the OTS and EMTS resulted in a mean position RMSE of 1.7 mm (range 0.6-2.8) and a mean orientation RMSE of 0.5 degrees (range 0.2-1.1), for the 68 measured positions. After application of the optimization algorithm, the mean position and orientation RMSE improved to 0.7 mm (range 0.1-1.7) and 0.5 degrees (range 0.1-1.3), respectively. In Figure 2.8 the position and orientation error is visualized for all 68 measured positions in the EM field. The color at each position represents the position and orientation error in mm and degrees, respectively. Both errors, but mainly the position error, are higher at the edges of the EM field than in the center (x- and y-axis). Also, an increased distance to the TTFG (z-axis) results in a higher position error. When only measuring the 27 positions that form a 3x3x3 cube in the center of the EM field, the mean position RMSE is 0.4 mm (range 0.1-0.6) and the mean orientation RMSE is 0.5 (range 0.2-0.6).

The position and orientation jitter of the transformations measured by the EMTS (T_{EM}) are visualized in Figure 2.9 for the same 68 measurement positions. The position jitter varies from 0.0 to 0.5 mm and the orientation jitter from 0.0 to 0.3 degrees. Both jitter errors increase at a higher distance to the TTFG (z-axis). At the edges on of

the EM field on the y-axis, both jitter errors increase as well. For the transformations measured by the OTS (T_{OPT}), the maximum position jitter (range 0.1-0.2 mm) and orientation jitter (range 0.0-0.1 degrees) are lower than the maximum jitter errors of T_{EM}.

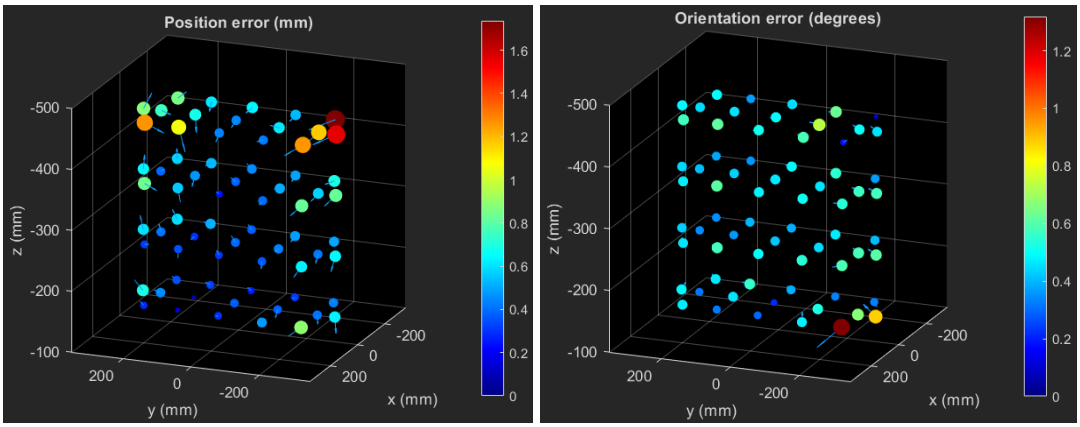

FIGURE 2.8: Calibration accuracy of the magneto-optical tracking setup. The position error in mm (left) and orientation error in degrees (right) are visualised for 68 measurement positions in the EM field. The TTFG is located at 0 mm on the z-axis. The direction of the position and orientation error is shown by a blue arrow.

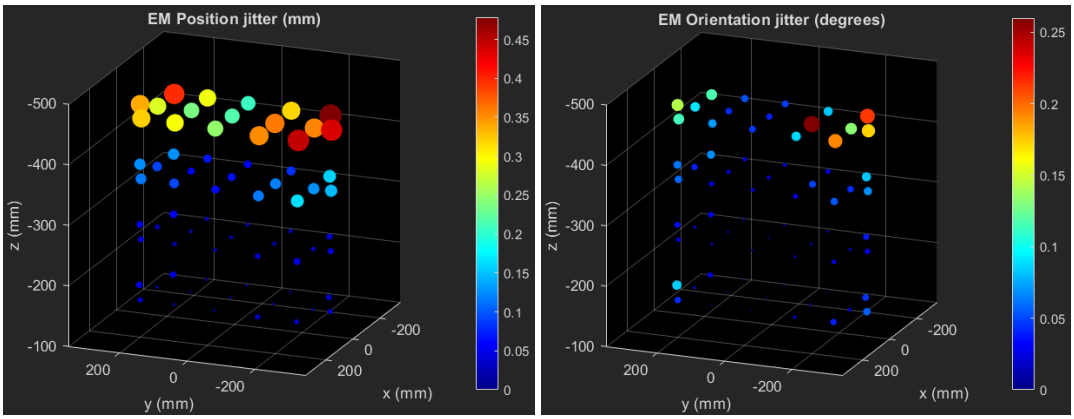

FIGURE 2.9: The position jitter in mm (left) and orientation jitter in degrees (right) of the EMTS at 68 measurement positions within the EM field. The TTFG is located at 0 mm on the z-axis.

2.3.2 EM tracking accuracy measurements with US probe

Trial 1: Maximum EM tracking interference of different US probes

A graphical summary of trial 1 is provided in Table 2.1. Here, the three US probes (wireless, T-shaped and curved array) could be compared to the reference with respect to the position and orientation jitter and the maximum position and orientation error and standard deviation (SD). The position and orientation jitter is comparable to the reference when using the T-shaped US probe. The curved array US probe causes a higher jitter error, but is still within 0.1 mm and 0.1 degrees. The wireless US probe causes a much higher jitter error of more than 1 mm and 1 degree.

Likewise, the maximum position and orientation error is much higher when using the wireless US probe (3.7 mm and 4.4 degrees), compared to the other two US probes (0.3 and 0.3 mm and 0.4 and 0.3 degrees). Turning the wireless probe on and setting it into scanning mode increases the maximum position and orientation error even more (4.5 mm and 7.7 degrees). For the T-shaped and curved array US probe, the maximum position and orientation errors do not increase when activating the US system and while in scanning mode.

TABLE 2.1: Measured position and orientation jitter and maximum position and orientation error ($\pm$ SD) for three US probes with respect to the distortion-free reference.

	Position jitter (mm)	Orientation jitter (degrees)	Max position error (mm)	Max orientation error (degrees)
Reference	0.0 ± 0.0	0.0 ± 0.0	0.0 ± 0.0	0.0 ± 0.0
Wireless, off	1.3 ± 0.8	1.1 ± 0.7	3.7 ± 0.9	4.4 ± 0.7
Wireless, on	1.8 ± 0.9	1.3 ± 0.8	5.8 ± 1.0	5.4 ± 0.8
Wireless, active	1.5 ± 0.9	1.2 ± 1.0	4.5 ± 1.0	7.7 ± 1.1
T-shaped, off	0.0 ± 0.0	0.0 ± 0.0	0.3 ± 0.0	0.4 ± 0.0
T-shaped, on	0.0 ± 0.0	0.0 ± 0.0	0.2 ± 0.0	0.2 ± 0.0
T-shaped, active	0.0 ± 0.0	0.0 ± 0.0	0.2 ± 0.0	0.2 ± 0.0
Curved array, off	0.1 ± 0.0	0.1 ± 0.1	0.3 ± 0.0	0.3 ± 0.1
Curved array, on	0.1 ± 0.0	0.1 ± 0.1	0.3 ± 0.0	0.3 ± 0.1
Curved array, active	0.1 ± 0.0	0.1 ± 0.1	0.3 ± 0.0	0.3 ± 0.1

Trial 2: Evaluate sensor fixation positions on wireless US probe

The results of trial 2 are visualized in Figure 2.10. Here, each subfigure represents an EM sensor fixation location relative to the US probe (Figure 2.5). At some measurement positions no data was collected, because the interference of the US probe significantly lowered the measurement rate of the EM sensor at these positions. In addition, the position and orientation error were mostly higher than 1 mm or 1 degree on these positions. Therefore, no error values were plotted in these cases in Figure 2.10, since these positions were certainly not suitable for EM sensor fixation.

For each of the nine locations, the measured error values decrease when increasing the distance between the US probe and the EM sensor. The influence on the measurement rate was higher at locations closer to the battery of the US probe (3,6,9) than at the scanning side (1,4,7). On average, the measured errors increase when locating the EM sensor closer to the battery of the US probe as well. The position and orientation jitter have the lowest values at location 1, 4 and 7.

When looking for suitable EM sensor fixation positions, location 1 on 10 cm probe-sensor distance has the lowest error values ($E_{pos} = 0.3$ mm and $E_{or} = 0.0$ degrees). However, when increasing the distance between the EM sensor and the US probe, the same orientation error could cause an increased position error at targets in the US image. When looking at the orientation error on location 1 and 4, increasing the probe-sensor distance more than 6 cm does not reduce the orientation error much further. Therefore, other positions with low errors are location 1 at $\geq$6 cm ($E_{pos} \leq 0.6$ mm and $E_{or} \leq 0.1$ degrees), location 4 at $\geq$6 cm ($E_{pos} \leq 0.5$ mm and $E_{or} \leq 0.1$ degrees) and location 7 at $\geq$8 cm ($E_{pos} \leq 0.4$ mm and $E_{or} \leq 0.2$ degrees). Out of these options, location 4 has the lowest position error at 6 cm probe-sensor

distance. At location 2, 3, 5, 6, 8 and 9, the position error is higher than 0.6 mm for every probe-sensor distance.

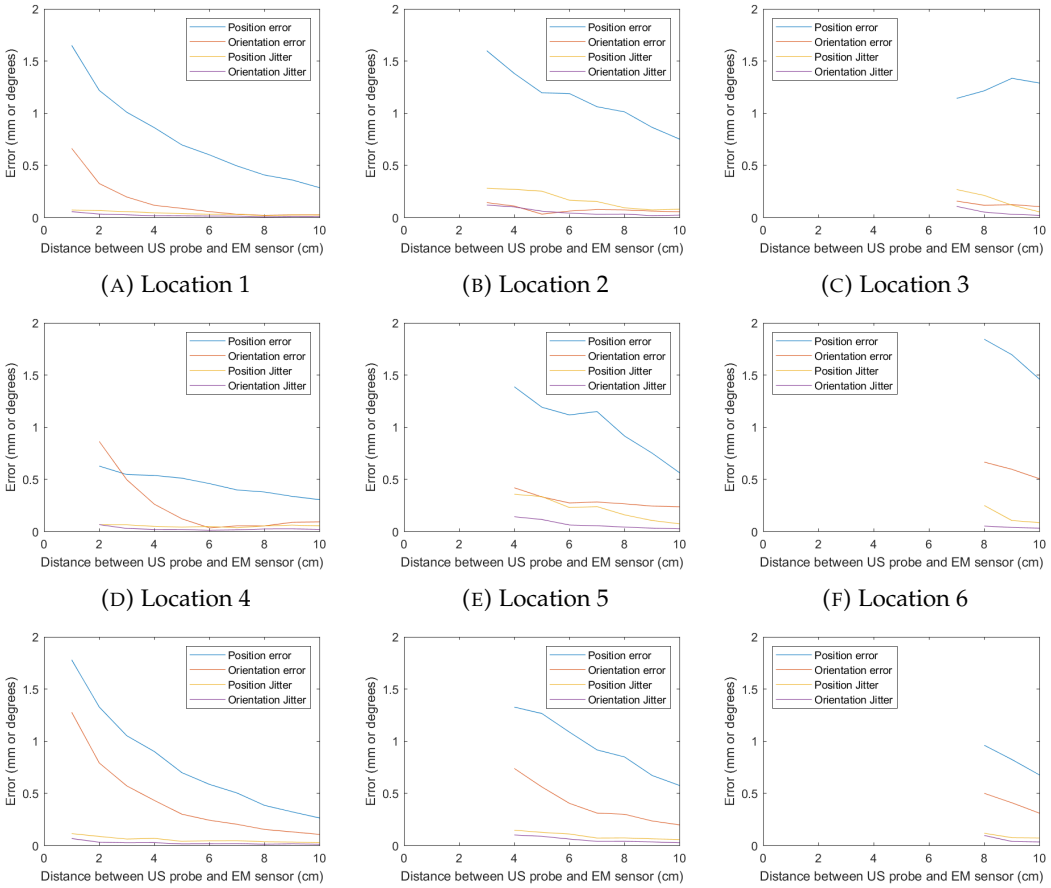

(A) Location 1 (B) Location 2 (C) Location 3

(D) Location 4 (E) Location 5 (F) Location 6

(G) Location 7 (H) Location 8 (I) Location 9

FIGURE 2.10: Measured position and orientation error and jitter at various distances between the US probe and the EM sensor. Each subfigure (A-I) represents one of nine measurement locations (Figure 2.5). At some distances no data is plotted, since the measurement rate of the EM sensor decreased due to the interference at these positions.

Trial 3: Dynamic measurements with wireless US probe

The measured mean position and orientation RMSE for the trajectories at 20 cm distance to the TTFG, at 40 cm distance to the TTFG and at clinical relevant positions have been listed in Table 2.2. For every trajectory, the RMSE values increase when the combined sensor is attached to the US probe compared to the reference. When locating the combined sensor at 4.5 cm distance to the US probe, both position and orientation RMSE are higher than at 6.5 cm distance. In this case, the orientation RMSE increases relatively more than the position RMSE.

When comparing between trajectories, the mean position and orientation RMSE is the lowest at 20 cm distance to the TTFG and highest at clinical relevant positions. When attaching the EM sensor to the US probe at 6.5 cm distance, compared to the reference, an average position and orientation RMSE increase of 0.4 mm and 0.5-0.7 degrees can be seen.

TABLE 2.2: Mean position and orientation RMSE on three trajectories for the combined sensor only (reference), the sensor attached to the US probe at 6.5 cm distance and attached at 4.5 cm distance.

	Trajectory at 20 cm		Trajectory at 40 cm		Clinical relevant trajectory	
	Position RMSE (mm)	Orientation RMSE (degrees)	Position RMSE (mm)	Orientation RMSE (degrees)	Position RMSE (mm)	Orientation RMSE (degrees)
Reference	0.9 ± 0.0	0.5 ± 0.0	1.7 ± 0.0	0.6 ± 0.0	2.0 ± 0.1	1.0 ± 0.1
US probe at 6.5 cm	1.3 ± 0.1	1.2 ± 0.0	2.1 ± 0.0	1.3 ± 0.0	2.4 ± 0.0	1.5 ± 0.0
US probe at 4.5 cm	1.4 ± 0.0	1.9 ± 0.0	2.3 ± 0.0	2.0 ± 0.0	2.9 ± 0.0	2.2 ± 0.0

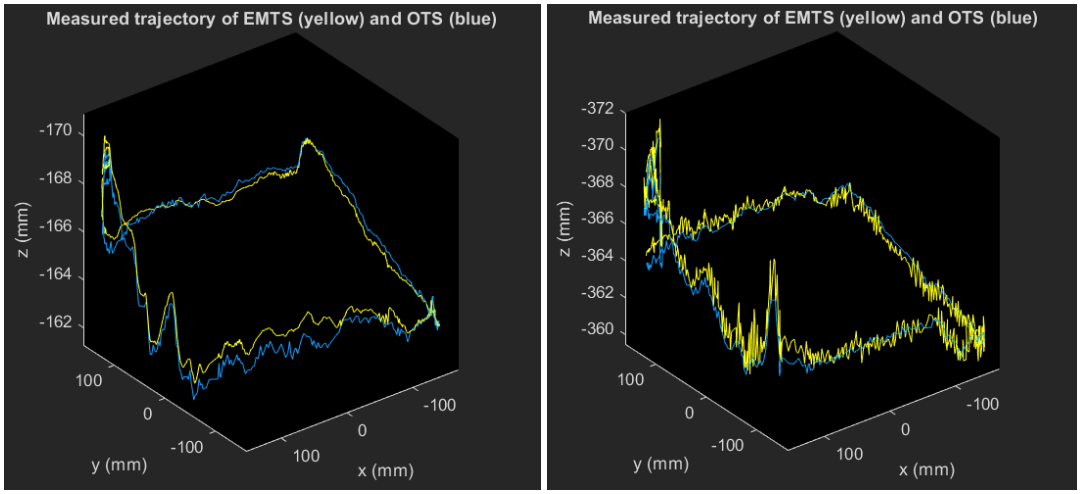

FIGURE 2.11: The trajectories of the reference measurements at 20 cm distance to the TTFG (left) and at 40 cm distance (right). The trajectory measured by the EMTS is visualized in yellow and the one measured by the OTS in blue.

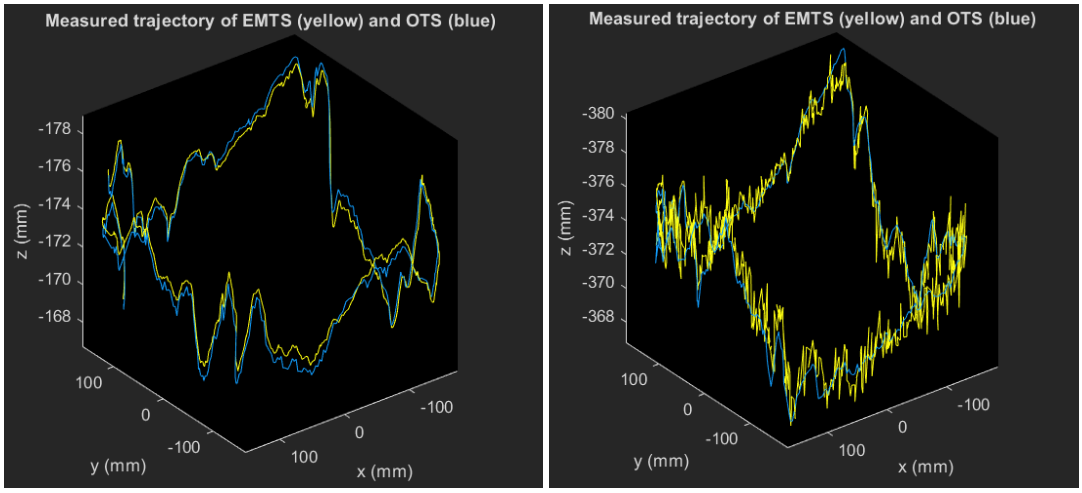

FIGURE 2.12: The trajectories of the measurements with the combined sensor attached at 6.5 cm to the US probe at 20 cm distance to the TTFG (left) and at 40 cm distance (right). The trajectory measured by the EMTS is visualized in yellow and the one measured by the OTS in blue.

The trajectories of the reference measurements at 20 cm and 40 cm distance to the TTFG are visualized in Figure 2.11. The same trajectories for the combined sensor attached to the US probe at 6.5 cm distance are shown in Figure 2.12. Both figures show an increase of the EM jitter at 40 cm distance to the TTFG compared to 20 cm distance. Visually, the jitter at 40 cm distance when using the US probe (Figure 2.12) is higher than the reference (Figure 2.11). However, all EM trajectories appear to follow the corresponding optical trajectory, without noticeable differences between both figures.

2.4 Discussion

In this study, a hybrid magneto-optical tracking setup was developed to examine the influence of different US probes on the EM tracking accuracy. In addition, nine EM sensor fixation positions on the wireless Clarius US probe were evaluated at various distances between 1 and 10 cm, which provided insight to select a location where the EM tracking interference caused by the US probe is minimal. Eventually, a 3D printed clip was manufactured, which could rigidly attach an EM sensor to the Clarius US probe at 6.5 cm near the scanning side while maintaining high EM tracking accuracy. This is the first step towards a tracked US system that has the potential to be clinically implemented for patient registration prior to abdominal tumor navigation.

Testing the interference of two different BK US probes (curved array and T-shape) and the wireless Clarius US probe with the Aurora EMTS showed that only the Clarius US device has a very strong influence on both position and orientation error and jitter. This interference might be caused by ferromagnetic parts located inside the Clarius US probe, since this probe is much more advanced compared to the conventional BK transducers. Eddy currents could be induced in these ferromagnetic parts, which distorts the EM tracking field. Moreover, the position and orientation errors amplified when the wireless US device was activated. This would suggest that electronics within the US probe, such as the battery, induce Eddy currents as well. The Wi-Fi or bluetooth signal of the Clarius US probe might cause additional interference, but this was not confirmed during this study.

Compared to the study of Hastenteufel *et al.*, the maximum position error caused by three 3D US probes (9.8, 10.9 and 31.6 mm) is higher than for the wireless Clarius US probe evaluated in this study (5.8 mm) [45]. However, the influence of the distance between the EM sensor and the US probe on the tracking error was not evaluated for the 3D US probes. On the other hand, they stated that the interference caused by 3D US probes is not systematic, especially when moving or rotating the US probe throughout the EM field [45]. This finding is similar to the Clarius US probe in this study, which might be a potential downside in clinical application when moving and rotation of the US device is required.

The results of the static position measurements clearly showed that the EM tracking error was higher when locating the EM sensor closer to the battery of the Clarius US probe. Furthermore, the measurement rate decreased closer to the battery and the distance between the EM sensor and targets in the US image would be larger. Therefore, the EM sensor should be located close to the scanning side of the US probe for minimal EM tracking interference. The location of the EM sensor at the front or side of the US probe showed acceptable tracking errors for a probe-sensor distance of 6 cm or more (0.6 mm and 0.1 degrees). Practically, a clip with attached sensor on the front would hinder the US scanning procedure less than on the side

of the US probe. Therefore, an EM sensor fixation position was chosen at 6.5 cm distance to the wireless Clarius US probe at the front of the probe.

A limitation of the static measurements is that the EM sensor was positioned in the middle of the EM tracking field only, since the EM tracking accuracy is optimal at that location and the EM sensor could not be moved during measurements. The tracking accuracy could have been different near the edges of the EM field or at an increased distance to the TTFG. Changing the orientation of the US probe with respect to the EM sensor might influence the amount of EM tracking distortion as well. Therefore, the results of the static measurements cannot be generalized for the entire tracking field and the clinical application.

Therefore, dynamic measurements were done to evaluate the EM tracking accuracy throughout the EM field and at clinically relevant areas. The results show a sub-millimeter and sub-degree increase of the mean position and orientation RMSE when fixating the EM sensor at 6.5 cm distance to the wireless US probe compared to the reference. According to Figure 2.11 and 2.12, the EM tracking error is mainly caused by the increased jitter of the EM sensor. The jitter could be reduced by averaging measured transformations or by applying a specific filter or smoother, such as a Kalman filter or Rauch–Tung–Striebel smoother. Otherwise, the planar FG could be applied instead of the TTFG to reduce the distance between the EM sensor and the FG, which might reduce the jitter.

For the clinical application of the tracked US probe in patient registration prior to surgical navigation, an accuracy in the sub-millimeter and sub-degree range is desirable, which was achieved in this study. However, a small orientation error might have a large impact on the position error in US images, due to the leverage. For example, the distance between the EM sensor and targets in the US image is approximately 12 cm at an US image depth of 10 cm and using the selected EM sensor position of 6.5 cm. The positional displacement due to the orientation error is defined as the product of the orientation error in radians and the distance to the target in mm. At the measured orientation error of 0.1 degrees and a distance of 120 mm, the positional displacement is approximately 0.2 mm. Therefore, the measured EM tracking error on the selected fixation position seems acceptable for this application. However, the wireless US probe will remain to interfere with the EMTS to some extent and fluctuates depending on the position in the EM tracking field. Therefore, conventional wired US probes that cause minimal interference, such as the T-shaped BK transducer, are recommended for more precise applications.

Since the Clarius US device will always interfere with the Aurora EMTS to some extent, it would be wise to investigate alternatives uses for this US device. For instance, the Clarius US device could be tracked by an OTS instead of the EMTS, since an OTS does not suffer from interference. However, it could be challenging to achieve a direct line of sight between the optical camera and the sensor on the US device during surgery. Another alternative is to further investigate the possibilities with the embedded IMU, which could serve as an addition to the EM tracking information to improve the accuracy. Otherwise, a deep learning algorithm in combination with the IMU might be able to track the US device as well [59]. However, a major disadvantage of using solely IMU data is the drift that occurs when measuring long trajectories.

The calibration procedure of the magneto-optical tracking system resulted in a sub-millimeter and sub-degree accuracy (mean RMSE of 0.7 mm and 0.5 degrees). However, the range of the calibrated position and orientation error throughout the EM field was relatively high, namely 0.1-1.7 mm and 0.1-1.3 degrees. This means that tracking errors during measurements could be caused by the uncertainty of

the calibration instead of interference with the US probe. This calibration uncertainty depends on a combination of factors: the calibrated static transformations ${}^{OPTsens}T_{EMsens}$ and ${}^{EMTS}T_{OPT_{FG}}$, the accuracy of the EMTS (0.5 mm RMSE), the accuracy of the OTS (0.3 mm RMSE) and the accuracy of both calibrated optical objects ($\pm$ 0.2 mm RMSE). In addition, jitter causes extra distortion during dynamic measurements. Furthermore, literature showed that EM tracking accuracy decreases at a larger distance to the TTFG and near edges of the EM field of view [40]. This suggests that calibration improvements could mainly be made by decreasing the calibration error range or by focusing on a specific target area within the EM field.

Future perspectives

When new materials or devices need to be integrated with the EMTS at the NKI-AvL in the future, the created hybrid magneto-optical tracking system could be very useful. This setup provides insight if and how much interference would be caused by these new materials or devices. The main advantage of this setup is that it could validate the EM tracking accuracy in a dynamic setting throughout the entire EM field. Furthermore, the setup can be easily rebuilt and the calibrated transformations from this study are available for future application. However, it is advised to repeat the optimization process with the Levenberg-Marquardt algorithm after rebuilding the magneto-optical tracking setup, to reach an optimal calibration accuracy.

Since the EM sensor can now be rigidly attached to the wireless US probe while maintaining accurate EM tracking, the next step is to calibrate the US probe with the EMTS. This would result in a tracked US system, which could transform positions from the US image to the EMTS. Eventually, this tracked US system provides the foundation for patient registration prior to surgical navigation. Therefore, clinical feasibility of the tracked US system will be evaluated after the calibration procedure.

2.5 Conclusion

In this study, a hybrid magneto-optical tracking setup was developed to measure the influence of a wireless US device on the EM tracking accuracy. A suitable fixation position for the EM sensor on the wireless US probe with a sub-millimeter and sub-degree EM tracking accuracy was found, which provides the foundation towards clinical implementation of the tracked wireless US device. Future research should focus on the calibration of the US device with the EMTS and on the clinical feasibility of using tracked ultrasound for patient registration prior to surgical navigation.

Chapter 3

Calibration of tracked ultrasound device

3.1 Introduction

During clinical patient registration with tracked US, specific anatomical targets on the US images will be matched to correlating targets on the pre-operative CT-scan. For this, the 3D position of targets on the US image needs to be known in EM tracking coordinates. Technically, the attachment of an EM sensor to the US probe enables real-time tracking of the location and orientation of the US probe. However, the relation between the US image and the attached EM sensor is initially unknown. Therefore, a calibration process of the US device with the EMTS is needed before clinical application would be feasible.

The calibration process of an US device with EMTS consists of two parts, temporal and spatial calibration. Temporal calibration corrects for the time offset between data acquired by the US probe and the EMTS to synchronize both data streams. Spatial calibration matches the location and orientation between both systems by finding the static transformation between the US image and the EM sensor attached to the US probe (${}^{EMsens}T_{USim}$). According to literature, spatial calibration is the main source of error for the surgical navigation accuracy [60]. Therefore, an accurate calibration method is essential for optimal US tracking and clinical feasibility.

A common method for temporal calibration is to move the US probe with attached EM sensor up and down in a tank filled with water, while imaging the bottom of the tank with US. Measuring the vertical position change of the EM sensor and the bottom of the tank in the US image results in two sinus-shaped curves. When matching these curves, the time lag between both systems could be calculated and a correction for the offset could be made [60].

Spatial calibration of a tracked US device has been widely researched in literature and several solutions have been proposed [28]. Most solutions apply a tracked phantom with known geometry to match specific phantom features detected in scanned US images with the known geometry of the phantom. The main difference between each method is the applied phantom type and geometry, such as a point target, single cross-wire phantom, N-wire phantom or a tracked pointer [28]. Each phantom type has it pros and cons in calibration accuracy, difficulty and speed, but no optimal standardized method has been found yet.

Single point methods, such as the point target or single cross-wire phantom, apply a bead, pin head or the crossing of two intersecting wires as calibration point. This target, of which the real-time location is known because of the calibrated phantom, is scanned with the US device at different depths and angles. Afterwards, the target could be selected on the US images and matched with the phantom using an ICP algorithm. An advantage of this method is that the calibration method

and phantom design is relatively easy. However, manual segmentation of the target point is needed, which requires some user experience and is time consuming. More importantly, it is hard to align the target point precisely at the center of the US image plane since the thickness of the US plane could be several millimeters. In addition, the phantom itself needs to be manufactured and calibrated, which is a factor for calibration errors as well [28], [61].

Another variant of a single point calibration method is by using a tracked pointer. This method is similar to the previously mentioned single point calibration methods, namely acquiring US images of the tip of the pointer and applying an ICP algorithm. The main advantage of the tracked pointer is that no phantom is required, which reduces the number of possible error causes. However, manual alignment of the pointer in the center of the US plane remains a challenge [62], [63].

Other spatial calibration methods use so called wall phantoms, such as a 2D alignment phantom or a phantom with one or more planes. Wall phantoms produce a line on the US image, which is easier to identify than a single point [28]. Many different phantom types have been developed, of which the Cambridge phantom achieved the highest calibration accuracy [61], [64]. However, this phantom is patented and one of the most difficult phantoms to apply.

Finally, phantoms with multiple wires have been evaluated, such as the N-wire phantom [65]. The N-wire phantom consists of one or more N-shaped wires, which form a specific pattern that could be scanned by the US device. Since automatic segmentation of these wires on the US image is feasible, this calibration method is easy to use and only takes a few seconds. However, accurate manufacturing and calibration of the N-wire phantom is required to achieve good results. This method is the fastest and easiest to use, but the accuracy could be poor at increased depths on the US image [61].

When comparing the accuracy and reproducibility of the various methods, the Cambridge phantom achieves the highest mean accuracy [61]. However, the reproducibility of this phantom is poor due to the required user experience and phantom manufacturing could be difficult. Two easier to use spatial calibration methods apply either the tracked pointer or the N-wire phantom. Using the tracked pointer results in a slightly greater variance than the N-wire phantom, probably due to the manual alignment of the pointer in the US image plane. However, the calibration accuracy of the tracked pointer was significantly better compared to the N-wire phantom [66]. Therefore, when using a proper measurement setup, the tracked pointer method should provide a good spatial calibration for tracked US devices.

In addition, data collection for calibration could be performed freehand or with a (robotic) gripper [67]. The main advantage of freehand calibration is that it could be performed relatively quick. However, some US scanning experience and a steady hand are required to correctly image the phantom and manual errors could occur, resulting in an inaccurate calibration. When using a (robotic) gripper to fixate the US probe and phantom, tracking sensors remain steady and tracking data is collected more accurate. However, building such measurement setup is expensive, complex and gripper or robotic parts could interfere with the EMTS. Therefore, no robotic gripper was used in this study.

In this chapter, the Clarius US probe will be calibrated with the Aurora EMTS through temporal and spatial calibration. The tracked pointer method will be applied for spatial calibration, since the measurement setup is relatively easy to build, no additional phantom needs to be manufactured and a relatively high calibration accuracy could be achieved [66]. The tracked pointer will be fixed in the measurement setup, to improve stability and visualization of the pointer tip precisely in the

center of the US image plane. In addition, the calibration process is repeated using the BK T-shaped US device. Afterwards, the accuracy of the calibration will be evaluated with the leave-one-out cross-validation (LOOCV) method and a comparison between both US devices could be made.

3.2 Materials and methods

3.2.1 Hardware

The calibration measurements were performed with the Clarius US probe (C3 HD, Clarius Mobile Health Corporation, Burnaby, Canada) and the NDI Aurora EMTS. This EMTS consisted of a TTFG with SIU, SCU, an Aurora pointer (Figure 1.9b) and an EM cable tool sensor (Figure 1.9d). The EM cable tool sensor was glued onto a 3D printed clip, which rigidly attaches the EM sensor to the wireless US probe at a location with minimal EM tracking interference according to Chapter 2 (Figure 3.1). Since the clip fits onto the US probe in one specific manner only, it is not required to repeat the calibration when reattaching the clip to the US device. The calibration measurements were repeated using the BK T-shaped US device (I14C5T, BK Medical, Peabody, USA), attached clip with EM sensor (Figure 1.12) and the same EMTS. Since one tracking sensor broke during the patient study, two different clips (old clip and new clip) have been calibrated.

FIGURE 3.1: Wireless Clarius US probe with attached clip with EM sensor.

The measurement setup for the calibration of the tracked ultrasound device is visualized in Figure 3.2. In this setup, the EM pointer was fixed to a with water filled tank with the pointer tip located inside the water. The TTFG was located underneath and the water tank was positioned in the center of the EM tracking field to ensure optimal tracking accuracy of the EM pointer and EM sensor.

The SOS assumed by the Clarius and BK US devices is 1,538.5 m/s [68]. For optimal calibration, the SOS of the water inside the tank should match the SOS assumed

by the US device, which depends on the used medium and its temperature. Initially, the tank was filled with 16 L distilled water at room temperature (19 °C). An ethanol/water mixture of 9.5% results in an SOS of approximately 1,538.5 m/s at 19 °C, according to Martin *et al.* [69]. Therefore, 16 L distilled water was mixed with 1.68 L ethanol to reach the desired SOS. During the measurements, the temperature of the ethanol/water mixture was measured.

FIGURE 3.2: Measurement setup for the calibration of the wireless US device with the EMTS.

3.2.2 Software

The NDI toolbox software was used for initial evaluation of the measurement setup and EM tracking volume. The EMTS was connected to a computer (Intel Xeon E-2144G CPU @ 3.60 GHz; 16.0 GB RAM; 64-bit operating system) through a USB 3.1 connection. The Clarius US device was connected to a router (ASUS RT-AC66U B1) using the Clarius Ultrasound App version 7.1.0 on a mobile phone. Then, the computer was connected to the same router through a wired Ethernet connection. For the purpose of this study, a new version of PlusServer from the PLUS toolkit was build using CMake 3.18.4, Microsoft Visual Studio 2015 and Qt 5.12.2, which was required to enable real-time data stream from the Clarius US device [48]. The Clarius Listen API version 7.1.0 was implemented in the build process [70]. The built PlusServer could receive tracking data from the EMTS and US images with pixel spacing information from the Clarius US device. The received data was send by PlusServer through OpenIGTLink and read into 3D Slicer version 4.10.2 with the SlicerIGT extension [49], [50]. Within 3D Slicer, the spatial calibration of the tracked US device and all further data evaluation was done.

3.2.3 Temporal calibration

Temporal calibration was performed using fCal software, which comes with the PLUS toolkit. The US probe with attached EM sensor was moved vertically up and down at an approximately constant speed inside the water tank, while imaging the bottom of the tank with US and measuring the position of the EM sensor. The software automatically detected and segmented the bottom of the water tank and calculated the time offset between the US images and the EM tracking data. This process was repeated three times and the resulting time offsets were averaged. However, a time offset of several milliseconds between the US device and EMTS was found for both BK and Clarius. This time offset could be neglected and no temporal correction was made between the EMTS and each US device.

3.2.4 Spatial calibration

The purpose of spatial calibration was to find the static transformation between the US image and the EM sensor attached to the US probe (${}^{EMsens}T_{USim}$ from Figure 1.13). Since US image coordinates are initially defined as pixel coordinates and a correction for each zoom factor of the US device needs to be made, ${}^{EMsens}T_{USim}$ was separated into three parts:

$$ {}^{EMsens}T_{USim} = {}^{EMsens}T_{USprobe}\,{}^{USprobe}T_{USim\_mm}\,{}^{USim\_mm}S_{USim} \tag{3.1} $$

First, a scaling transformation was defined for the transformation of US image points from pixel coordinates to millimeters (${}^{USim\_mm}S_{USim}$). This transformation scales the US image in x- and y-direction with a scaling factor defined by the pixel spacing, which is the distance between two adjacent pixels in mm. The pixel spacing is uniform for the x- and y-direction, changes for every zoom factor and can be read out into 3D Slicer in real-time. Therefore, ${}^{USim\_mm}S_{USim}$ is a static scaling, but it changes when the zoom factor is altered. The origin of US_{im_mm} has been visualized in green in Figure 3.3, which has the same origin as US_{im} since only scaling is applied.

A second transformation matrix was defined, which translates points from the US image coordinate system in millimeters to the US probe coordinate system (${}^{USprobe}T_{USim\_mm}$). The origin of the US probe coordinate system was defined as the center of the probe's scanning side on the US image, visualized in blue in Figure 3.3. This position always remains the same, while the origin of US_{im} changes for each zoom factor. Since the number of pixels in the image is uniform regardless of the zoom factor, the image size information was combined with the pixel spacing to compute a translation in x- and y-direction. Afterwards, a rotation of 180 degrees around the x-axis was combined with the computed translation to form the transformation matrix ${}^{USprobe}T_{USim\_mm}$ (Figure 3.3). Similar to ${}^{USim\_mm}S_{USim}$, ${}^{USprobe}T_{USim\_mm}$ is a static transformation that only changes when altering the zoom factor.

The third and final transformation translates points from the US probe coordinate system to the coordinate system of the EM sensor attached to the US probe (${}^{EMsens}T_{USprobe}$)(Figure 3.3). This is a static transformation independent on the zoom factor, which will be computed with the spatial calibration method using a tracked pointer.

During the spatial calibration measurements, the tip of the EM pointer was scanned with the US device, while holding it inside the water tank (Figure 3.2). Fixation of the EM pointer made it easier to accurately visualize the pointer tip in the US image by slightly moving and tilting the US probe only. During these measurements,

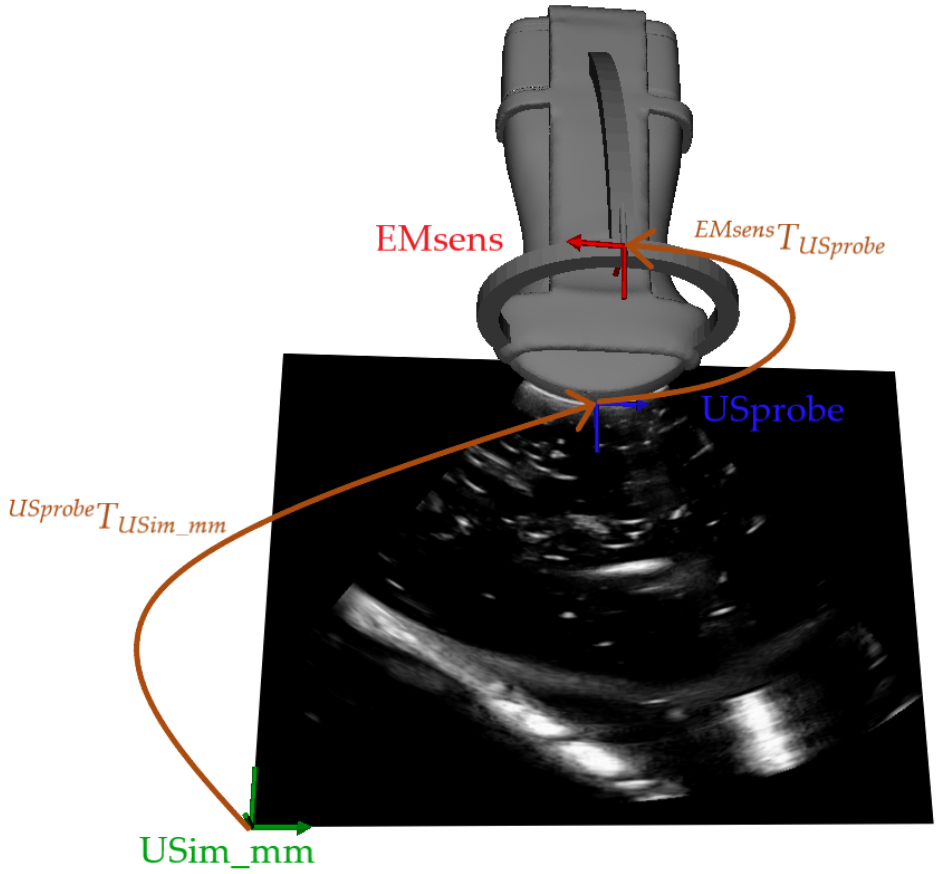

FIGURE 3.3: Overview of the wireless US device (grey), US image (black), coordinate systems (green, blue and red) and transformations (brown) for the application of a tracked US device.

the pointer tip was pointed towards the scanning part of the US device and located at 29 different locations relative to the US image. These locations were spread across the field of view of the US image and three zoom factors have been applied, namely a depth of 5, 15 and 30 cm. At each location, the US probe was tilted until an artifact with the highest intensity arose at the pointer tip on the US image. This indicated that the pointer tip was located exactly in the 2D US image plane [62], which is important for an accurate calibration. In Figure 3.4, the difference in intensity of the artifact is visualized. The left image has practically no artifact, which means that the pointer is not located inside the US plane. On the right image, the pointer tip is placed too far through the US plane, causing an artifact just below the pointer tip. In the middle image, the artifact has the highest intensity and the pointer tip location has been indicated by a red dot.

During the measurements, the US images were recorded with the corresponding tracking information, consisting of the transformation from the EM sensor to the EMTS (${}^{EMTS}T_{EMsens}$) and the transformation from the EM pointer to the EMTS (${}^{EMTS}T_{EMpointer}$). The recorded measurement data was used to compute the transformation ${}^{EMsens}T_{USprobe}$. For every EM pointer location, two corresponding points were selected, resulting in two sets of 29 points each. The first set of points were manually selected on the US image, exactly at the pointer tip (red dot in Figure 3.4). Since a correction for the zoom factor was already achieved, these points were defined in the US_{probe} coordinate system (Equation 3.2). The second set of points were

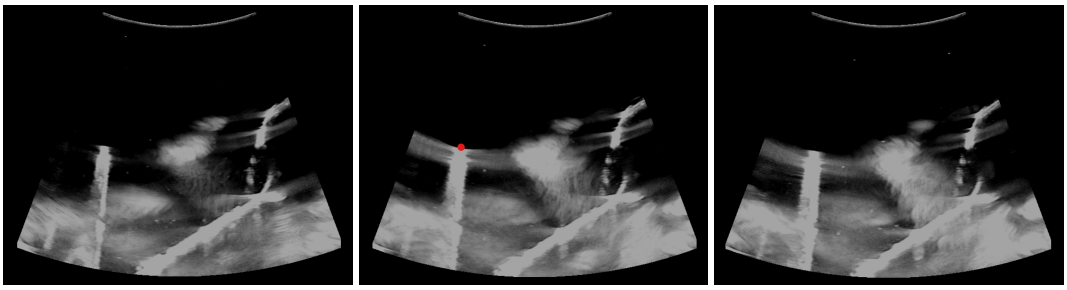

FIGURE 3.4: Three US images of an EM pointer at the left side on each image. The pointer tip is located in front of the US plane (left), exactly in the US plane (middle) and beyond the US plane (right). A red dot indicates the correct pointer tip location.

computed using the tracking data from the EMTS. Here, the measured location of the EM pointer was defined in the EM_{sens} coordinate system with Equation 3.3. Afterwards, an ICP registration algorithm was applied on the data using the "fiducial registration wizard" module within 3D Slicer, which resulted in the calibrated transformation ${}^{EMsens}T_{USprobe}$. The RMSE of the ICP registration was computed automatically in 3D Slicer.

$$ {}^{USprobe}p = {}^{USprobe}T_{USim\_mm} \; {}^{USim\_mm}S_{USim} \; {}^{USim}p \tag{3.2} $$

$$ {}^{EMsens}p = {}^{EMTS}T_{EMsens}{}^{-1} \; {}^{EMTS}T_{EMpointer} \; {}^{EMpointer}p \tag{3.3} $$

The same spatial calibration method was repeated twice for the BK ultrasound device. First, the old clip was attached to the probe and, secondly, the new clip. Approximately the same number of pointer tip locations were selected for each calibration and three zoom factors were applied, namely a depth of 5, 9 and 13 cm.

3.2.5 Accuracy evaluation

Based on the acquired spatial calibration measurement data, the RMSE of the ICP calibration and the leave-one-out cross-validation error (LOOCVE) were computed. As previously described, the calibration of ${}^{EMsens}T_{USprobe}$ was based on $N = 29$ measured point locations on the US image (${}^{USprobe}p$) and measured by the EMTS (${}^{EMsens}p$). To calculate the LOOCVE, one of the measured points ($i = 1, ..., N$) was removed from both sets and a new transformation was computed using the remaining 28 points. This new transformation was then applied to transform the removed point ${}^{USprobe}p(i)$ from the US_{probe} coordinate system to the EM_{sens} coordinate system, resulting in ${}^{EMsens\_T}p(i)$. Afterwards, the euclidean distance between the transformed point (${}^{EMsens\_T}p(i)$) and the originally measured point by the EMTS (${}^{EMsens}p(i)$) was computed. This process was repeated for all 29 points and the LOOCVE was defined as the average of the euclidean distances, with the following equation: [30]

$$ LOOCVE = \frac{1}{N}\sum_{i=1}^{N} || {}^{EMsens}p(i) - {}^{EMsens\_T}p(i) || \tag{3.4} $$

In addition, the mean absolute error (MAE) of the calibration was computed in x-, y- and z-direction to evaluate the offset in each direction of the US image.

The MAE was defined as the mean of the absolute difference of the x-, y- and z-coordinate between ${}^{USprobe}p$ and ${}^{EMsens}p$ transformed to the US_{probe} coordinate system with ${}^{EMsens}T_{USprobe}{}^{-1}$.

Finally, an independent samples t test was used to analyze the mean differences between two unpaired groups: either Clarius, BK old clip or BK new clip. Values of $P<0.05$ were considered to be statistically significant.

3.3 Results

3.3.1 Spatial calibration accuracy

A visual representation of the calibration accuracy is shown in Figure 3.5. Here, the inverse calibrated transformation ${}^{EMsens}T_{USprobe}{}^{-1}$ was applied on ${}^{EMsens}p$ (red points), which then could be compared with ${}^{USprobe}p$ (blue points) relative to the US image plane. When looking at the xy-plane (A,C,E), the blue and red points are located at approximately the same position, which indicates a successful calibration. However, the distance between the blue and red points seem to increase at the edges of the US image, for example at the lowest and highest depth. The error between points is smaller at the center of the US image, which is at a depth of approximately 6.5 and 15 cm for BK and Clarius, respectively. On the zy-plane (B,D,F), the blue points are located exactly at one line, since they were selected on the 2D US image. After a perfect calibration, the red points should be located on the same line. In this figure, the red points are aligned, but some outliers could be spotted.

The RMSE, LOOCVE and MAE of the spatial calibration have been listed in Table 3.1. The LOOCVE has a similar value compared to the RMSE for each calibrated clip and US device. When comparing the Clarius with the BK US device, the listed error values are approximately twice as high for the Clarius US device, which is a statistically significant difference compared to both BK clips (P=0.000). This difference is visible in Figure 3.5 as well, since an increased distance between points could be seen for the Clarius calibration compared to both BK calibrations. Furthermore, the BK calibration with the old clip has a slightly higher LOOCVE compared to the BK calibration with the new clip. However, this difference was not statistically significant (P=0.429).

When comparing the MAE in each direction for the calibration with the Clarius US device, the error is larger in the x- and y-direction (1.5 and 1.7 mm) than in the z-direction (1.1 mm). This suggests that the depth error of the calibration is larger than the out of plane error. For the BK, the MAE is similar in each direction.

TABLE 3.1: RMSE, LOOCVE and MAE in x-, y- and z-direction of the spatial calibration for the Clarius US, BK US with the old clip and BK US with the new clip.

	RMSE (mm)	LOOCVE $\pm$ SD (mm)	MAE (mm)		
			x-axis	y-axis	z-axis
Clarius	3.1	3.1 ± 1.3	1.5	1.7	1.1
BK old clip	1.7	1.7 ± 0.9	0.6	0.8	0.9
BK new clip	1.5	1.5 ± 0.6	0.8	0.7	0.7

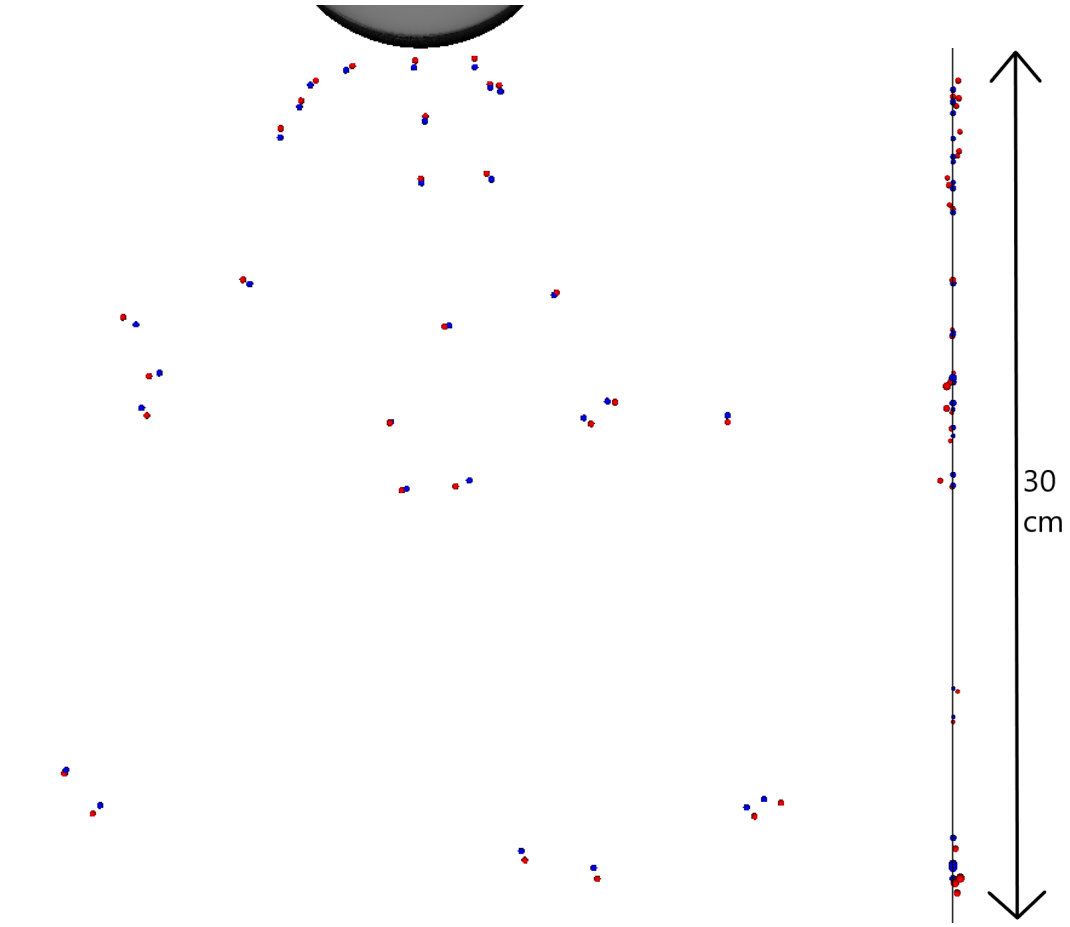

(A) Clarius xy-plane

(B) Clarius zy-plane

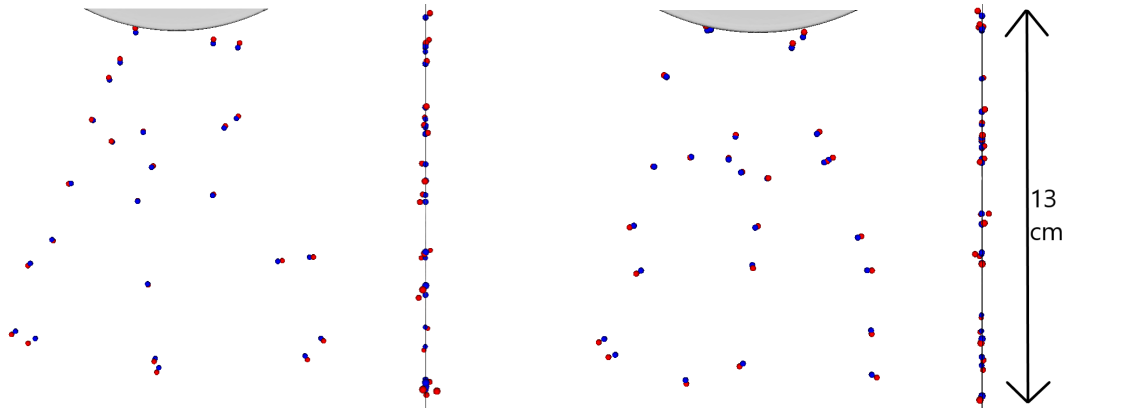

(C) BK old clip xy-plane

(D) BK old clip zy-plane

(E) BK new clip xy-plane

(F) BK new clip zy-plane

FIGURE 3.5: Visual representation of the calibration accuracy for the Clarius (A,B) and BK US device with old (C,D) and new clip (E,F). The points have a diameter of 2 mm and represent the pointer tip locations in US_{probe} coordinates (blue) and EM_{sens} coordinates transformed to the US_{probe} coordinate system (red). The depth is 30 cm for Clarius (A,B) and 13 cm for BK (C-F).

3.4 Discussion

In this study, the Clarius and BK US devices have been calibrated with the Aurora EMTS by applying the tracked pointer calibration method. According to the LOOCV method, a calibration accuracy of 3.1 mm was achieved for the Clarius US device, while the BK US device reached a calibration accuracy of 1.5 and 1.7 mm, which is a statistically significant difference of approximately 1.5 mm. A possible reason for this difference in calibration accuracy is the maximum depth used by both US devices, which is 13 cm for the BK and 30 cm for the Clarius device. Application of an ICP algorithm on a set of points that are located further apart would inherently result in a larger error. Furthermore, accurate visualization of the tracked pointer on US images is more difficult at increased depths due to a decreased intensity of the pointer tip and the artifact. Besides that, the Clarius US device uses a lower frequency than the BK, leading to a decreased image resolution. This makes manual selection of pointer tip locations on the US image more difficult when using Clarius compared to BK, which could have negatively influenced the calibration accuracy.

Another important factor that might have reduced the calibration accuracy of the Clarius US probe is interference of the probe with the EMTS. As evaluated in Chapter 2, a static tracking error of approximately 0.6 mm and 0.1 degrees was found with the same clip used in this study. This error might have increased during the spatial calibration measurement due to jitter, since the pointer tip locations were chosen at one specific EM measurement position. Application of an averaging method to filter the jitter might improve the calibration accuracy. On the other hand, the calibration measurements were performed at the center of the EM tracking field, where the EM jitter was minimal. Due to an availability issue, the cable tool sensor was attached to the clip instead of the reference disk sensor that was used for the measurements in Chapter 2. The cable tool sensor is slightly less accurate than the reference disk sensor, which might have caused additional tracking inaccuracies [40].

The spatial calibration method with a tracked pointer was relatively easy to apply and, after some practice, visualization of the pointer tip on the US image was feasible. However, limitations of this method are the manual selection of pointer tip locations on the US images and the uncertainty of SOS in the water during measurements. The error caused by the selection of pointer tip locations highly depends on a precise positioning of the pointer tip in the US image plane. According to the MAE in the z direction, this error was approximately 1 mm for each calibration, which is acceptable. However, some mismatch in x- and y-direction is visible in Figure 3.5 as well, mainly at the edges of the US image. Visually, the selected (blue) points seem incorrectly scaled, which might be caused by an SOS difference between the water and the system's assumed SOS. During the measurements, the temperature of the ethanol/water mixture did increase to 21 °C, which might have caused a small SOS increase in the medium of approximately 4 m/s [69]. According to Equation 1.5, this could cause a shift of at most 1 mm in the y-direction, depending on the depth. This would imply that the accuracy of this calibration is most accurate at the center of the US image, which is at 6.5 and 15 cm depth for BK and Clarius. Therefore, calibration improvements could be made by focusing more on the clinical relevant depths, which is at approximately 0-8 cm.

The RMSE stated in the results show the accuracy of the computed calibration, but this parameter is not necessarily the same as the tracking accuracy of the US device. For example, when reducing the number of points used to calculate the calibration, the RMSE will likely decrease. However, the tracking accuracy could be worse because of a too specific calibration on one part of the US image due to

a low number of points. Therefore, using an increased number of points spread throughout the US image for the calibration could lead to an improved tracking accuracy, while the RMSE increases. According to Figure 3.5, the spread of points used for the BK calibration is good. For the Clarius US device, more points could have been selected between the middle and lower part of the US image.

The LOOCVE provides a better indication of the tracking accuracy of the calibrated US device than the RMSE, since it uses target points that were not applied for the calculation of the calibration. However, a limiting factor of this method is that the validation target points were determined in the same manner and with the same setup as the target points used for the calibration itself. Likewise, it is uncertain if the pointer tip locations are exactly correct, since they were manually selected. Therefore, systematic errors caused by the measurement setup or method would not be retrieved by this parameter. On the other hand, the LOOCVE shows the consistency of the collected data. The SDs in this study (1.3, 0.9 and 0.6 mm) are relatively high compared to the results of Bø *et al.* (0.07, 0.06 and 0.03 mm) [30]. This indicates that the accuracy of manually selecting pointer tip locations has a high variability between points.

Other studies that applied the same method with an EM tracked pointer reached similar calibration errors. For example, Zhang *et al.* found a calibration RMSE of 1.2 mm and Welch *et al.* reached an accuracy of 1.3 mm [63], [66]. Other studies reached a worse calibration accuracy, such as Hsu *et al.* with an accuracy of 3.2 mm [62]. This implies that the calibration with BK (1.5 and 1.7 mm) is acceptable, while the calibration with Clarius (3.1 mm) could be improved. However, it is difficult to compare spatial calibration results between different studies, since each method is slightly different and many other factors could influence the calibration error, such as the applied US device, depth setting, SOS of the water, position in the EM field and external distortion.

Future perspectives

After calibration of the US device, the main question remains if the same tracking accuracy could be achieved in clinical practice as well. One major difference between tracked US during calibration measurements and in vivo is the SOS of the medium. In human tissue, the SOS varies from approximately 1450 m/s in fat to 1600 m/s in muscles, while most US devices use a constant SOS of 1540 m/s [28]. These SOS differences could cause tracking errors in vivo varying from 0.5 to 3 mm [71]. When US scanning the pelvic bone, the US waves must propagate through the tissue between the skin and the pelvic bone, which mostly consists of fat. Theoretically, a SOS difference of approximately 90 m/s could occur, which is a shift of 3 mm if the target is located at a depth of 5 cm. Therefore, a correction for the SOS might be necessary to ensure accurate US tracking in clinical practice.

According to the results of this study, the tracked BK US device has a better tracking accuracy than the Clarius US device. A tracking accuracy of approximately 1.5 mm for the BK US device is acceptable for clinical application. However, a tracking accuracy of 3 mm for the Clarius US device is relatively high. Further research in a clinical setting is needed to investigate both devices and compare their pros and cons. Therefore, both devices will be applied in a patient study for the registration of the pelvic bone in Chapter 4, where a further comparison between both devices will be provided.

3.5 Conclusion

In this study, a Clarius and BK US device have been separately calibrated with the EMTS using the tracked pointer method, which resulted in a calibration accuracy of approximately 3 and 1.5 mm, respectively. Now, both tracked US devices could be applied in a clinical setting for patient registration prior to surgical navigation. The following step is to evaluate the accuracy of the US registration method by comparing it to the current reference standard.

Chapter 4

Feasibility of tracked ultrasound registration: a patient study

4.1 Introduction

At the NKI-AvL, surgical navigation has been proven to be of additional value in abdominal cancer surgery [15]–[18]. Visualization of a patient-specific 3D model from pre-operative imaging in combination with real-time EM tracking aids the surgeon in localizing tumors, malignant lymph nodes and other important anatomical structures, such as arteries, veins or ureters. This technique has the potential to improve patient outcomes by increasing the number of complete resections and reducing the complication rate.

For navigated surgeries, a registration procedure is required to correlate pre-operative imaging data with the patient's position on the OR. Currently, a CBCT-scan is made on the OR prior to the surgical procedure, which is rigidly registered with the pre-operative imaging data. The registration of the CBCT-scans with the EMTS is done using EM tracked patient sensors that are attached to the patient's skin near the surgical target area. An ICP algorithm registers the locations of the patient sensors on the CBCT-scan with the EM tracked positions in real-time, which is clinically feasible [17]. However, frequently, the patient is moved after the CBCT-scan has been acquired due to tilting of the surgical bed or transfer to another OR. Since the patient sensors are attached to the skin, these movements could cause a shift between the sensor positions and the anatomical target area, which could lead to navigation inaccuracies. For example, tilting of the surgical bed into Trendelenburg could cause the patient to move in cranial direction, while the patient sensors between the skin and the bed remain at approximately the same position. Currently, a manual translation of the CBCT registration is applied during surgery to correct for this error, which is not ideal and cannot correct for rotational differences [18]. Therefore, there is a high demand for an alternative registration method that could consistently reach an accurate navigation regardless of the patient position during surgery.

The use of tracked US instead of CBCT could overcome this problem, since US acquisition is possible on every OR regardless of the patient position or tilting of the surgical bed. A tracked US registration procedure could be performed after correctly positioning the patient, which might result in a more accurate registration than the current CBCT registration method. Furthermore, US registration targets, such as the pelvic bone, lie much closer to the surgical target area than the patient sensors on the skin for CBCT registration. Therefore, tracked US has the potential to consistently reach a high navigation accuracy, which could remove the need for a manual correction to improve surgical navigation usefulness and patient outcomes.

Some other advantages of US compared to CBCT is that US is a non-invasive method, removing the radiation exposure for the patient and staff members. Moreover, US causes minimal workflow interruption, since staff members are not obliged to leave the OR during acquisition, which is necessary during CBCT scanning. Furthermore, intra-operative re-registration with a sterile covered tracked US device might prove additional value, while re-registration with a CBCT is clinically not feasible. However, a major disadvantage of US is that the images are noisy, artifacts are common and the image quality is highly operator dependent. It could be challenging to accurately and consistently visualize anatomical targets with US. Therefore, the clinical feasibility of applying tracked US for patient registration prior to surgical navigation needs to be evaluated.

In this patient study, both EM tracked US devices (BK and Clarius) will be applied on patients undergoing abdominal cancer surgery with surgical navigation. Tracked US images of the pelvic bone will be collected and matched with the pre-operative CT-scan to determine the patient registration. The accuracy of this registration method will be evaluated by comparing it to the current reference, which is CBCT registration. In addition, the influence of the patient position on the resulting registration will be evaluated by acquiring two separate US scans for each patient: one in Trendelenburg and one in horizontal patient position.

4.2 Materials and methods

4.2.1 Hardware and software

For each measurement the NDI Aurora EMTS with SIU, SCU and TTFG was applied. Four EM sensors were tracked, namely three Philips patient sensors (Figure 1.9a) and one EM sensor attached to the US probe. Either the calibrated BK T-shaped US device (Figure 1.12) or the calibrated Clarius US probe (Figure 3.1) was used, since the Clarius US probe was not yet calibrated at the start of this study. For the BK, two similar clips have been applied (old clip and new clip), since one sensor broke during the period of the patient study. The used CBCT was a Philips Allura FD20 XperCT.

Several software packages have been used. During patient measurements, PlusServer from the PLUS toolkit was used to stream tracking and US data through OpenIGTLink into 3D Slicer version 4.10.2 with the SlicerIGT extension [48]–[50]. The measured data was visualized, recorded and saved in 3D Slicer. Evaluation of the data was performed post-operatively in 3D Slicer and MATLAB. In addition, open-source software ITK-SNAP [72] and in-house developed software WrldMatch were used for CT bone segmentation and CT bone matching, respectively.

4.2.2 Patient selection

A prospective feasibility study on patients with abdominal cancer was started at the NKI-AvL, Amsterdam, The Netherlands. In the period from June 2020 to January 2021, patients of 18 years and older scheduled for navigated open abdominal tumor surgery have been selected. The specific surgical procedure varied for each patient, such as an APR, LND or nephrectomy. The study protocol was approved by the institutional review board and informed consent was obtained of all patients.

4.2.3 Data collection

Prior to each measurement, a 3D Slicer scene was set up with a patient specific model of the pelvic bone from the pre-operative CT-scan. This bone model was created in ITK-SNAP with the active contour segmentation mode. Sometimes, manual adaptations were made to remove all holes from the bone model, which was important for the US registration method. In 3D Slicer, the vertebrae and both femurs were manually removed from the bone model. Afterwards, three landmarks were pre-operatively selected on the bone model for the initial registration: on the left anterior superior iliac spine, the right anterior superior iliac spine and the pubic bone.

To ensure consistent US scanning with minimal surgical workflow interruption, an US scanning protocol was designed (Appendix A). Each patient measurement consisted of four phases, namely preparation, initial registration, tracked US measurement in Trendelenburg and tracked US measurement horizontally. During the preparation phase, the software and hardware was set up and three patient sensors were attached to the patient with surgical tape. Two patient sensors were located on the back at the height of the lumbosacral vertebra and one at the front next to the iliac crest. After anesthesia, the patient was correctly positioned on the surgical bed. This was very important, because patient movement between the US measurement and CBCT-scan could lead to an unreliable comparison between both registration methods.

The second phase, initial registration, was performed by US scanning the patient's pelvic bone at approximately the same three virtually marked locations. For each location, a new landmark was manually selected on the bone surface in the US image in 3D Slicer. When all three landmarks were selected, an ICP algorithm automatically computed the initial transformation from EMTS to CT (${}^{CTinit}T_{EMTS}$). After initial registration, real-time movements of the US probe relative to the patient correlated with the virtual movements in 3D Slicer. Figure 4.1 shows the 3D Slicer interface during US scanning after initial registration with the three applied landmarks. The location of the bone surface in the US image corresponds with the pre-operative bone model fairly well, which helped in correctly orienting the US probe during the subsequent measurements.

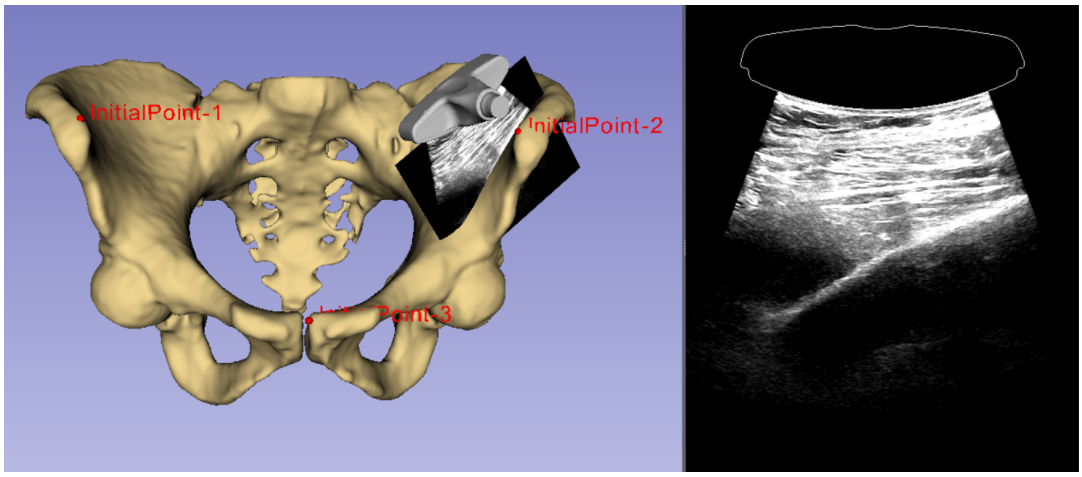

FIGURE 4.1: US scanning interface in 3D Slicer after initial registration. The three landmarks used for initial registration are indicated by red dots.

Tracked US measurements were performed twice for each patient: first in Trendelenburg (tilting of 10 degrees) and second in horizontal patient position. During each measurement, three structures of the pelvis were visualized, namely the right os ilium, left os ilium and os pubis, see Figure A.1. For the right and left os ilium, an US sweep was made at the lateral and medial side of the bone. The os pubis was visualized from different angles by tilting the US probe. Mostly, the US probe was held orthogonal to the bone surface to improve the bone surface intensity on the US image. All US and tracking data was recorded and saved in 3D Slicer. Sometimes, the third patient sensor ventral of the patient was relocated and its tracking information was recorded. Afterwards, the CBCT scan was made and the normal surgical navigation workflow continued.

4.2.4 CBCT registration method

In this patient study, the transformation from EMTS coordinates to CT coordinates (${}^{CT}T_{EMTS}$) was computed for each patient using the CBCT registration method, which has been extensively described in subsection 1.2.4. For the computation of ${}^{CT}T_{CBCT}$, the CBCT-scans (mostly two) and pre-operative CT-scan were loaded into WrldMatch. Within that program, a rigid image registration was performed based on the bone's intensity from each CBCT-scan to the pre-operative CT-scan. Afterwards, the resulting transformations (${}^{CT}T_{CBCT}$) and mentioned (CB)CT-scans were loaded into 3D Slicer. In that program, six landmarks were selected on the transformed CBCT-scans, one for every 5DOF sensor of each patient sensor. Since the CBCT-scans were already transformed to the pre-operative CT scan, the selected landmarks were expressed in CT coordinates. The corresponding 6 landmarks in EMTS coordinates were selected using the EM tracking information of the patient sensors at the end of the second (horizontal) recording. In 3D Slicer, an ICP registration algorithm computed the transformation ${}^{CT}T_{EMTS}$, which was inverted to create the reference registration ($T_{CBCT} = {}^{CT}T_{EMTS}{}^{-1}$) for further analysis.

4.2.5 US registration method

Post-operatively, the transformation from EMTS coordinates to CT coordinates (${}^{CT}T_{EMTS}$) was computed with the US registration method as well (subsection 1.2.6). First of all, a correction for possible patient movement was made, since compression of the US probe onto the patient's skin might induce a small translation towards the TTFG. This was done by applying an ICP algorithm on the location of the two dorsal patient sensors in each image frame relative to its location at the end of the measurement without US probe compression. The resulting translation was automatically applied on the US image for each frame. Afterwards, the recorded US images were reviewed and landmarks were manually selected at the bone surface on these images. An example of ten selected landmarks (red points) has been visualized in Figure 4.2. Due to the initial registration, the landmarks were already located near the bone surface of the 3D model. Approximately 50 landmarks were selected on each location (lateral and medial side of the right and left ilium and the pubic bone), resulting in a total of approximately 250 landmarks. Since the US image was transformed to the EMTS coordinate system with the spatial calibration method of Chapter 3, the selected landmarks were expressed in EMTS coordinates. This method was applied for each patient on both the horizontal and Trendelenburg measurement data.

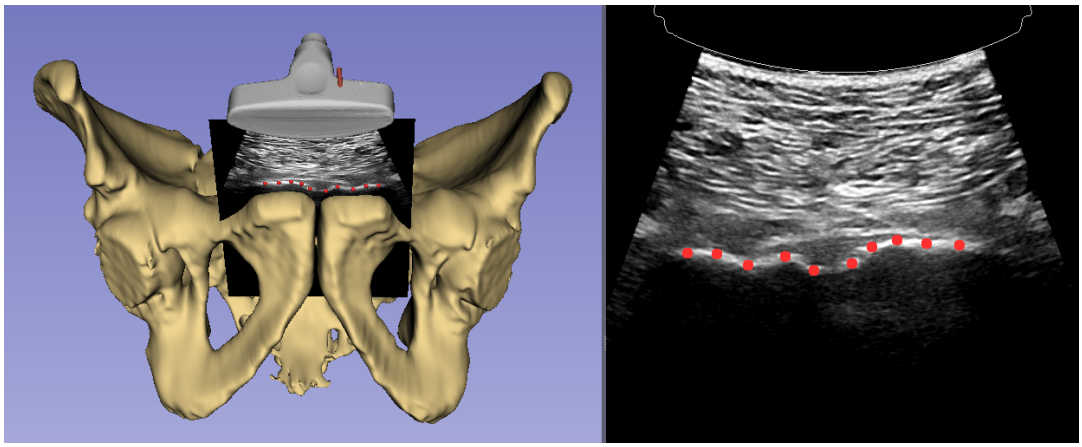

FIGURE 4.2: Post-operative landmark selection of the bone surface on US images. A recorded 2D ultrasound image of the pubic bone (right), ten landmarks (red dots) and their location relative to the initial transformed 3D bone model (left) are visualized.

Three different rigid registration methods were applied for the computation of ${}^{CT}T_{EMTS}$. Prior to each registration, the initial registration (${}^{CTinit}T_{EMTS}$) was applied on the US bone landmarks for improved results. Within 3D Slicer, the "fiducials to model registration" module was applied, which is a part of the Slicer-IGT module. This module applies an ICP algorithm using the landmarks in the selected order. The other two registrations were computed within MATLAB using an ICP point cloud registration algorithm. Here, the pre-operative bone model and the selected landmarks were loaded separately into MATLAB as point clouds. The ICP algorithm minimized the distance between both point clouds according to either a point to point or a point to plane method, resulting in the transformation ${}^{CT}T_{CTinit}$. Combination with the initial transformation resulted in the final US registration:

$$ {}^{CT}T_{EMTS} = {}^{CT}T_{CTinit}\,{}^{CTinit}T_{EMTS} \tag{4.1} $$

For each patient, all three registration methods were applied on the horizontal and Trendelenburg landmarks, separately. For further analysis, the resulting transformations were inverted to define the US registration in horizontal patient position ($T_{US\_hor} = {}^{CT}T_{EMTS}{}^{-1}$) and the US registration in Trendelenburg ($T_{US\_tren} = {}^{CT}T_{EMTS}{}^{-1}$).

4.2.6 Accuracy evaluation

The through US registration computed transformation in horizontal patient position (T_{US_hor}) was compared with the reference (T_{CBCT}) by calculating the TRE. Six target points (p_{target}) were selected at several anatomical landmarks on the pre-operative CT-scan: the aortic bifurcation, the left and right iliac bifurcation and within the pelvic cavity. The three landmarks in the pelvic cavity were selected ventral of the coccyx and on the left and right side at the height of the proximal rectum. Afterwards, all target points were transformed from CT to EMTS coordinates by T_{CBCT} and T_{US_hor}, and the TRE was defined as the euclidean distance between the transformed positions with the following equation: [25]

$$ TRE_{US}(p_{target}) = ||T_{US\_hor}(p_{target}) - T_{CBCT}(p_{target})|| \tag{4.2} $$

Similarly, the target registration discrepancy (TRD) between the horizontal and Trendelenburg US registration was computed to evaluate the influence of alternate patient positions on the tracking accuracy at the defined targets:

$$TRD_{tren}(p_{target}) = ||T_{US\_tren}(p_{target}) - T_{US\_hor}(p_{target})|| \tag{4.3}$$

Both TRE_{US} and TRD_{tren} were further evaluated by computing the translational difference in x-, y- and z-direction between the transformed target points for each patient. This information was used to investigate if a position error in one specific direction might be causing an increased TRE or TRD.

In addition, the RMSE of each registration method was computed automatically within 3D Slicer and MATLAB, which provides an indication of the registration accuracy at the location of the registered fiducials. These fiducials were the patient sensors for the CBCT registration and the bone surface landmarks for the US registration method.

4.3 Results

4.3.1 Patient characteristics

During the time period of this study, ten patients have been included in total. Some relevant patient characteristics are listed in Table 4.1, such as the gender, age, surgery type and body mass index (BMI) before the date of surgery. In addition, the mean Hounsfield unit (HU) of the pre-operatively segmented bone model is reported. For most patients, the main reason to use surgical navigation was for the localization of malignant lymph nodes during surgery. During the US measurements on the OR, the BK US device was applied on seven patients, while the Clarius US device was used on the other three patients. Two patients (1 and 3) were transferred to another OR after the US measurements and CBCT-scan were acquired, due to the possibility of intraoperative brachytherapy. Since patient anesthesia was performed after OR transfer, both patients were conscious during the data collection phase, which might have caused increased patient movement during US acquisition in Trendelenburg. Furthermore, patient 2, 3 and 9 were accidentally repositioned just before the CBCT-scan was made. This caused a difference in the physical position of the patient sensors between the CBCT-scan and horizontal US measurement, which might have led to unreliable results.

TABLE 4.1: Summary of patient age, gender, surgery type, BMI, mean HU and applied US device.

Patient	Age	Gender	Surgery type	BMI (kg/m^2)	Mean HU	US device
1[a]	66	M	APR	34.6	351	BK
2[b]	61	M	Inguinal LND	34.9	314	BK
3[a,b]	48	M	APR	21.7	306	BK
4	78	M	Nephrectomy & para-aortic LND	25	368	BK
5	50	M	TME	29.3	295	BK
6	52	M	APR & iliac LND	25.2	379	BK
7	32	F	Nephrectomy & para-aortic LND	24.6	323	BK
8	69	M	Cystoprostatectomy & pelvic LND	29.6	313	Clarius
9[b]	63	F	Iliac LND	24.4	295	Clarius
10	49	F	Iliac LND	19.1	361	Clarius

[a]Patient was conscious during US and CBCT measurements

[b]Patient was repositioned just before CBCT-scanning

4.3.2 Ultrasound registration accuracy

A visual representation of the resulting US registration in 3D Slicer for patient 7 is shown in Figure 4.3. Here, the landmarks, which were selected at the bone surface in US images, are visualized relative to the pre-operative bone model. Figure 4.3b shows that the initial registration procedure results in an approximate corresponding location of the bone model with the landmarks. After application of the fiducials to model registration algorithm in 3D Slicer, the landmarks are located even closer to the bone surface of the pre-operative model (Figure 4.3c). In this subfigure, most landmarks are located directly at the bone surface, especially at the pubic bone. However, multiple landmarks are located inside the bone model at both ilia. Visually, the results of this patient were representative of all other included patients.

(A) All landmarks, selected at the bone surface on US images

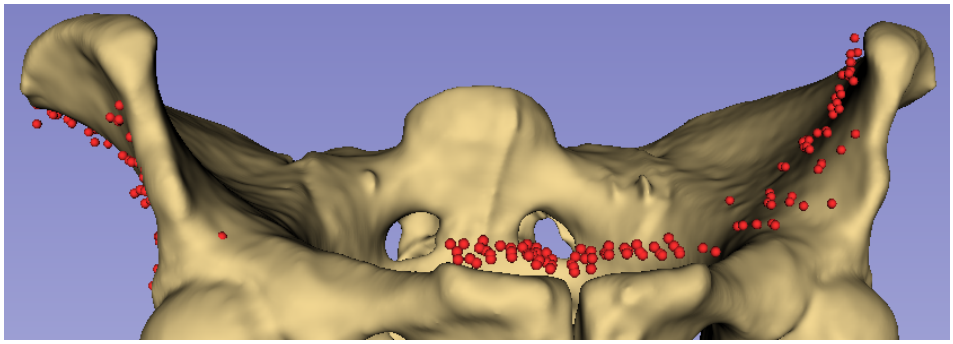

(B) Selected landmarks and initial transformed bone model

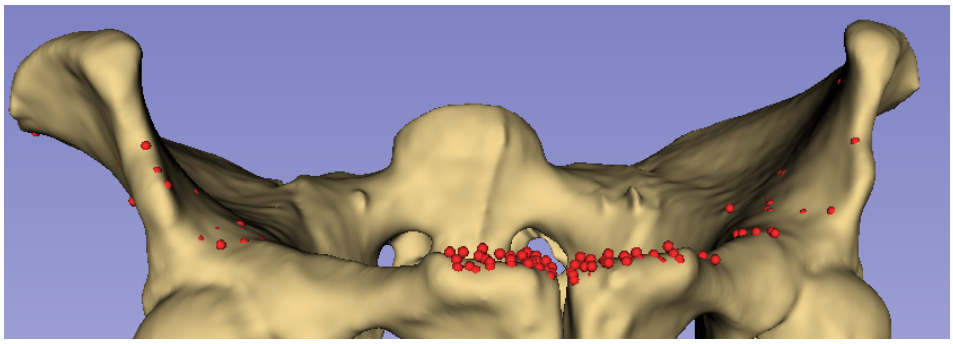

(C) Selected landmarks and through US registration transformed bone model

FIGURE 4.3: US registration of patient 7 in horizontal patient position. In each subfigure (A-C), the selected bone surface landmarks (red points) are represented in EMTS coordinates. The 3D bone model was transformed through initial registration (B) and US registration in 3D Slicer (C).

The US registration accuracy was quantitatively evaluated by comparing it with the CBCT registration method using TRE_{US}, which is visualized as a grouped box plot for all three applied US registration methods in Figure 4.4. For all patients combined, an average TRE of 5.7 mm was found. Moreover, the average TRE_{US} was higher for the patients scanned with the Clarius US device (8.8 mm) compared to the BK US device (4.3 mm). However, the TRE_{US} of patient 2, 3, 9 and 10 are relatively high compared to the other patients. As stated in subsection 4.3.1, the results of patient 2, 3 and 9 could be unreliable due to patient movement during the measurement phase. Exclusion of these patients results in an average TRE_{US} with the BK US device of 2.6 mm ($\pm$ 0.7 mm), 2.7 mm ($\pm$ 0.8 mm) and 2.8 mm ($\pm$ 0.8 mm) for the Slicer, ICP-point and ICP-plane registration method, respectively. The average TRE_{US} with the Clarius US device after exclusion was 8.4 mm ($\pm$ 5.2 mm), 8.2 mm ($\pm$ 5.4 mm) and 8.5 mm ($\pm$ 5.4 mm) for the respectively corresponding registration methods. A list of the TRE_{US} for each patient has been provided in Table B.1 of Appendix B. In addition, the RMSE of the CBCT registration (T_{CBCT}) and each US registration (T_{US_hor} and T_{US_tren}) has been listed in Table B.2. Noteworthy is the high RMSE of T_{CBCT} for patient 10, which might have a correlation with the high TRE_{US} of this patient.

All three evaluated US registration methods resulted in similar values of TRE_{US}. On average, the Slicer registration method produced a slightly lower TRE than the ICP-point and ICP-plane registration method. However, this difference is within sub-millimeter range.

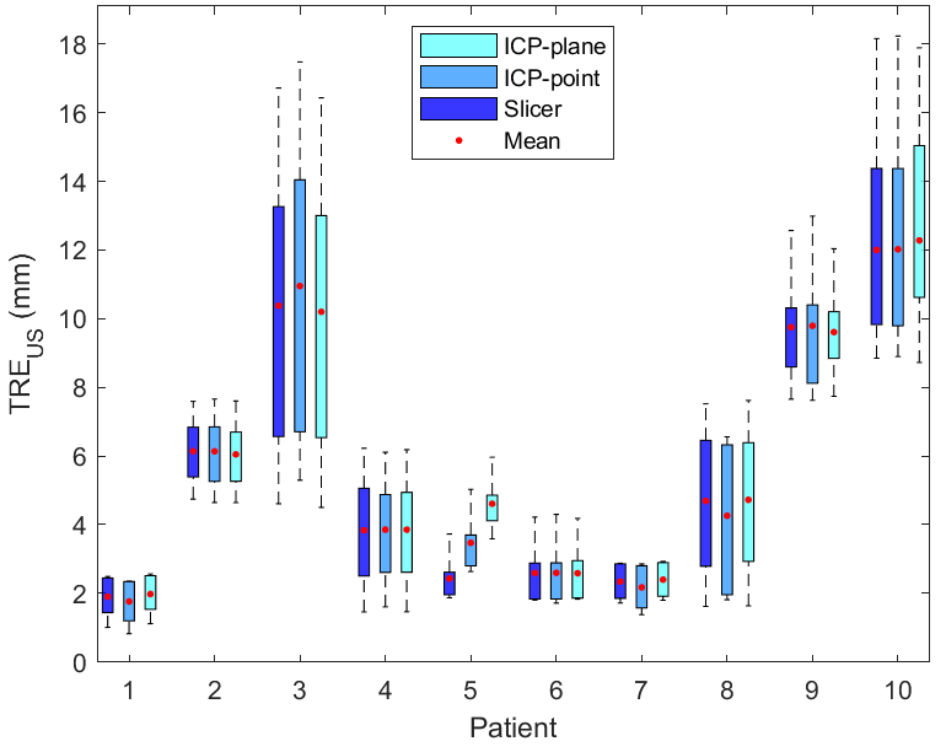

FIGURE 4.4: Grouped box plot of TRE_{US} of the Slicer, ICP-point and ICP-plane US registration method for all ten patients. The mean TRE_{US} is visualized by a red dot.

4.3.3 Influence of patient position on registration accuracy

The influence of the patient position on the registration accuracy was evaluated by comparing the horizontal US registration with the Trendelenburg US registration using TRD_{tren}, which is visualized as a grouped box plot in Figure 4.5. A limit was set at 19 mm since the average TRD_{tren} of patient 1 (108 mm) and 3 (58 mm) were much higher compared to the other patients. Since the US registration method is equal in both patient positions, a high TRD_{tren} could indicate a registration discrepancy due to the shift in patient position. The value of TRD_{tren} varies between 4 and 115 mm, with an average of approximately 22 mm. However, patient 1 and 3 were both conscious during the US measurements and patient movement was visually noticed. Exclusion of these two patients resulted in an average TRD_{tren} of 7.0 mm ($\pm$ 4.8 mm), 7.4 mm ($\pm$ 4.6 mm) and 6.7 mm ($\pm$ 3.6 mm) for the Slicer, ICP-point and ICP-plane registration method, respectively. A complete list of the TRD_{tren} values for each patient has been provided in Table B.1 of Appendix B.

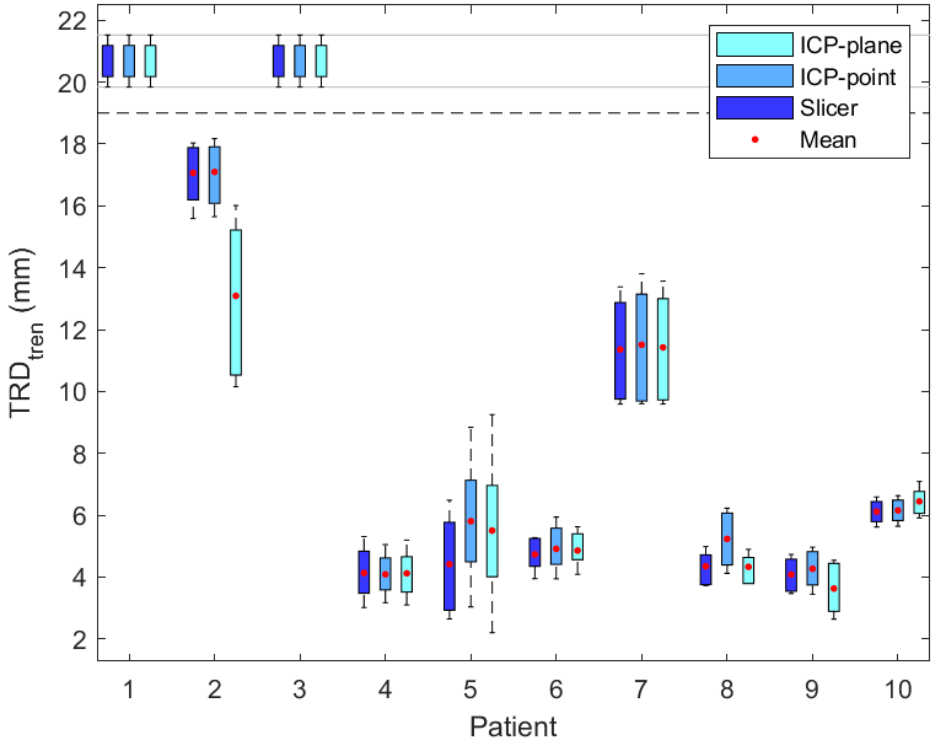

FIGURE 4.5: Grouped box plot of TRD_{tren} of the Slicer, ICP-point and ICP-plane US registration method for all ten patients. A limit was set at 19 mm and the mean TRD_{tren} is visualized by a red dot.

In Figure 4.6, the through T_{CBCT}, T_{US_hor} and T_{US_tren} transformed target points have been visualized in 3D relative to the pelvis of patient 7. Visually, the locations of the horizontal US transformed points (blue) roughly correspond with the location of the CBCT transformed points (green). However, a translation difference of more than 1 mm in posterior direction could be observed for each target point. For the target points transformed through US registration in Trendelenburg (red), a much larger distance to the other target points is noticeable. Visually, this translation offset occurs mostly in superior and posterior direction.

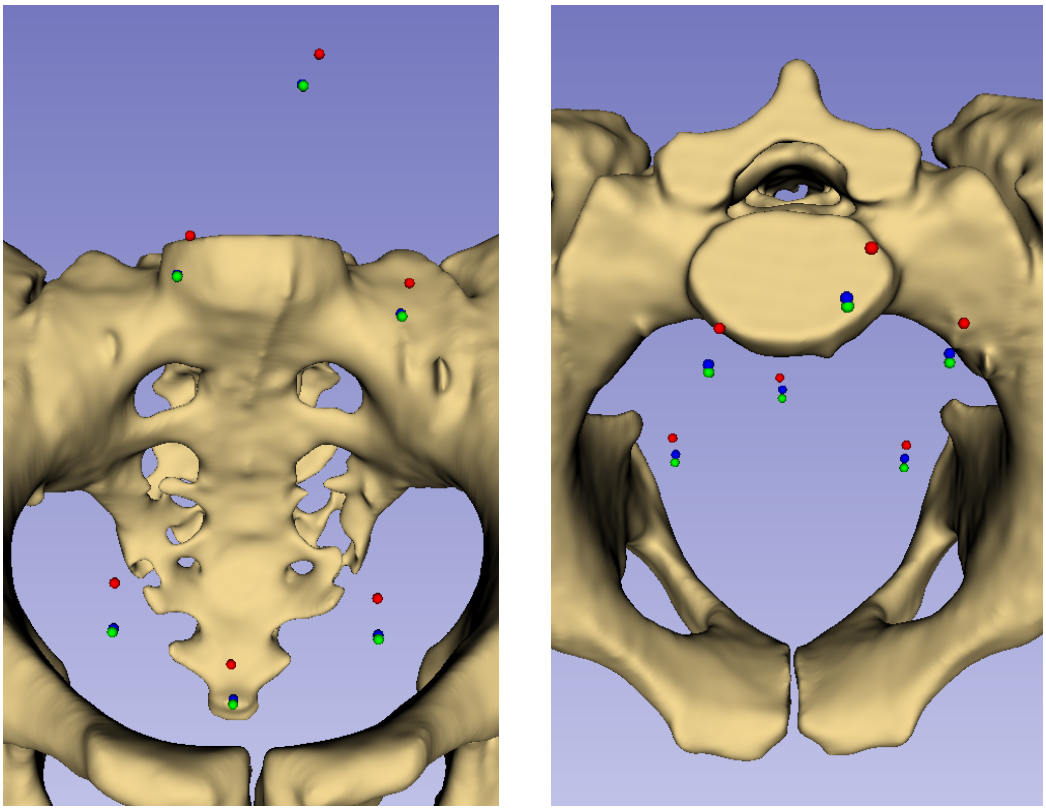

FIGURE 4.6: Anterior (left) and superior (right) view of the target points for patient 7 transformed to the EMTS coordinate system through CBCT registration (green), Slicer US registration in horizontal position (blue) and Slicer US registration in Trendelenburg (red). The target points have a diameter of 3 mm and the bone model was transformed with the CBCT registration.

For all other patients, a translational difference in superior direction for $T_{US\_tren}(p_{target})$ compared to $T_{US\_hor}(p_{target})$ was found as well. The mean offset in superior direction for all ten patients was 18.4 mm ($\pm$ 31.0 mm). Exclusion of patient 1 and 3 resulted in a mean offset in superior direction of 6.5 mm ($\pm$ 4.8 mm). This suggests that the pelvic bone and target points of the patient are located more superior when the surgical bed is tilted into Trendelenburg compared to a horizontal position.

4.4 Discussion

In this patient study, a novel US registration method based on the pelvic bone was applied in a clinical setting to correlate pre-operative imaging data with the patient's position on the OR. Comparison with the current reference showed an average US registration accuracy of 2.6 mm at surgical targets, such as the aortic bifurcation, when applying the tracked BK US probe. For the application of the proposed US registration method in clinical practice, one of the major requirements is to achieve a clinically feasible tracking accuracy during surgery of less than 5 mm. Currently, the CBCT registration method achieves an average tracking accuracy at surgical targets of 3-4 mm [17], [18]. Therefore, the TRE for the US registration found in this study (2.6 mm) suggests that surgical navigation through US registration should be feasible and accurate.

However, objective evaluation of the TRE is difficult due to a small uncertainty introduced by the CBCT registration method, which is assumed to be the reference in this study. For instance, the RMSE of the CBCT registration in this study varied between 0.3 and 7.1 mm, which is a tracking inaccuracy at the location of the patient sensors. Since these patients sensors were attached to the skin of the patient, the tracking error at the location of target points is unknown and might differ from the real position as well. Therefore, the computed TRE_{US} in this study could be worse due to CBCT registration errors. For instance, the patients with the highest TRE_{US} (patient 3, 9 and 10), had the highest RMSE of T_{CBCT} as well. This suggests that for these patients the reported TRE_{US} might be worse than the real tracking error if the US registration method would be clinically implemented. Therefore, it would be interesting to apply the US registration method during surgery and evaluate the clinical TRE using real anatomical landmarks of the patient in future studies.

In this study, two tracked US devices were clinically applied, namely the BK and Clarius US device. For all patients, the average TRE_{US} was twice as high when the Clarius US device was applied (8.7-8.9 mm) compared to the BK US device (4.2-4.4 mm). However, only three patients were measured with the Clarius device of which one (patient 9) was repositioned and one (patient 10) had a high CBCT registration RMSE. The third patient (patient 8) had a TRE_{US} of approximately 4.5 mm, which is almost 2 mm higher than the average TRE_{US} acquired with the BK device after exclusion (2.6 mm). These results suggest that the BK provides a better registration than the Clarius US device. Possibly, this difference is caused by the worse calibration accuracy mentioned in Chapter 3 for the Clarius US device (3.1 mm) compared to the BK (1.5 mm). Furthermore, the applied frequency of Clarius (2.5 MHz) was lower than BK (7.5 MHz), which causes a decrease in image resolution. Therefore, accurate visualization of the bone surface was much harder when applying the Clarius US device compared to the BK. Finally, EM jitter was noticed during US acquisition with the Clarius on patients. Therefore, interference of the Clarius US probe on the EMTS could still have some impact on the registration accuracy.

A decrease in surgical navigation accuracy when altering the patient position after CBCT-scanning is a known issue at the NKI-AvL [17], [18]. Currently, a manual correction is made by applying a translation during surgery using real-time tracking information of a surgical pointer targeted at specific anatomical structures, such as the aortic bifurcation. If a manual correction is required, a translation difference was mostly applied in caudal-cranial direction [18]. On average, a correction of 9.4 mm in this direction was necessary when patients were positioned into Trendelenburg [18]. The results of this tracked US study indicated a translational offset of 6.5 mm between the US measurements in horizontal and Trendelenburg patient position in the same (cranial) direction. For these measurements, the surgical bed was tilted into 10 degrees Trendelenburg, while this angle is, oftentimes, much higher during surgery (20-30 degrees). This implies that the reported offset of 6.5 mm might be higher if the table was tilted into 20-30 degrees Trendelenburg, which would approximate the translational difference of 9.4 mm mentioned by Kok *et al.* [18]. Since the US registration method could compensate for this cranial offset, this method could achieve a better registration accuracy than the conventional CBCT method in altered patient positions, such as Trendelenburg.

The specific application of tracked US for patient registration prior to surgical abdominal tumor navigation has not been proposed in literature yet. However, surgical navigation is commonly applied in orthopedic and neurosurgery [73]. For example, Barratt *et al.* applied an optically tracked US device for bone registration in orthopedic surgery [74]. A similar registration method was applied to register

US-derived bone surface points to the CT bone surface based on the pelvic bone of cadavers. Here, a TRE of approximately 2.2 mm was reported, which is similar to the TRE of 2.6 mm found in this study. However, the surgical target in their study was located at the spherical region of the acetabulum, which might differ from targets inside the pelvic cavity.

On the other hand, registration with a tracked US device has some limitations. For instance, the image quality of the bone surface on US is significantly worse than on a CBCT-scan. Some user experience is required to adequately position and move the US device to optimally visualize the bone surface. This could be an issue for clinical implementation when intra-operative re-registration is desirable. Furthermore, an increased amount of fat tissue complicates orthogonal positioning of the US probe on the bone surface and the bone intensity highly varies between patients. Additionally, an increased pressure of the US probe on the patient's skin could slightly rotate the pelvis leading to an inaccurate registration. This might clarify why most landmarks were located inside the bone model after registration in Figure 4.3c. Other possibilities of inaccurate bone surface localization on US images could be caused by the spatial calibration of the fixed EM sensor or the SOS difference between human tissue and what is assumed by the US device. Application of an SOS correction method might be able to improve the positional accuracy in US images, as suggested by Fontanarosa *et al.* [75].

While the applied US registration method proved to be feasible, manual landmark selection on the recorded US images still is a time consuming process. Depending on the length and quality of the US recordings, 15 to 30 minutes were required to select all landmarks for one patient position. For clinical implementation, a reduced registration time is desirable, which is possible by reducing the number of required landmarks. However, omitting the landmarks at either the medial iliac bone, lateral iliac bone or pubic bone for the patients in this study resulted in a worse average TRE_{US}. This suggests that, on average, the selection of more landmarks results in a better registration. Another option is to automate the registration process by implementing an automatic segmentation algorithm. However, this could be a challenging task due to the large number of artifacts, noise and other high intensity structures, such as muscles, throughout the US image.

4.5 Conclusion

With a reported TRE of 2.6 mm, tracked US is a promising alternative to the CBCT-scan for patient registration prior to surgical abdominal tumor navigation. Furthermore, performing US registration when the patient is in the correct surgical position could improve the navigation accuracy while removing the need for manual correction during surgery. However, the required registration time should be reduced to improve clinical efficiency.

Chapter 5

Recommendations

Ultimately, the goal of applying tracked US for patient registration is to overcome the current limitations of the intra-operative CBCT-scan, such as clinical workflow interruption and radiation exposure, and achieve an acceptable tracking accuracy during surgical navigation regardless of the patient's position. The results of this patient study were promising for the BK US device, but accurate data was only obtained for four patients. Therefore, an option is to include more patients to evaluate the consistency of the reported mean TRE of 2.6 mm. However, it could take several months to include significantly more patients, since navigation surgery is scheduled approximately once per month at the NKI-AvL. Furthermore, using the CBCT registration method as a reference leaves a small uncertainty in the computation of the TRE, as discussed in Chapter 4. Additional experience during this patient study showed that accidentally moving the patient between the US and CBCT-scan occurs relatively often, which leads to patient exclusion. Therefore, it would be wise to expand the current patient study by either intra-operative validation of the US registration accuracy or using Doppler US imaging for the registration of pelvic-abdominal vessels.

The first option is to evaluate the clinical navigation accuracy during surgery after application of the tracked US registration method. Instead of using the CBCT registration method as a reference, EM tracking information from the surgery could be applied for the computation of the TRE. During abdominal navigated surgery, the surgeon could use a sterile EM pointer to indicate certain anatomical landmarks inside the patient, such as the aortic bifurcation. The EM tracked position of these landmarks could be stored for post-operative evaluation of the US registration accuracy. However, it is important that the US measurements are performed at the same patient position and tilting of the surgical bed as during surgery to achieve a reliable comparison. Therefore, US acquisition might need to take place after CBCT scanning and before draping of the patient. For example, if the surgery is performed in Trendelenburg, the surgical bed could be tilted into this position after acquisition of the CBCT-scan. Then, tracked US measurements could be performed and the surgical procedure can start in the same patient position.

The second option is to evaluate the possibility of using pelvic-abdominal vessels as US registration targets instead of the pelvic bone. At the NKI-AvL, vessel-based US registration is already performed for navigated liver surgery [76], [77]. Their experience might be helpful to investigate possibilities for abdominal navigation. Another study showed the possibility of 3D US-based navigation during abdominal interventions in which the abdominal aorta and renal arteries were tracked using Doppler US [78]. A promising correlation between CT and Doppler US data was shown. However, they applied the US technique as a validation method and not for the registration itself. Nypan *et al.* applied a vessel-based rigid registration of the abdominal aorta, renal arteries and iliac arteries on a phantom [79]. Doppler

US images were registered to a CT-scan using the arterial centerline or with a 3D-3D registration method. A TRE of 3.7 and 3.2 was achieved for the centerline and 3D-3D registration method, respectively [79]. This study suggests that the pelvic-abdominal arteries might be appropriate targets for tracked US registration.

Some advantages of using vessels as registration targets instead of the pelvic bone is that an automatic segmentation algorithm is easier to develop because of the Doppler information. An automatic segmentation algorithm significantly reduces the registration time, which is favourable for clinical application. Furthermore, most surgical targets, such as malignant lymph nodes, are located near the pelvic-abdominal arteries. If the registration of these arteries is accurate, navigation at the surgical targets should have approximately the same accuracy. However, a limitation is that the vessels are round structures, which might cause an incorrect registration along the length of the vessel. Therefore, US visualization of specific anatomical landmarks of the vessels, such as the aortic and iliac bifurcations, should be evaluated.

An initial exploration on tracked US for vessel registration was done after data acquisition on the final patient in the study of Chapter 4. The EM tracked Clarius US device was applied in combination with Doppler to visualize the external iliac arteries and veins. In Figure 5.1, a 3D Slicer interface of this measurement is shown. Here, the pre-operative model of the pelvic bone, arteries and veins are transformed to the EMTS coordinate system with the CBCT registration. The segmentation outlines of the arteries and veins are visualized on the US Doppler image as well. On this US image, the locations of the right external iliac artery and vein correspond with the pre-operative model, which is very promising. Therefore, future research should focus on the possibilities of vessel-based registration in addition to the pelvic bone registration method.

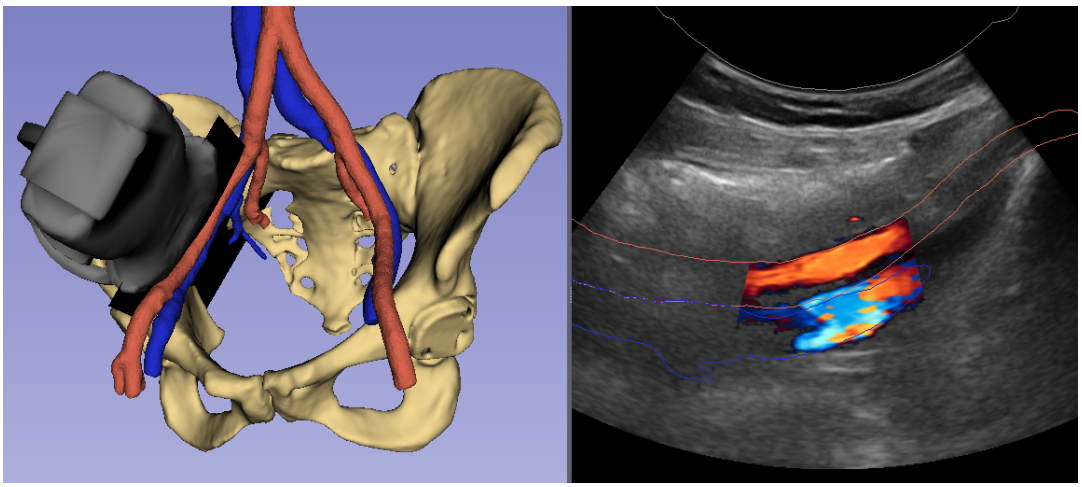

FIGURE 5.1: Tracked US interface in 3D Slicer with Doppler function enabled. A 3D model of the Clarius US device (grey), pelvic bone (beige), arteries (red) and veins (blue) is visualized on the left with the 2D Doppler US image on the right.

The main limitation of the current US bone registration method is the time consuming process of manual bone surface landmark selection, which needs to be reduced for clinical application. Therefore, the development of an automatic bone segmentation algorithm is recommended. However, this could be a challenging task due to the noise, artefacts or other structures with high intensities in US images. Zettinig *et al.* proposed a method of image filtering prior to bone segmentation [80].

It is feasible to use convolutional neural networks to denoise US images, which has the potential to highlight application specific structures automatically. For US image denoising, a relatively simple network with U-net architecture should suffice [81]. Salehi *et al.* trained a convolutional network for automatic bone segmentation, which was applied on a cadaver study, resulting in a surface error of the pelvic bone of 0.6 mm [82]. The results of their denoising and automatic bone segmentation are visualized in Figure 5.2, which seems very promising to apply at the NKI-AvL as well.

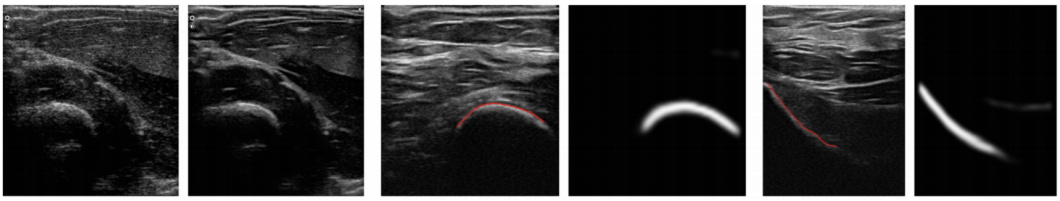

FIGURE 5.2: Example of automatic denoising (a) and bone segmentation (b,c) using a convolutional neural network [80].

As the results of this study have shown, the accuracy of the tracked US registration method depends on the applied US device. Despite the fact that a large part of this study focused on the implementation of the wireless Clarius US device, the conventional BK US device showed better results for the calibration and patient registration. Moreover, the Clarius US device had several issues, such as interference with the EMTS, Wi-Fi connection instability and a relatively low frequency resulting in a worse image resolution. Therefore, it is advised to apply the BK or other high frequency (10-15 MHz) US probes for future research on this topic. These high frequency US devices show an increased image resolution, which makes the scanning process during surgery much easier. In addition, a high image resolution might ease the development of an automatic bone segmentation algorithm.

On the other hand, the Clarius US device still has some promising features that could be further evaluated, such as elastography and an embedded IMU. The use of elastography for bone surface recognition was briefly tested with other US devices. However, accurate segmentation seemed difficult, since small movements of the US probe caused a lot of noise on the elastography image. Especially the IMU data might be useful to track the US device without an EMTS as stated by Prevost *et al.* [59]. However, drift might be an issue when measuring for long trajectories. Validation of the IMU with the OTS might provide insight of the tracking accuracy of the IMU, but more research on this topic is required.

Chapter 6

General conclusions

The main objective of this thesis was to evaluate the feasibility and accuracy of EM tracked US registration for abdominal navigation surgery to potentially replace the currently applied CBCT registration method. Based on the evaluation of tracked US bone registration in a clinical patient study, it can be concluded that the proposed method is feasible and accurate ($<$3 mm) at surgically relevant targets. In addition, this research clearly illustrated that a different patient position into Trendelenburg has a high impact on the registration accuracy ($>$5 mm). Application of tracked US instead of the CBCT could correct for these discrepancies. However, the true navigation accuracy of this method during surgery is still unknown, which should be evaluated in an intra-operative setting in the future.

While the applicability of tracked US for data collection in the surgical workflow was proven during this research, the manual US bone segmentation process still takes too much time for clinical application (approximately 30 minutes). Therefore, future studies should focus on reducing the registration time, for example by training a convolutional neural network in the development of an automatic bone segmentation algorithm. In addition, vessel-based US registration might be of additional value to the current bone registration method, which should be explored in future research.

In conclusion, the proposed tracked US registration method has the potential to reach a clinically acceptable navigation accuracy within 5 mm regardless of the position of the patient and surgical bed on the OR. Therefore, application of this method could overcome the current limitations of CBCT registration to improve the usability of navigation on abdominal tumor surgery and, possibly, patient outcomes.

Appendix A

Ultrasound scanning protocol

1. Place all three patient sensors on the patient (2 on the back, 1 at the front).
2. Open the 3D Slicer patient specific scene (double click on file).
3. Activate the EMTS, US system, start Plus server and verify functionality in 3D Slicer.
4. After anesthesia, correctly position the patient on the surgical bed for the CBCT-scan.
5. Perform initial registration by ultrasound scanning the following structures and selecting a landmark in 3D Slicer:
   (a) Left anterior superior iliac spine
   (b) Right anterior superior iliac spine
   (c) Pubic bone
6. Check if initial registration results are acceptable, otherwise retry.
7. Rotate the surgical bed to reach a Trendelenburg position of 10 degrees.

Start data recording 1

8. Perform ultrasound measurements by scanning:
   (a) Right os ilium, lateral to medial
   (b) Left os ilium, lateral to medial
   (c) Os pubis

End data recording 1

9. Rotate the surgical bed back to a horizontal position.

Start data recording 2

10. Perform ultrasound measurements by scanning:
    (a) Right os ilium, lateral to medial
    (b) Left os ilium, lateral to medial
    (c) Os pubis

End data recording 2

11. If relocation of the third patient sensor at the front is necessary, **run recording 2 for a few extra seconds after sensor relocation.**
12. Save the 3D Slicer scene and continue normal surgical navigation workflow.

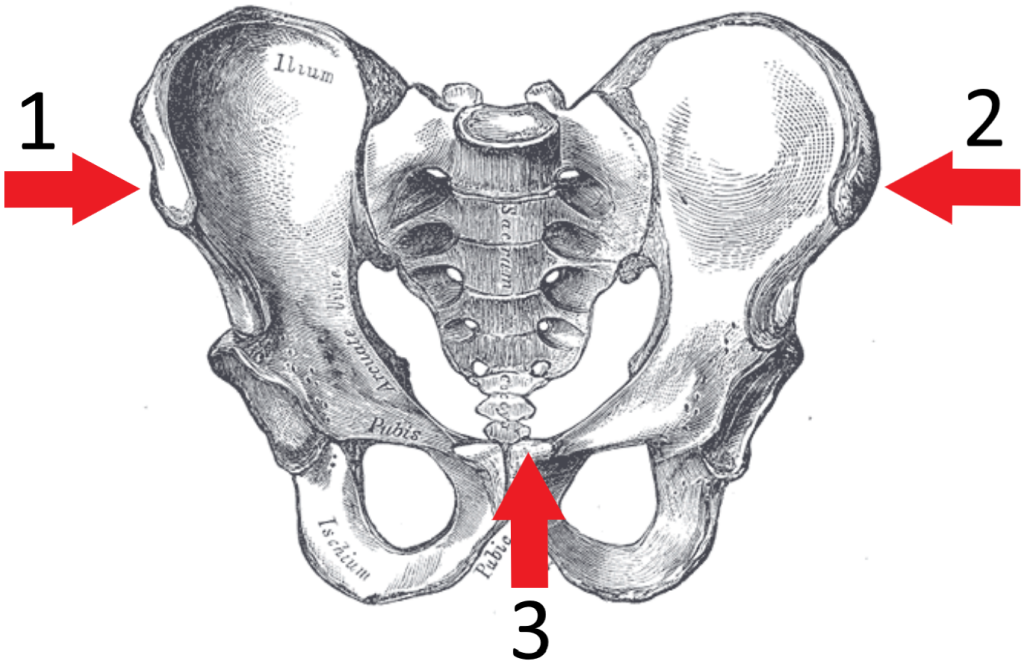

FIGURE A.1: To be scanned structures of the pelvis: right os ilium (1), left os ilium (2) and os pubis (3).

Appendix B

Patient study: list of error values

TABLE B.1: TRE_{US} (mean ± SD) of the horizontal US registration compared to the CBCT registration and TRD_{tren} (mean ± SD) of the horizontal US registration compared to the Trendelenburg US registration for all ten patients and the average. Units are in mm.

Patient	1[a]	2[b]	3[a,b]	4	5	6	7	8	9[b]	10	Average
TRE_{US} Slicer	1.9 ± 0.6	6.1 ± 1.1	10.4 ± 4.7	3.8 ± 1.7	2.4 ± 0.7	2.6 ± 0.9	2.3 ± 0.5	4.7 ± 2.3	9.8 ± 1.7	12.0 ± 3.6	5.6 ± 3.8
TRE_{US} ICP-point	1.8 ± 0.6	6.1 ± 1.1	11.0 ± 4.8	3.9 ± 1.6	2.8 ± 1.3	2.6 ± 0.9	2.2 ± 0.6	4.3 ± 2.0	9.8 ± 1.9	12.0 ± 3.6	5.7 ± 3.9
TRE_{US} ICP-plane	2.0 ± 0.6	6.1 ± 1.1	10.2 ± 4.6	3.9 ± 1.7	3.3 ± 1.3	2.6 ± 0.9	2.4 ± 0.5	4.7 ± 2.3	9.6 ± 1.5	12.3 ± 3.4	5.7 ± 3.7
TRD_{tren} Slicer	104.4 ± 3.0	17.1 ± 1.0	58.4 ± 11.1	4.1 ± 0.9	4.4 ± 1.5	4.7 ± 0.5	11.4 ± 1.6	4.3 ± 0.5	4.1 ± 0.5	6.1 ± 0.4	21.9 ± 33.4
TRD_{tren} ICP-point	115.0 ± 4.4	17.1 ± 1.1	57.7 ± 11.2	4.1 ± 0.7	5.8 ± 2.0	4.9 ± 0.7	11.5 ± 1.8	5.2 ± 0.9	4.3 ± 0.6	6.2 ± 0.4	23.2 ± 36.2
TRD_{tren} ICP-plane	100.4 ± 3.8	13.1 ± 2.5	58.5 ± 11.1	4.1 ± 0.8	5.5 ± 2.4	4.9 ± 0.6	11.4 ± 1.7	4.3 ± 0.5	3.6 ± 0.8	6.4 ± 0.4	21.2 ± 32.4

[a] Patient was conscious during US and CBCT measurements

[b] Patient was repositioned just before CBCT-scanning

TABLE B.2: Root-mean-square error of the CBCT registration (T_{CBCT}), US registration in horizontal position (T_{US_hor}) and in Trendelenburg (T_{US_tren}) for all ten patients and the average (± SD). Units are in mm.

Patient	1	2	3	4	5	6	7	8	9	10	Average
RMSE T_{CBCT}	1.6	0.7	2.7	1.7	0.6	0.3	1.1	0.5	7.1	2.5	1.9 ± 2.0
RMSE T_{US_hor} Slicer	0.9	1.7	1.0	1.2	1.9	1.4	1.5	1.5	1.9	1.5	1.5 ± 0.3
RMSE T_{US_hor} ICP-point	1.3	2.3	1.5	1.5	2.4	1.8	1.8	2.2	2.5	2.2	2.0 ± 0.4
RMSE T_{US_hor} ICP-plane	1.3	2.3	1.5	1.5	2.4	1.8	1.8	2.1	2.5	2.2	1.9 ± 0.4
RMSE T_{US_tren} Slicer	0.4	2.3	1.6	1.2	1.6	1.7	1.9	1.5	1.7	1.5	1.5 ± 0.5
RMSE T_{US_tren} ICP-point	1.0	2.9	2.1	1.6	2.2	1.9	2.2	2.0	2.3	2.0	2.0 ± 0.5
RMSE T_{US_tren} ICP-plane	0.6	3.7	2.1	1.6	2.2	1.9	2.2	2.0	2.2	2.0	2.1 ± 0.8

Bibliography

[1] P. Kumar and M. Klark, *Kumar and Clark's Clinical Medicine, Eighth Edition*. Elsevier Ltd., 2012, pp. 229–302, ISBN: 978-0-7020-4499-1.

[2] A. M. R. Agur and A. F. Dalley, *Grant's Atlas of Anatomy, Twelfth Edition*. Lippincott Williams & Wilkins, 2009, pp. 95–284, ISBN: 978-0-7817-9604-0.

[3] K. L. Moore, A. F. Dalley, and A. M. R. Agur, *Clinically Oriented Anatomy, Seventh Edition*. Lippincott Williams & Wilkins, 2014, pp. 181–438, ISBN: 978-1-4511-8447-1.

[4] World Cancer Research Fund, *Worldwide cancer data*. [Online]. Available: https://www.wcrf.org/dietandcancer/cancer-trends/worldwide-cancer-data (visited on 03/12/2020).

[5] Integraal Kankercentrum Nederland, *Nederlandse kankerregistratie*. [Online]. Available: https://www.iknl.nl/nkr-cijfers (visited on 03/12/2020).

[6] P. Rawla, T. Sunkara, and A. Barsouk, "Epidemiology of colorectal cancer: Incidence, mortality, survival, and risk factors", *Przeglad Gastroenterologiczny*, vol. 14, no. 2, pp. 89–103, 2019. DOI: 10.5114/pg.2018.81072.

[7] F. Mulita and S. K. R. Mukkamalla, *Lymph Node Dissection*, 2020. [Online]. Available: https://www.ncbi.nlm.nih.gov/books/NBK564397/ (visited on 02/18/2021).

[8] M. Świderska, B. Choromańska, E. Dabrowska, E. Konarzewska-Duchnowska, K. Choromańska, G. Szczurko, P. Myśliwiec, J. Dadan, J. R. Ładny, and K. Zwierz, "The diagnostics of colorectal cancer", *Wspolczesna Onkologia*, vol. 18, no. 1, pp. 1–6, 2014. DOI: 10.5114/wo.2013.39995.

[9] J. D. Brierley, M. K. Gospodarowicz, and C. Wittekind, *TNM Classification of Malignant Tumours, Eighth Edition*. John Wiley & Sons, 2017, pp. 1–16, ISBN: 978-1-1192-6357-9.

[10] S. B. Edge, D. R. Byrd, C. C. Compton, A. G. Fritz, F. L. Greene, and A. Trotti, *AJCC Cancer Staging Manual, Seventh Edition*. Springer, 2010, pp. 101–250, ISBN: 978-0-387-88440-0.

[11] S. Stintzing, "Management of colorectal cancer", *F1000Prime Reports*, vol. 6, no. 108, 2014. DOI: 10.12703/P6-108.

[12] A. Stein, D. Atanackovic, and C. Bokemeyer, "Current standards and new trends in the primary treatment of colorectal cancer", *European Journal of Cancer*, vol. 47, no. 3, S312–S314, 2011. DOI: 10.1016/S0959-8049(11)70183-6.

[13] C. D. Athanasiou, J. Robinson, M. Yiasemidou, S. Lockwood, and G. A. Markides, "Laparoscopic vs open approach for transverse colon cancer. A systematic review and meta-analysis of short and long term outcomes", *International Journal of Surgery*, vol. 41, no. 1, pp. 78–85, 2017. DOI: 10.1016/j.ijsu.2017.03.050.

[14] J. M. Parker, T. F. Feldmann, and K. G. Cologne, "Advances in Laparoscopic Colorectal Surgery", *Surgical Clinics of North America*, vol. 97, no. 3, pp. 547–560, 2017. DOI: 10.1016/j.suc.2017.01.005.

[15] T. J. M. Ruers, K. F. D. Kuhlmann, G. L. Beets, N. Kok, A. G. J. Aalbers, R. van der Veen, H. Groen, and J. Nijkamp, "Image-guided surgical navigation for rectal cancer surgery", *European Journal of Surgical Oncology*, vol. 45, no. 2, Pe113, 2019. DOI: 10.1016/j.ejso.2018.10.390.

[16] J. Nijkamp, K. F. D. Kuhlmann, J.-J. Sonke, and T. J. M. Ruers, "Image-guided navigation surgery for pelvic malignancies using electromagnetic tracking", in *Medical Imaging 2016: Image-Guided Procedures, Robotic Interventions, and Modeling*, vol. Proc. SPIE 9786, 2016, p. 97862L. DOI: 10.1117/12.2216213.

[17] J. Nijkamp, K. F. D. Kuhlmann, O. Ivashchenko, B. Pouw, N. Hoetjes, M. A. Lindenberg, A. G. J. Aalbers, G. L. Beets, F. van Coevorden, N. Kok, and T. J. M. Ruers, "Prospective study on image-guided navigation surgery for pelvic malignancies", *Journal of Surgical Oncology*, vol. 119, no. 4, pp. 510–517, 2019. DOI: 10.1002/jso.25351.

[18] E. Kok, R. van Veen, J. Nijkamp, H. Groen, N. Hoetjes, W. Heerink, G. L. Beets, A. G. J. Aalbers, K. F. D. Kuhlmann, and T. J. M. Ruers, "First Clinical Results of Image-Guided Navigation in Locally Advanced Primary and Recurrent Rectal Cancer Patients", *European Journal of Surgical Oncology*, vol. 46, no. 2, e86, 2020. DOI: 10.1016/j.ejso.2019.11.204.

[19] A. M. Franz, T. Haidegger, W. Birkfellner, K. Cleary, T. M. Peters, and L. Maier-Hein, "Electromagnetic tracking in medicine -A review of technology, validation, and applications", *IEEE Transactions on Medical Imaging*, vol. 33, no. 8, pp. 1702–1725, 2014. DOI: 10.1109/TMI.2014.2321777.

[20] T. Koivukangas, J. P. A. Katisko, and J. P. Koivukangas, "Technical accuracy of optical and the electromagnetic tracking systems", *SpringerPlus*, vol. 2, no. 90, 2013. DOI: 10.1186/2193-1801-2-90.

[21] Z. Yaniv, E. Wilson, D. Lindisch, and K. Cleary, "Electromagnetic tracking in the clinical environment", *Medical Physics*, vol. 36, no. 3, pp. 876–892, 2009. DOI: 10.1118/1.3075829.

[22] Northern Digital Inc., *Aurora Electromagnetic Tracking System*. [Online]. Available: https://www.ndigital.com/medical/products/aurora (visited on 03/24/2020).

[23] Northern Digital Inc., *Aurora Sensors, Tools & Accessories*. [Online]. Available: https://www.ndigital.com/medical/products/tools-and-sensors (visited on 03/24/2020).

[24] L. Noltes, "A study into laparoscopic surgical navigation for colorectal cancer patients without a hybrid operating room", M3 Technical Medicine Thesis, University of Twente, 2019, pp. 1–56.

[25] D. L. G. Hill, P. G. Batchelor, M. Holden, and D. J. Hawkes, "Medical image registration", *Physics in Medicine and Biology*, vol. 46, no. 3, R1–R45, 2001. DOI: 10.1088/0031-9155/46/3/201.

[26] J. M. Fitzpatrick, D. L. G. Hill, and C. R. Maurer Jr., "Chapter 8: Image Registration", in *Handbook of Medical Imaging Vol 2*, SPIE Press, 2000, pp. 449–506, ISBN: 0-8194-3622-4. DOI: 10.1117/3.831079.ch8.

[27] P. Laugier and G. Haïat, "Introduction to the physics of ultrasound", in *Bone Quantitative Ultrasound*, Springer, 2011, pp. 29–45, ISBN: 978-94-007-0016-1. DOI: 10.1007/978-94-007-0017-8_2.

[28] L. Mercier, T. Langø, F. Lindseth, and D. L. Collins, "A review of calibration techniques for freehand 3-D ultrasound systems", *Ultrasound in Medicine and Biology*, vol. 31, no. 4, pp. 449–471, 2005. DOI: 10.1016/j.ultrasmedbio.2004.11.015.

[29] M. K. Feldman, S. Katyal, and M. S. Blackwood, "US artifacts", *Radiographics*, vol. 29, no. 4, pp. 1179–1189, 2009. DOI: 10.1148/rg.294085199.

[30] L. E. Bø, E. F. Hofstad, F. Lindseth, and T. A. N. Hernes, "Versatile robotic probe calibration for position tracking in ultrasound imaging", *Physics in Medicine and Biology*, vol. 60, no. 9, pp. 3499–3513, 2015. DOI: 10.1088/0031-9155/60/9/3499.

[31] I. Hacihaliloglu, "Ultrasound imaging and segmentation of bone surfaces: A review", *TECHNOLOGY*, vol. 5, no. 2, pp. 74–80, 2017. DOI: 10.1142/S2339547817300049.

[32] Clarius, *Clarius Scanner C3 HD Specifications*. [Online]. Available: https://www.clarius.com/scanners/c3/specifications (visited on 03/28/2020).

[33] Clarius, *Clarius ultrasound for clinical research*. [Online]. Available: https://www.clarius.com/research (visited on 03/28/2020).

[34] Clarius, *Real-time Elastography Now Available on Clarius Handheld Ultrasound*. [Online]. Available: https://www.clarius.com/real-time-elastography-now-available-on-clarius-handheld-ultrasound (visited on 03/28/2020).

[35] S. R. Kirsch, C. Schilling, and G. Brunner, "Assesment of metallic distortions of an electromagnetic tracking system", *IEEE Trans Med Imaging*, vol. 6141, no. 0J, pp. 1–9, 2006. DOI: 10.1117/12.654768.

[36] M. A. Nixon, B. C. McCallum, W. R. Fright, and N. B. Price, "The effects of metals and interfering fields on electromagnetic trackers", *Presence: Teleoperators and Virtual Environments*, vol. 7, no. 2, pp. 204–218, 1998. DOI: 10.1162/105474698565587.

[37] J. B. Hummel, M. R. Bax, M. L. Figl, Y. Kang, C. Maurer, W. W. Birkfellner, H. Bergmann, and R. Shahidi, "Design and application of an assessment protocol for electromagnetic tracking systems", *Medical Physics*, vol. 32, no. 7, pp. 2371–2379, 2005. DOI: 10.1118/1.1944327.

[38] J. B. Hummel, M. L. Figl, W. W. Birkfellner, M. R. Bax, R. Shahidi, C. R. Maurer, and H. Bergmann, "Evaluation of a new electromagnetic tracking system using a standardized assessment protocol", *Physics in Medicine and Biology*, vol. 51, no. 10, N205–N210, 2006. DOI: 10.1088/0031-9155/51/10/N01.

[39] L. Maier-Hein, A. M. Franz, W. W. Birkfellner, J. B. Hummel, I. Gergel, I. Wegner, and H. P. Meinzer, "Standardized assessment of new electromagnetic field generators in an interventional radiology setting", *Medical Physics*, vol. 39, no. 6, pp. 3424–3434, 2012. DOI: 10.1118/1.4712222.

[40] J. Nijkamp, B. Schermers, S. Schmitz, S. de Jonge, K. F. D. Kuhlmann, F. van der Heijden, J. J. Sonke, and T. J. M. Ruers, "Comparing position and orientation accuracy of different electromagnetic sensors for tracking during interventions", *International Journal of Computer Assisted Radiology and Surgery*, vol. 11, no. 1, pp. 1487–1498, 2016. DOI: 10.1007/s11548-015-1348-1.

[41] J. Gomes-Fonseca, F. Veloso, S. Queirós, P. Morais, A. C. Pinho, J. C. Fonseca, J. Correia-Pinto, E. Lima, and J. L. Vilaça, "Technical Note: Assessment of electromagnetic tracking systems in a surgical environment using ultrasonography and ureteroscopy instruments for percutaneous renal access", *Medical Physics*, vol. 47, no. 1, pp. 19–26, 2019. DOI: 10.1002/mp.13879.

[42] J. Much, "Error Classification and Propagation for Electromagnetic Tracking", Thesis, Technical University of Munich, 2008, pp. 1–92.

[43] M. Feuerstein, T. Reichl, J. Vogel, J. Traub, and N. Navab, "Magneto-optical tracking of flexible laparoscopic ultrasound: Model-based online detection and correction of magnetic tracking errors", *IEEE Transactions on Medical Imaging*, vol. 28, no. 6, pp. 951–967, 2009. DOI: 10.1109/TMI.2008.2008954.

[44] A. M. Franz, K. März, J. Hummel, W. Birkfellner, R. Bendl, S. Delorme, H. P. Schlemmer, H. P. Meinzer, and L. Maier-Hein, "Electromagnetic tracking for US-guided interventions: Standardized assessment of a new compact field generator", *International Journal of Computer Assisted Radiology and Surgery*, vol. 7, no. 1, pp. 813–818, 2012. DOI: 10.1007/s11548-012-0740-3.

[45] M. Hastenteufel, M. Vetter, H. P. Meinzer, and I. Wolf, "Effect of 3D ultrasound probes on the accuracy of electromagnetic tracking systems", *Ultrasound in Medicine and Biology*, vol. 32, no. 9, pp. 1359–1368, 2006. DOI: 10.1016/j.ultrasmedbio.2006.05.013.

[46] Northern Digital Inc., *Polaris Optical Tracking System*. [Online]. Available: https://www.ndigital.com/medical/products/polaris-family/ (visited on 09/16/2020).

[47] A. Brown, A. Uneri, T. D. Silva, A. Manbachi, and J. H. Siewerdsen, "Design and validation of an open-source library of dynamic reference frames for research and education in optical tracking", *Journal of Medical Imaging*, vol. 5, no. 2, p. 021 215, 2018. DOI: 10.1117/1.jmi.5.2.021215.

[48] A. Lasso, T. Heffter, A. Rankin, C. Pinter, T. Ungi, and G. Fichtinger, "PLUS: Open-source toolkit for ultrasound-guided intervention systems", *IEEE Transactions on Biomedical Engineering*, vol. 61, no. 10, pp. 2527–2537, 2014. DOI: 10.1109/TBME.2014.2322864.

[49] R. Kikinis, S. D. Pieper, and K. G. Vosburgh, "3D Slicer: A Platform for Subject-Specific Image Analysis, Visualization, and Clinical Support", in *Intraoperative Imaging and Image-Guided Therapy*, 2014, pp. 277–289. DOI: 10.1007/978-1-4614-7657-3_19.

[50] T. Ungi, A. Lasso, and G. Fichtinger, "Open-source platforms for navigated image-guided interventions", *Medical Image Analysis*, vol. 33, no. 1, pp. 181–186, 2016. DOI: 10.1016/j.media.2016.06.011.

[51] A. Tabb and K. M. Ahmad Yousef, "Solving the robot-world hand-eye(s) calibration problem with iterative methods", *Machine Vision and Applications*, vol. 28, no. 1, pp. 569–590, 2017. DOI: 10.1007/s00138-017-0841-7.

[52] M. Shah, R. D. Eastman, and T. Hong, "An overview of robot-sensor calibration methods for evaluation of perception systems", in *Performance Metrics for Intelligent Systems (PerMIS) Workshop*, 2012, pp. 15–20. DOI: 10.1145/2393091.2393095.

[53] F. L. Markley, Y. Cheng, J. L. Crassidis, and Y. Oshman, "Averaging quaternions", *Journal of Guidance, Control, and Dynamics*, vol. 30, no. 4, pp. 1193–1196, 2007. DOI: 10.2514/1.28949.

[54] Q. Ma and K. M. Ackerman, *AXXB calibration Matlab package*. [Online]. Available: https://www.github.com/RobotMa/axxb_calibration/ (visited on 09/16/2020).

[55] F. C. Park and B. J. Martin, "Robot Sensor Calibration: Solving AX = XB on the Euclidean Group", *IEEE Transactions on Robotics and Automation*, vol. 10, no. 5, pp. 717–721, 1994. DOI: 10.1109/70.326576.

[56] M. Feuerstein, T. Reichl, J. Vogel, J. Traub, and N. NAVAB, "New approaches to online estimation of electromagnetic tracking errors for laparoscopic ultrasonography", *Computer Aided Surgery*, vol. 13, no. 5, pp. 311–323, 2008. DOI: 10.3109/10929080802310002.

[57] M. Li, C. Hansen, and G. Rose, "A software solution to dynamically reduce metallic distortions of electromagnetic tracking systems for image-guided surgery", *International Journal of Computer Assisted Radiology and Surgery*, vol. 12, no. 1, pp. 1621–1633, 2017. DOI: 10.1007/s11548-017-1546-0.

[58] F. L. Markley, *How do I calculate the smallest angle between two quaternions?* [Online]. Available: https://www.researchgate.net/post/How_do_I_calculate_the_smallest_angle_between_two_quaternions (visited on 10/20/2020).

[59] R. Prevost, M. Salehi, S. Jagoda, N. Kumar, J. Sprung, A. Ladikos, R. Bauer, O. Zettinig, and W. Wein, "3D freehand ultrasound without external tracking using deep learning", *Medical Image Analysis*, vol. 48, no. 1, pp. 187–202, 2018. DOI: 10.1016/j.media.2018.06.003.

[60] F. Lindseth, T. Lang, T. Selbekk, R. Hansen, I. Reinertsen, C. Askeland, O. Solheim, G. Unsgrd, R. Mrvik, and T. A. Nagelhus Hernes, "Ultrasound-Based Guidance and Therapy", in *Advancements and Breakthroughs in Ultrasound Imaging*, 2013, pp. 27–82. DOI: 10.5772/55884.

[61] P. W. Hsu, R. W. Prager, A. H. Gee, and G. M. Treece, "Freehand 3D ultrasound calibration: A review", in *Advanced Imaging in Biology and Medicine: Technology, Software Environments, Applications*, Springer Berlin Heidelberg, 2009, pp. 47–84, ISBN: 9783540689928. DOI: 10.1007/978-3-540-68993-5_3.

[62] P. W. Hsu, G. M. Treece, R. W. Prager, N. E. Houghton, and A. H. Gee, "Comparison of Freehand 3-D Ultrasound Calibration Techniques Using a Stylus", *Ultrasound in Medicine and Biology*, vol. 34, no. 10, pp. 1610–1621, 2008. DOI: 10.1016/j.ultrasmedbio.2008.02.015.

[63] H. Zhang, F. Banovac, A. White, and K. Cleary, "Freehand 3D ultrasound calibration using an electromagnetically tracked needle", in *Medical Imaging 2006: Visualization, Image-Guided Procedures, and Display*, vol. Proc. SPIE 6141, 2006, p. 61412M. DOI: 10.1117/12.654906.

[64] R. W. Prager, R. N. Rohling, A. H. Gee, and L. Berman, "Rapid calibration for 3-D freehand ultrasound", *Ultrasound in Medicine and Biology*, vol. 24, no. 6, pp. 855–869, 1998. DOI: 10.1016/S0301-5629(98)00044-1.

[65] G. Carbajal, A. Lasso, Á. Gómez, and G. Fichtinger, "Improving N-wire phantom-based freehand ultrasound calibration", *International Journal of Computer Assisted Radiology and Surgery*, vol. 8, no. 1, pp. 1063–1072, 2013. DOI: 10.1007/s11548-013-0904-9.

[66] M. Welch, J. Andrea, T. Ungi, and G. Fichtinger, "Freehand ultrasound calibration: phantom versus tracked pointer", in *Medical Imaging 2013: Image-Guided Procedures, Robotic Interventions, and Modeling*, vol. Proc. SPIE 8671, 2013, p. 86711C. DOI: 10.1117/12.2007922.

[67] F. Aalamifar, A. Cheng, Y. Kim, X. Hu, H. K. Zhang, X. Guo, and E. M. Boctor, "Robot-assisted automatic ultrasound calibration", *International Journal of Computer Assisted Radiology and Surgery*, vol. 11, no. 1, pp. 1821–1829, 2016. DOI: 10.1007/s11548-015-1341-8.

[68] Clarius, "Clarius Ultrasound Scanner User Manual", pp. 1–111, 2017. [Online]. Available: https://www.clarius.me/wp-content/uploads/2017/01/UltrasoundUserManual.pdf (visited on 03/28/2020).

[69] K. Martin and D. Spinks, "Measurement of the speed of sound in ethanol/water mixtures", *Ultrasound in Medicine and Biology*, vol. 27, no. 2, pp. 289–291, 2001. DOI: 10.1016/S0301-5629(00)00331-8.

[70] Clarius Mobile Health, *Clarius Listen API*. [Online]. Available: https://www.github.com/clariusdev/cast (visited on 10/26/2020).

[71] F. Lindseth, T. Langø, J. Bang, and T. A. Hernes, "Accuracy evaluation of a 3D ultrasound-based neuronavigation system", *Computer Aided Surgery*, vol. 7, no. 4, pp. 197–222, 2002. DOI: 10.1002/igs.10046.

[72] P. A. Yushkevich, J. Piven, H. C. Hazlett, R. G. Smith, S. Ho, J. C. Gee, and G. Gerig, "User-guided 3D active contour segmentation of anatomical structures: Significantly improved efficiency and reliability", *Neuroimage*, vol. 31, no. 3, pp. 1116–1128, 2006. DOI: 10.1016/j.neuroimage.2006.01.015.

[73] U. Mezger, C. Jendrewski, and M. Bartels, "Navigation in surgery", in *Langenbeck's Archives of Surgery*, vol. 398, Springer, 2013, pp. 501–514. DOI: 10.1007/s00423-013-1059-4.

[74] D. C. Barratt, G. P. Penney, C. S. Chan, M. Slomczykowski, T. J. Carter, P. J. Edwards, and D. J. Hawkes, "Self-calibrating 3D-ultrasound-based bone registration for minimally invasive orthopedic surgery", *IEEE Transactions on Medical Imaging*, vol. 25, no. 3, pp. 312–323, 2006. DOI: 10.1109/TMI.2005.862736.

[75] D. Fontanarosa, S. van der Meer, E. Harris, and F. Verhaegen, "A CT based correction method for speed of sound aberration for ultrasound based image guided radiotherapy", *Medical Physics*, vol. 38, no. 5, pp. 2665–2673, 2011. DOI: 10.1118/1.3583475.

[76] J. Smit, "Ultrasound-based navigation for surgical removal of liver lesions", M3 Technical Medicine Thesis, University of Twente, 2017, pp. 1–72.

[77] B. R. Thomson, J. N. Smit, O. V. Ivashchenko, N. F. M. Kok, K. F. D. Kuhlmann, T. J. M. Ruers, and M. Fusaglia, "MR-to-US Registration Using Multiclass Segmentation of Hepatic Vasculature with a Reduced 3D U-Net", in *Medical Image Computing and Computer Assisted Intervention – MICCAI 2020*, Springer International Publishing, 2020, pp. 275–284. DOI: 10.1007/978-3-030-59716-0_27.

[78] J. H. Kaspersen, E. Sjølie, J. Wesche, J. Åsland, J. Lundbom, A. Ødegård, F. Lindseth, and T. A. Nagelhus Hernes, "Three-dimensional ultrasound-based navigation combined with preoperative CT during abdominal interventions: A feasibility study", *CardioVascular and Interventional Radiology*, vol. 26, no. 4, pp. 347–356, 2003. DOI: 10.1007/s00270-003-2690-1.

[79] E. Nypan, G. A. Tangen, F. Manstad-Hulaas, and R. Brekken, "Vessel-based rigid registration for endovascular therapy of the abdominal aorta", *Minimally Invasive Therapy & Allied Technologies*, vol. 28, no. 2, pp. 127–133, 2019. DOI: 10.1080/13645706.2019.1575240.

[80] O. Zettinig, M. Salehi, R. Prevost, and W. Wein, "Recent advances in point-of-care ultrasound using the imfusion suite for real-time image analysis", in *Simulation, Image Processing, and Ultrasound Systems for Assisted Diagnosis and Navigation*, vol. 11042 LNCS, Springer Verlag, 2018, pp. 47–55. DOI: 10.1007/978-3-030-01045-4_6.

[81] O. Ronneberger, P. Fischer, and T. Brox, "U-net: Convolutional networks for biomedical image segmentation", in *Medical Image Computing and Computer-Assisted Intervention – MICCAI 2015*, vol. 9351, Springer Verlag, 2015, pp. 234–241. DOI: 10.1007/978-3-319-24574-4_28.

[82] M. Salehi, R. Prevost, J. L. Moctezuma, N. Navab, and W. Wein, "Precise ultrasound bone registration with learning-based segmentation and speed of sound calibration", in *Medical Image Computing and Computer-Assisted Intervention – MICCAI 2017*, vol. 10434 LNCS, Springer Verlag, 2017, pp. 682–690. DOI: 10.1007/978-3-319-66185-8_77.